Spring 1-1-2013

Computing Ocean Surface Currents from Satellite Synthetic Aperture Radar Imagery

Waqas A. Qazi
University of Colorado at Boulder, waqas.qazi@colorado.edu

Recommended Citation

Qazi, Waqas A., "Computing Ocean Surface Currents from Satellite Synthetic Aperture Radar Imagery" (2013). *Aerospace Engineering Sciences Graduate Theses & Dissertations*. 69.
https://scholar.colorado.edu/asen_gradetds/69

Computing Ocean Surface Currents from Satellite Synthetic Aperture Radar Imagery

by

Waqas A. Qazi

B.Sc. (Hons.), University of the Punjab, 2005
M.Sc. (Hons.), University of the Punjab, 2007

A thesis submitted to the
Faculty of the Graduate School of the
University of Colorado in partial fulfillment
of the requirements for the degree of
Doctor of Philosophy
Department of Aerospace Engineering Sciences
2013

This thesis entitled:
Computing Ocean Surface Currents from Satellite Synthetic Aperture Radar Imagery
written by Waqas A. Qazi
has been approved for the Department of Aerospace Engineering Sciences

William Emery

Baylor Fox-Kemper

Date

The final copy of this thesis has been examined by the signatories, and we find that both the content and the form meet acceptable presentation standards of scholarly work in the above mentioned discipline.

Qazi, Waqas A. (Ph.D., Aerospace Engineering Sciences)

Computing Ocean Surface Currents from Satellite Synthetic Aperture Radar Imagery

Thesis directed by Prof. William Emery

Ocean surface currents play an important role in ocean-atmosphere interactions and global ocean circulation, and are also significant for fishing, ocean navigation, and search & rescue. Existing in-situ and remote sensing techniques for measuring ocean surface currents are limited by spatial and temporal data coverage, and thermal IR feature tracking methods are limited by clouds and weak thermal gradients. High-resolution spaceborne Synthetic Aperture Radar (SAR) offers repeatable cloud-penetrating measurements of the ocean surface. This research explores methods for ocean surface current measurement through satellite-based SAR.

The major part of this research is concerned with the development and application of a semi-automated algorithm to generate ocean surface currents at ≈1.9 km resolution from sequential spaceborne C-band SAR intensity images using the Maximum Cross-Correlation (MCC) method. The primary geographical area of study is the coastal California Current System (CCS), and nearly two years (2008-2009) of 30-min lag data from the Envisat ASAR and ERS-2 AMI SAR sensors is analyzed. The velocity wavenumber spectrum of the derived MCC SAR currents agrees with the k^{-2} power law as predicted by submesoscale resolution models, and also shows seasonal mesoscale variability. The derived MCC SAR currents are validated against High frequency (HF) radar currents, and the two show some agreement in vector direction, with MCC SAR vectors oriented slightly anti-clockwise relative to HF radar vectors. The unimodal mean-symmetric residual histograms indicate that errors between the two datasets are random, except for a mean positive bias of ≈11 cm/s in MCC SAR currents relative to HF radar currents. This magnitude difference occurs primarily in the along-shore component (≈6 cm/s) and is negligible in the cross-shore component. Doppler Centroid Cross-Track (XT) radial currents from Envisat Wide Swath Mode (WSM) scenes are compared with HF radar radial currents, and are seen to have much larger extreme values, which is attributed to the Doppler wind correction process. Ignoring the extreme values, errors between the two datasets appear to be random, with a near-zero mean bias, and are also linked with the Doppler radial estimation errors attributed to model wind corrections. Comparison of Doppler radials with MCC SAR radials for two ≈12-hour lag cases also shows promising results. Finally, experiments conducted with TerraSAR-X experimental Dual Receive Aperture (DRA) mode Along-Track Interferometry (ATI) datasets suggest possible solutions for the absolute phase calibration problem using interferometric phase over ocean only.

Dedication

To the city of Boulder.

I shut my eyes and all the world drops dead;

I lift my lids and all is born again.

Sylvia Plath

Acknowledgements

I would like to thank my advisor, Bill Emery, for being a wonderful, resourceful and always-available advisor who guided me during the course of my research at CU, professionally as well as personally. I would also like to especially thank the remaining members of my PhD committee, Baylor Fox-Kemper, Roland Romeiser, Scott Palo, and Jeff Thayer, for their excellent perspectives and guidance, and for keeping me focused on the right track whenever I wandered off-course during my research. Bob Leben is thanked for letting me discuss ideas with him whenever I hit a wall during my work.

This research would not have been possible without collaboration with many helpful people. Sung Yong Kim and Eric Terrill at Scripps Institute of Oceanography provide the HF radar datasets for the West Coast. Morten Hansen and Johnny Johannessen at Nansen Environmental & Remote Sensing Center (NERSC), Norway, provided the Doppler centroid currents dataset and helped me with analysis and interpretation.

All the friends I've met and made in Boulder, you have made my graduate school experience very colorful and memorable. Thank you, Andrea, Azhar, Gary, Hien, Irina, Mrinal, Mustafa, Nathan, Shahjehan, Stephanie, Ully, Wee Kiat. Thank you to all my colleagues at the lab who helped me out every time I went running to them and from whom I learnt so much, especially Fabio, Carolyn, Ian, and Dan.

A special thank you to the Office of International Education at CU, especially Becky, Janet, and Larry, who have been a constant source of support and encouragement for me throughout my time here.

I would like to express my gratitude to the Fulbright program which supported me during my studies and gave me such wonderful opportunities for cultural and personal engagement. I also acknowledge the NASA Physical Oceanography program which partially supported me.

Contents

Chapter

Appendix

Tables

Table

Figures

Figure

Chapter 1

Introduction

1.1 Introduction

This chapter presents the motivation and scientific rationale behind the research undertaken and presented in this dissertation. An overview of prevailing methods for ocean surface current calculation using Synthetic Aperture Radar (SAR) is given, along with the state of the art. Major research goals are described. Datasets used for this study are also discussed, along with their primary characteristics. Finally, the organization of the dissertation document is detailed at the end.

1.2 Motivation

Ocean surface currents are an important parameter in the study of ocean-atmosphere interaction and climate variability. In-situ current measurement techniques such as drifting buoys are limited in their spatial and temporal coverage. Remote sensing measurements of ocean currents using High frequency (HF) coastal radars are restricted to only near-shore coverage and cannot be deployed in harsh environments. Space-based remote sensing measurements using radar altimetry provide better coverage but only measure geostrophic currents and do not perform well near the coasts. Feature tracking in thermal infrared (TIR) and ocean color (OC) imagery cannot function in cloudy conditions or when thermal gradients are weak. SAR, with its nearly all-weather, day-night operational capability at a high resolution, provides another alternative for ocean surface current measurement.

Oceans are responsible for about one third to a half of the total meridional heat transport of the ocean-atmosphere system, with the primary transport mechanism being ocean currents [32]. The global current circulation is one of the significant parameters that defines regional weather and climate, and is thus also a primary indicator of climate change. The periodic ENSO (El Niño/Southern Oscillation) event, for example, is characterized by changes in the surface current in certain regions. Ocean surface currents are a significant part of the global ocean circulation and they strongly influence ocean-atmosphere interaction. Coastal surface currents are often responsible for surface advection of nutrient-rich waters, which are biologically the richest parts of the oceans [114], thus having a direct impact on the fishing industry. Many marine organisms have their life cycles inherently linked with ocean currents. Near real-time measurements of coastal surface currents are important for the Coast Guard to use in numerical models for search and rescue operations. Surface currents are also significant for shipping, navigation, and the analysis and prediction of the spread of pollutants like oil spills.

In-situ instruments for measuring ocean surface currents, drifting and moored buoys and Acoustic Doppler Current Profilers (ADCPs), have the disadvantage of being restricted to point measurements only. Drifting buoys can provide a Lagrangian view of the near-surface current but this requires repeated seeding of the buoys to comprehensively cover an area; drifters often tend to converge and leave certain ocean areas without measurement. Though effective for current measurement in specific areas of interest, it is prohibitively expensive to routinely and repeatedly deploy in-situ measurement systems in large numbers in all sea conditions. Generation of a surface current field over some region thus requires approximation and interpolation, which reduces the overall accuracy of the derived current field.

Ground-based coastal HF radar stations can measure high temporal resolution real-time surface currents up to 150 km off the coast with a spatial resolution of a few kilometers in most weather conditions [73]. However, their coverage is limited to areas near the coast, and furthermore it is difficult to deploy them in remote areas and harsh environments, such as Alaska and the Polar Regions, due to power and maintenance requirements.

Radar altimetry is a popular space-based remote sensing method to measure mesoscale current features. However, altimetry measurements can only generate geostrophic currents as the currents are derived by inversion of the altimeter sea surface height estimates [35]. Another major restriction is that radar altimetry cannot function well in shallow waters or near coastlines because of land contamination in the large antenna footprint, tidal variations, and rapid atmospheric variations in coastal waters. Present satellite constellation of nadir altimeters is further limited in its spatial resolution and coverage.

Ocean surface currents can be estimated from TIR and OC remote sensing imagery by tracking the movement of features through sequential temporal imagery; one popular and effective method used for feature tracking is the Maximum Cross-Correlation (MCC) method [28, 36]. The MCC method has been successful for Advanced Very High Resolution Radiometer (AVHRR) and Moderate-Resolution Imaging Spectroradiometer (MODIS) TIR data as well as OC data from MODIS. However, this method is inhibited by weather because infrared (IR) and OC data cannot be acquired under cloudy conditions. Furthermore, thermal feature tracking cannot be used in areas where thermal gradients are weak, e.g. the US Gulf of Mexico.

The microwave spectrum (generally 30 cm to 0.1 cm wavelengths or 1 GHz to a few hundred GHz frequencies) is not considerably affected by the atmosphere except for a few attenuation windows between 30 MHz - 30 GHz and rainfall events. Microwave frequencies in the atmospheric transmission windows are very suitable for remote sensing of the Earths surface as they can penetrate clouds and are independent of atmospheric conditions like dust and haze. This allows detection of microwave energy under almost all weather and environmental conditions. Active radar data acquisition, furthermore, does not depend upon the time of day, i.e. it functions equally well at day or night.

Synthetic Aperture Radar (SAR) is a special form of active radar which uses pulse compression and Doppler history to improve range and azimuth resolution, respectively. Typical spaceborne SAR spatial resolutions are on the order of a few meters. Ocean surface current fields can be estimated from SAR imagery by feature tracking in intensity imagery [82], and radial (across-track) currents can be estimated through Along-Track Interferometry (ATI) [48] and Doppler centroid tracking [22]. SAR-derived currents offer distinct advantages over other current measurement techniques involving optical and TIR data in that SAR signals are not blocked by clouds and function in most weather conditions. SAR measurements also offer the possibility of wider coverage with higher spatial resolution than HF radar or feature tracking with IR and OC images. It also has flexibility to perform measurements anywhere in the world, such as areas where deployment of HF radar is difficult. SAR ATI and Doppler centroid tracking can generate currents in areas with weak thermal gradients, where feature tracking in TIR images would not work. For higher latitudes, where cloud cover is very persistent, SAR can help us map surface currents over large areas with a resolution higher than previously possible. Table 1.1 summarizes the above discussion and provides a snapshot of why SAR can act as a good resource for surface current measurement.

Table 1.1: Summarizing comparison of present ocean surface current measurements methods and their characteristics with ocean surface current measurement from SAR remote sensing.

Measurement Method	Characteristic				
	Grid Measurements	Coastal Coverage	Currents Measured	Cloud Independence	Remote Area Operation
In-situ (Drifters, ADCPs)	No	Yes	Total	Yes	No
HF radars	Yes	Yes	Total	Yes	No
Altimetry	Yes	No	Geostrophic	Yes	Yes
TIR Feature Tracking	Yes	Yes	Total	No	Yes
SAR	Yes	Yes	Total	Yes	Yes

1.3 Surface Current Measurements from SAR

The microwave range generally used for SAR imaging of the ocean (C-band to X-band) does not penetrate the surface more than a few millimeters, and thus the scattered returns are characteristic of the surface. Three methods have previously been explored for ocean surface current estimation from SAR; two of these, feature tracking and ATI, are described briefly below. The third, the Doppler Centroid method, is mentioned in Sec. 1.6.2.2

1.3.1 Currents from SAR Intensity Imagery

At intermediate incidence angles (20° - 75°), the primary SAR scattering mechanism from the ocean surface is Bragg scattering through small-scale surface capillary waves. Biogenic surface slicks associated with fish, upwelling, and phytoplankton blooms generally form monomolecular layers on the sea surface [6]. The effect of these monomolecular slicks is to dampen the surface capillary waves by Marangoni damping, which in turn reduces the Bragg backscatter [4, 13]. Biogenic surface slicks thus appear in SAR imagery as lower backscatter regions, as compared to the surrounding ocean surface. In upwelling zones, SAR imaging of upwelling-related surface slicks may also result due to thermal effects [27].

There have been a few published studies exploring feature tracking in SAR intensity imagery for surface current estimation, and they show that surface slicks act as passive tracers for advection due to surface currents. Lyzenga & Marmorino [82] used feature correlation to track ocean surface slicks imaged by airborne SAR and their results from a single pair of images 20 minutes apart compared well with ADCP currents averaged over 10-20 m depths. Surface currents were estimated in two cases by Liu & Hsu [80] through wavelet feature tracking in Envisat Advanced SAR (ASAR) & ERS-2 SAR datasets, however they didn't compare their results with any other ocean current measurements. In Marmorino et al. [85], surface slicks in spiral-eddy convergence zones were tracked to estimate surface currents in a few cases of airborne SAR observations at time separations of around 1.5 hours. More recently, Gade et al. [47] compared the results of current generation from feature tracking on both natural and man-made surface slicks (oil spills). Comparisons with currents generated from a model showed that currents from feature tracking were larger in magnitude. Ciappa et al. [25] have shown that ocean surface currents can also be estimated from SAR intensity images by tracking macro-algae movement through the MCC method. It should be noted that macro-algae blooms, unlike the micro-algae blooms associated with upwelling, form a few-inches thick layer at the sea surface, and appear as a rough and reflective surface.

Previously published work on biogenic slick feature tracking in SAR imagery for estimation of surface currents has been restricted to processing and analysis of relatively small and limited datasets, and a concise general technique for the same has not been reported. Comparisons with other datasets have been scarce or performed for very specific cases. The research outlined in this dissertation attempts to fill these gaps by using a semi-automated algorithm to process large datasets and performing comparisons with ocean currents measured by coast-based HF radar stations. For most of their mission coincidence time frame (2002 - 2011), the European Space Agency (ESA) Envisat and ERS-2 remote sensing satellites with onboard C-band SAR instruments remained in a specific orbit configuration where ERS-2 followed Envisat in the same orbit with a time-lag of 30 minutes. This small time-lag with their high spatial resolution makes these SAR sensors a unique resource for measurement of ocean surface currents. In the primary study area, the California

Current System (CCS), this 30-minute separation is well-suited for observing advection of features which exist at submesoscale to mesoscale time and length scales.

A summary of the above discussion is provided in Table 1.2.

Table 1.2: Summary of reported studies involving the use of sequential SAR images for feature tracking, and contributions of the use of MCC SAR method in this dissertation.

Research Study	Validation Dataset	Feature Tracked	SAR Pair Time Lag	Platform	No. of Pairs Processed
Lyzenga & Marmorino [82]	ADCP current measurements	Biogenic surface slicks	20 min	Airborne	1
Liu & Hsu [80]	-	Biogenic surface slicks	28 min	Spaceborne	1
Marmorino et al. [85]	Numerical model currents	Biogenic surface slicks	100 min	Airborne	2
Ciappa et al. [25]	-	Macro-algae	48 min	Spaceborne	4
Gade et al. [47]	Numerical model currents	Oil spill	11.5 hrs	Spaceborne	1
This dissertation	HF radar measured currents	Biogenic surface slicks	30 min	Spaceborne	124

1.3.2 Currents from Along-Track Interferometry

Ocean Surface currents can be derived from SAR ATI, which is performed by receiving returns from a scene by two antennas displaced in the azimuth (Along-Track) direction. Along-Track Interferometry processing using this phase information can be used to generate ocean current vectors in the elevation (across-track) direction. Use of ATI phase processing to generate ocean currents was first proposed in seminal papers by Goldstein & Zebker [48] and Goldstein et al. [49]. Derivation of currents from ATI has been demonstrated on many airborne SAR ATI systems. However, ocean current recovery from spaceborne SAR ATI is still a subject open to investigation.

TerraSAR-X, in operation since 2008, is the first satellite-based SAR system that offers ATI capabilities. The onboard active phased array imaging antenna can be operated in two special modes, the "Dual Receive Aperture (DRA)" or the "Aperture Synthesis (AS)" mode, to logically divide it into two antennas on the same platform, thus allowing for ATI acquisitions with a short time lag. A theoretical study regarding ocean current measurement from both TerraSAR-X (TSX) ATI modes is presented in [107]. The first results of river currents derived from TSX AS mode ATI data have been published recently by [111]. The preliminary results of river currents from the DRA mode data have been presented by [110].

A primary restriction in using spaceborne ATI for ocean surface current measurement is lack of absolute phase calibration. Often stationary land is used for this purpose, which limits ATI analysis to only ATI scenes with adequate land area. This research will discuss and report experiments conducted for absolute phase calibration of the experimental DRA mode ATI data from TSX.

1.4 Problem Statement

Ocean surface currents measured using in-situ techniques, currents measured from coast-based HF radar stations, and geostrophic currents derived from radar altimetry are all limited by spatial coverage, while remote sensing techniques involving thermal feature tracking are limited by clouds and weak thermal gradients. Spaceborne SAR offers through-cloud, day-night observation capability to determine surface currents at a high resolution on a regular, repeatable basis.

Biogenic surface slicks are characterized in SAR intensity imagery by low backscatter, and some studies have reported tracking slicks to estimate surface currents. However, these studies have only evaluated limited datasets. Furthermore, no systematic validation with other remote sensing measurements has been performed. It is the aim of this research study to develop a semi-automated algorithm to process large SAR datasets to generate coastal surface currents, analyze the results, and compare them with HF radar measured currents.

Estimation of Cross-Track (XT) radial currents using Doppler centroid tracking has been shown to work with Envisat ASAR Wide Swath Mode (WSM) scenes [22, 55, 56]. Cross-Track radial current from Envisat ASAR Doppler centroid tracking will be compared with HF radar measured currents, and where possible, with MCC SAR currents. These comparisons of currents derived from SAR by different methods with HF radar currents and inter-comparison between the SAR methods will be unique in the sense that these datasets are all remote sensing derived products, and thus give greater coverage and comparable spatial scales, and also similar time scales in some cases, as compared to in-situ measurement sources.

The generation of XT radial currents from ATI is well established in theory, and has been utilized extensively for airborne SAR ATI systems. TerraSAR-X offers the first satellite-based ATI system. Initial results of ocean current derivation from TSX ATI [110,111] show that lack of absolute phase calibration is a significant problem in this regard. In this study, experiments will be conducted to evaluate the feasibility of absolute phase calibration from the ocean interferometric phase itself, instead of relying on stationary land areas in an image. It should be noted that TSX acquires ATI data in only experimental mode, and thus the datasets available are not ideal or plentiful.

1.5 Major Research Objectives

The major research objectives are as follows:

- Develop a semi-automated algorithm for processing of Envisat and ERS-2 30-min lag SAR intensity images and generate ocean surface currents by biogenic slick tracking through the MCC method.
- Study and analyze the MCC SAR output current fields.
- Validate the MCC SAR currents with HF radar current measurements.
- Compare Envisat WSM Doppler Centroid radial currents with HF radar radial currents.
- Compare the Doppler Centroid currents with MCC SAR currents in the few cases where overlap is available.
- Conduct experiments on absolute phase calibration for TSX DRA ATI datasets.

1.6 Data

The datasets used in this research are described below.

1.6.1 SAR Datasets

Spaceborne SAR datasets from Envisat, ERS-2 and TerraSAR-X used for derivation of ocean surface currents are described below.

1.6.1.1 Envisat ASAR and ERS-2 Advanced Microwave Instrument (AMI) SAR

Envisat and ERS-2 were ESA satellites, active from July, 1995 to July, 2011, and October, 2002 to April, 2012, respectively. For most of their mission coincidence time period, Envisat and ERS-2 flew in the same near-polar, sun-synchronous orbit, with ERS-2 following Envisat by a lag of 30 minutes. Both of these had C-band (5.3 GHz) SAR instruments onboard: the AMI SAR onboard ERS-2 and the Advanced SAR (ASAR) onboard Envisat. These SAR instruments' standard stripmap image mode acquired imagery at a swath width of 100 km and a maximum Along-Track (AT) length of 100 km. The ASAR, however, was an improvement over the ERS AMI SAR instrument in many ways; it featured the standard HH and VV polarization modes along with alternating polarization modes (VV/HH, HV/HH, VH/VV), and it also operated in two ScanSAR modes: the WSM with 150 m nominal resolution in azimuth/range and 400 km swath, and the Global Monitoring mode with 1 km nominal resolution in azimuth/range and 400 km swath.

For feature identification and tracking in SAR backscatter images, phase-preserved data is not required, rather intensity images are suitable. Archived Image Mode Ellipsoid Geocoded (GEC) SAR datasets from both ASAR and AMI SAR sensors were acquired from ESA. The GEC format is an intensity image format, generated from the raw SAR data using the Range-Doppler algorithm, geolocated and resampled to a map projection, delivered at a pixel sampling of 12.5 m by 12.5 m, with a geometric resolution of approximately 30 m in ground range by 30 m in azimuth. All of these images were acquired in VV-polarization mode, which is better for current mapping purposes than HH-polarization and provides more contrast for the ocean in the presence of a slick (VV-polarization gives higher radar backscatter from the sea surface than HH-polarization [3]). The images were already multi-looked.

Since mid-2007, Envisat WSM scenes are delivered with a low-resolution Doppler centroid estimation grid, which can be utilized for the Doppler centroid tracking method for radial current generation. The acquisition of required archived Envisat ASAR and ERS-2 AMI SAR images over the US West and East

Coasts was made possible through submission of a Cat-1 proposal to ESA.

1.6.1.2 TerraSAR-X (TSX) DRA-mode ATI

TerraSAR-X, launched in 2008, is an X-band (9.65 GHz) SAR imaging satellite for earth observation, operating in a near-polar sun-synchronous orbit at an equatorial altitude of ≈515 km. The onboard active phased array imaging antenna can be operated in special modes to logically divide it into two antennas on the same platform, thus allowing for ATI acquisitions with a short time lag. Along-Track Interferometry acquisition using a single platform offers the advantages of imaging from exactly the same orbit, with the same imaging geometry, for both fore and aft antennas; perturbations would ideally have the same effect on the signals received by both antennas, which may be canceled out when generating an interferogram.

The TerraSAR-X satellite can operate in ATI mode using either the DRA or the AS mode. An experimental DRA mode ATI campaign was conducted for 33 days in April & May 2010. The datasets from this campaign are available from DLR (German Aerospace Center) and 93 DRA mode images were accessed. These data-takes were not user-specific, but are spread over a large geographic sampling, over rivers and oceans. The DRA ATI datasets consist of the complex returns from both fore and aft virtual antennas, and also the full antenna return. The complex returns for both DRA ATI were processed at full azimuth bandwidth and no spectral weighting was applied. The datasets are in slant-range and azimuth coordinate system, and have resolutions of 1.18 m and 3.3 m in slant-range and azimuth, respectively. The acquired datasets were all in HH polarization mode, and had a nominal swath width of 30 km.

1.6.2 Ocean Currents Datasets

High frequency radar measured currents are used in this study as primary validation datasets, and are described below. Doppler centroid currents derived from Envisat WSM images are also described.

1.6.2.1 High frequency (HF) Radar Currents

Coast-based HF radar stations measure real-time surface currents in the upper 1 meter of the ocean surface at 0.5 - 6 km horizontal resolution; the coverage zone extends from the near-coast, except for the surfzone, to 50 - 150 km off the coast (depending upon the radar frequency) [73]. The HF range (3 - 30 MHz) is used to receive Bragg backscatter from the surface capillary waves. The Doppler spectrum of the backscatter is used to derive the underlying current that modifies the phase speed of the surface capillary waves [52]. The raw measurements are radial current observations in the radar transmission direction, and observations from at least two HF radar stations are required for a vector solution. Interpolation techniques are used to convert the radial observations from multiple stations into a two-dimensional surface current field.

High frequency radar stations cover a large portion of the California Coast and give hourly high-temporal resolution data independent of weather conditions. Surface current fields observed from HF radar are available on resampled post-processed grids at both 6 km and 2 km resolutions since 2007 [72]. Hourly 2 km and 6 km grid resolution current fields for 2007-2010 over the California coastal region were acquired from the Marine Physical Lab at Scripps Institute of Oceanography. These current fields were derived from raw radial velocity measurements using the Optimum Interpolation (OI) method (see [72] and [71] for processing details). The OI vector current estimation errors were also included with these datasets. The error covariance matrix for the OI method is computed from the hourly standard deviation of radial velocities or the assumed error variance. However, a normalized nondimensional uncertainty index, generated by normalizing the a posteriori uncertainty matrix with the signal variance (expected variance of surface currents) [72], is considered more useful for error analysis, and three indices of the error estimates are provided with the HF radar current fields. These three indices are linked to the OI estimation errors in u-component, v-component, and vector direction; they approach a value of 0 for an estimate with 0 uncertainty, and approach a value of 1 for an estimate with no information.

Over the US East Coast, HF radar currents are available for certain locations from 2009 under the Mid-Atlantic Regional Coastal Ocean Observing System (MARCOOS). Hourly current fields at 6 km resolution were acquired and used for analysis as needed. It should be noted that these HF radar current datasets over the East Coast are not fully post-processed and are not recommended for comprehensive validation use (personal communication with John Wilkin).

1.6.2.2 Doppler Centroid Radial Currents

The Doppler centroid tracking method is a SAR single-antenna Doppler shift method which enables estimates of XT radial currents. The method utilizes the residual Doppler shifts in the single-antenna return due to relative motion of the target with respect to the antenna. For satellite platforms, the centroid of the measured Doppler spectrum is dominated by the antenna velocity relative to the rotating Earth. This major contribution to the Doppler centroid, along with satellite attitude and antenna pointing contributions, can be modeled and removed from the measured Doppler spectrum. The resultant "Doppler centroid anomaly" depicts the Doppler shift due to geophysical processes, which over the ocean are winds, surface currents, and waves.

The derivation of Doppler Centroid radial currents from Envisat WSM scenes was first reported by Chapron et al. [22]. Hansen et al. [55] improved upon the initial method by extensive error analysis and determined that Doppler radials can be derived from the Doppler centroid grid associated with Envisat WSM scenes can be derived with an accuracy of 30 cm/s or less for incidence angles greater than 27°; the Root Mean Square Error (RMSE) for estimation of Doppler radials is dependent upon the incidence angle. Envisat WSM observations over the time period of a few years have been used to study the Agulhas Current [113] and the Norwegian Sea [56]; in both cases comparisons with other geostrophic current measurements showed favorable results.

Since mid-2007, Envisat WSM scenes are delivered with a low-resolution Doppler centroid estimation grid, which can be utilized for the Doppler centroid tracking method for radial current generation [66]. The WSM images were acquired from ESA through submission of a Cat-1 proposal. The processing for Doppler Centroid currents was done by collaborating research group at Nansen Environmental & Remote Sensing Center (NERSC), Norway.

1.7 Dissertation Overview

The remainder of this document is organized as follows.

Chapter 2 is concerned with detailed literature review pertaining to the research problem. The basics of the physical mechanisms behind SAR imaging of the ocean surface are described first, followed by detailed discussions on the methods and techniques for deriving ocean surface currents from SAR intensity images and ATI. An analytical review of the published studies is given for both methods of current derivation.

Chapter 3 details the area of study, data processing and analysis steps for derivation of surface currents from Envisat ERS-2 30-minute lag SAR intensity image pairs through the MCC method, analysis of the results, and comparisons with HF radar currents. Radial currents from the Doppler Centroid method are also compared with both HF radar and MCC SAR radials.

Chapter 4 describes experiments conducted for absolute phase calibration with TerraSAR-X experimental DRA mode ATI data.

Chapter 5 presents discussions and possible explanations for various issues encountered during the research.

Chapter 6 summarizes the conclusions and gives some recommendations for future work.

The appendices contain relevant and secondary supporting material to the research.

Chapter 2

Background

2.1 Introduction

This chapter presents the literature review of the basic physical processes and techniques used for ocean surface current generation from Synthetic Aperture Radar (SAR). A brief overview of SAR is presented first, followed by a detailed description of the fundamental processes of SAR imaging of the ocean surface in Sec. 2.3. SAR microwaves do not penetrate beneath the ocean surface and the primary scattering mechanism at moderate incidence angles (20° - 70°) is Bragg scattering from small-scale surface waves, modulated by long-scale waves. In Sec. 2.4, the process of ocean upwelling is briefly described, followed by a detailed discussion on the damping of Bragg scattering by upwelling associated biogenic surface slicks, along with an overview of recent published studies regarding feature tracking in SAR for surface current estimation. Sec. 2.5 presents a discussion of the Along-Track Interferometry (ATI) method for estimating Cross-Track (XT) radial currents; the ATI capabilities of TerraSAR-X (TSX) are described in the end.

2.2 Synthetic Aperture Radar - An Overview

A radar's resolution is its ability to distinguish between two adjacent targets in both range (Cross-Track) and azimuth (Along-Track) directions. For a simple side-looking radar system operating at a wavelength λ, with imaging geometry as shown in Fig. 2.1, the azimuth (Along-Track) resolution is governed by antenna pattern aperture and observation range:

$$\Delta R_{az} = R\theta \approx \frac{R\lambda}{d} = \frac{h\lambda}{d\cos\beta} \tag{2.1}$$

where d is antenna size/diameter, θ is antenna beamwidth, h is the radar height, β is the look angle, θ_i is the incidence angle, $\theta_g = 90° - \beta$ is the grazing angle, and R is the slant range to target.

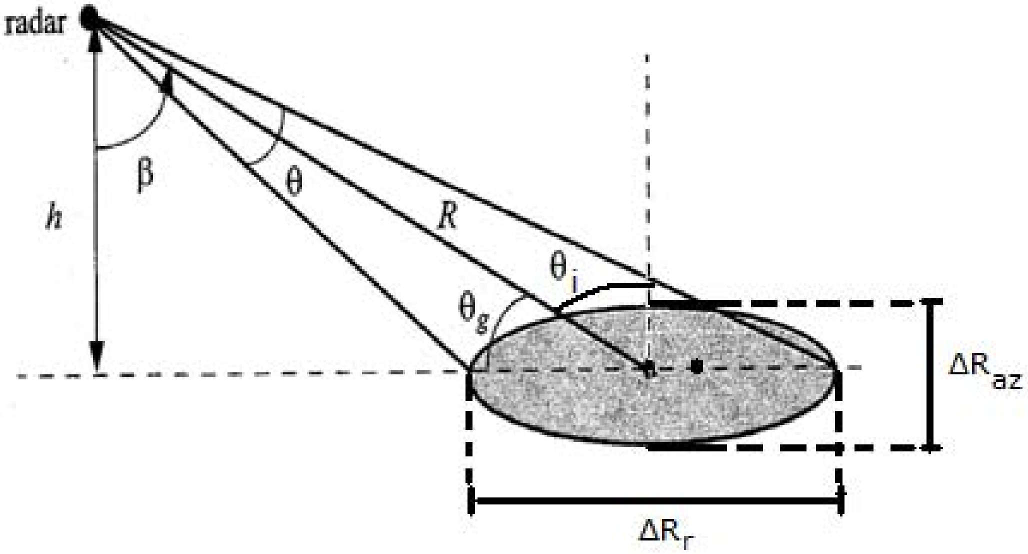

Figure 2.1: Imaging geometry for a side-looking radar. The grey circle defines the antenna footprint on the ground. The specific terms are defined in the text.

The ground range (Cross-Track) resolution is related to the emitted pulse-width τ_p by:

$$\Delta R_r = \frac{c\tau_p}{2\sin\beta} \tag{2.2}$$

where c is the speed of light in vacuum (assuming the radar beam is traveling in vacuum).

The range-resolution can be improved (reduced) using pulse-compression techniques. For fixed R and λ, azimuth resolution can be improved by increasing the antenna aperture size d (Eqn. 2.1). However, there are physical limits on the antenna size, especially for airborne and spaceborne radar platforms. The basic principle for a "Synthetic Aperture Radar (SAR)", as the term suggests, is to "synthesize" a large antenna aperture by using modified data recording and signal processing techniques, achieving very high azimuth resolution for the system using the Doppler history. SAR functionality and image formation are well-established and for further detailed explanations, references are given to [29, 84]

2.3 SAR Imaging of the Ocean Surface

The microwave range generally used for SAR imaging of the ocean (C-band to X-band: 4 to 12.5 GHz [103]) does not penetrate the surface more than a few millimeters, and the scattered returns are thus characteristic of the surface. The ocean surface can be treated as a random rough surface for its interaction with microwaves. The primary scattering mechanism is through small-scale surface capillary waves, however the long-scale waves (primarily wind-driven) also affect the backscatter by influencing the capillary waves through the processes of tilt and hydrodynamic modulation. SAR processing introduces the velocity bunching modulation, which causes azimuth shift of moving targets in the SAR image. The microwave interaction with the ocean surface is discussed in detail in this section.

2.3.1 Microwave Penetration of the Ocean Surface

The electromagnetic properties of water imply that the range of microwave frequencies used for SAR (1-15 GHz) generally do not penetrate beyond a few millimeters of the ocean surface, generally defined as the topmost ocean layer where nearly all exchanges of energy, momentum, light, water, and gases between the atmosphere and the ocean take place. For water, the “complex relative permittivity (ϵ_{cr})”, given by $\epsilon_{cr} = \epsilon_r^{'} - j\epsilon_r^{''}$, is a function of frequency and two physical parameters: temperature and salinity (amount of salt content in water). The real part of relative permittivity $\epsilon^{'}$ describes the ability of the medium to store electrical energy, while the imaginary part $\epsilon^{''}$, also termed as “loss factor”, describes the electromagnetic loss in the medium. Many models have been used to describe the dependence of ϵ_{cr} on frequency, temperature, and salinity (see Appendix B for a brief overview). Comparative analysis of some prominent models by Meissner & Wentz [88] shows that in the 1-15 GHz frequency range, the deviation between these models is negligible. Volume scattering in water is negligible because of the very short microwave penetration depth.

The “absorption coefficient (α)” for microwaves in any medium is a function of frequency and the physical properties of the medium (electric permittivity and magnetic permeability μ):

$$\alpha = \omega \sqrt{\frac{\mu_o \epsilon_o \epsilon_r^{'}}{2} \left[\sqrt{1 + \left(\frac{\epsilon_r^{''}}{\epsilon_r^{'}} \right)^2} - 1 \right]} \tag{2.3}$$

where ω is angular frequency, μ_o is the absolute magnetic permeability, and ϵ_o is the absolute electric permittivity.[a]

The "penetration depth (δ_p)", i.e. the depth at which the electromagnetic power decays to $1/e$ of its value at the surface, is given by:[b]

$$\delta_p = \frac{1}{2\alpha} \tag{2.4}$$

The penetration depth of sea water as a function of frequency is shown in Fig. 2.2 at temperature T = 20 °C and salinity S = 36 ppt (from [63]); the Klein-Swift model was used to calculate this curve [128]. The nominal frequencies of Envisat Advanced SAR (ASAR), ERS-2 Advanced Microwave Instrument (AMI) SAR, and TSX SAR instruments are also indicated in the plot. For both C- and X- band frequencies, the penetration depths are less than quarter of a cm.

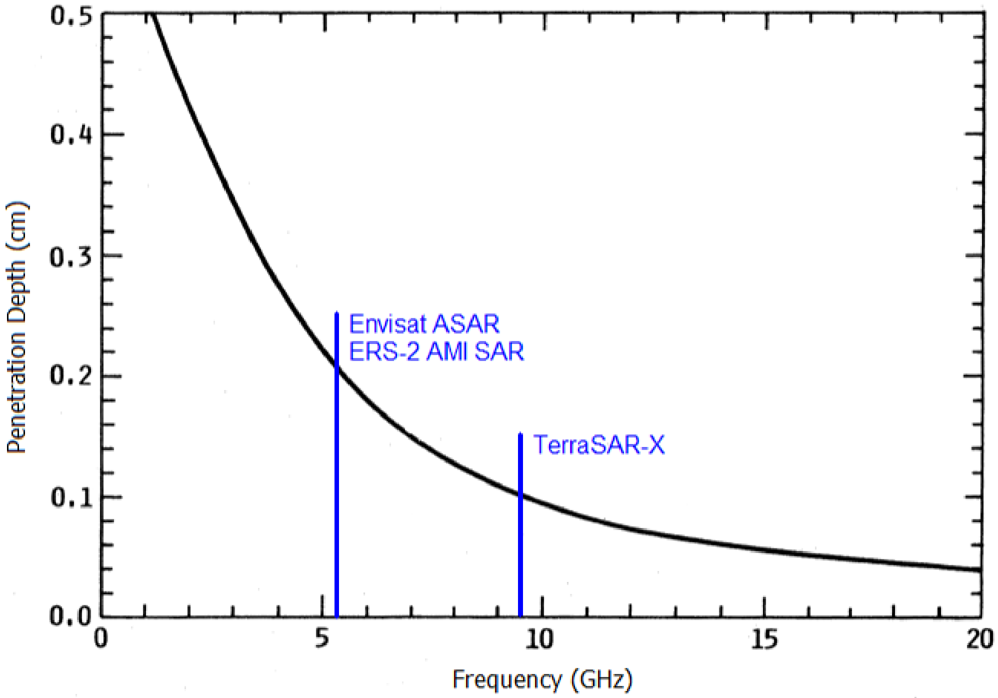

Figure 2.2: Penetration depth of microwaves in sea water as a function of frequency, calculated under the low-loss assumption, at a salinity value of 36 ppt and a temperature value of 20 °C (from [63]); also shown are the nominal frequencies of Envisat ASAR, ERS-2 AMI SAR, and TSX.

---

[a] The relative magnetic permeability μ_r is absent because water is known to be a diamagnetic material, and its relative magnetic permeability is constant with temperature: $\mu_r \approx 1$ [117].

[b] This definition after [128] and [33]

2.3.2 Microwave Interaction with the Ocean Surface

Understanding SAR imaging of ocean surface is more challenging than that of land surfaces because of the inherent motion of the ocean surface. The phase information utilized in SAR image formation loses coherence due to sea surface motion over the integration time because the ocean coherence time is generally less than the integration time. Active microwave scattering from the ocean surface is characterized by surface roughness, interaction of waves at different scales, and wave-current interactions. The ocean surface is generally modeled as a randomly rough surface for its interaction with microwaves.

Models used for electromagnetic interaction with rough surfaces are asymptotic approximations to the exact solution of Maxwell's equations. If the surface curvature is assumed to be small compared to the wavelength, the surface interaction with the wave can be approximated by tangent planes or facets at each point of the surface [16, 129]. This approximation is called the "Kirchhoff" or "Physical Optics" model, and is valid for high frequency (longer wavelengths) and small surface slopes. The Kirchhoff approximation works as a good model for quasi-specular reflection, however it does not give the correct polarization dependence for the radar backscatter [65, 127].

The other widely used approximation assumes the surface curvature to be comparable to or greater than the wavelength, with the Root Mean Square (RMS) surface height being small compared to the microwave wavelength, categorizing the surface as "slightly rough"; this approximation is called the "Small Perturbation Model (SPM)", and is valid for small surface slopes and small wavelengths [129, 137]. The SPM correctly models the backscatter dependence on polarization, however it cannot account properly for long-scale features and specular scattering [126]. To the first order, SPM radar backscatter is only from Bragg scattering, with the Bragg wavenumber being specified by the radar wavelength and the incidence angle [138]. Second and higher-order contributions, such as depolarization, become significant as the amplitude of surface roughness increases with respect to the microwave wavelength [129].

Measurements of radar backscatter from sea surfaces show that the backscatter follows the high-frequency Kirchhoff formulation at large incidence angles, while at low incidence angles, the low-frequency SPM gives better solutions [43]. At microwave frequencies, the sea surface can be modeled as a superposition of independent, random surface-height distributions [79]. The most popular of these "composite" models for the ocean surface is the "two-scale model", which assumes the random rough surface of the ocean to be composed of two scales: small-scale Bragg/capillary waves of the order of the radar wavelength, and large-scale surface waves considerably larger than the radar wavelength, which modulate the small-scale waves. The two-scale model thus utilizes both the Kirchhoff (large-scale waves) and SPM (small-scale waves) roughness regimes. The exact definitions of these scales depend upon the radar wavelength, incidence angle, and the ocean surface height spectrum [15]. Brown [15] recommends using a short-scale wavelength $<3\lambda$ and long-scale wavelength $>3\lambda$, where λ is the radar wavelength. Romeiser et al. [109] use a short-scale wavelength defined by Bragg scattering ($<\frac{3\lambda}{\sin\theta_i}$) for their model (where θ_i is the incidence angle). Other authors use short-scale wavelength values between 2λ and 3.33λ [93]. In general, the small-scale waves can be considered to be <1 m in length while the long-scale waves can be considered to be greater than 10 m.

Even though the two-scale model shows good agreement with measurements, the actual sea surface has a continuous scale of roughness and may not always follow a two-scale model. Many other models for radar backscatter from the ocean surface have been proposed, which attempt to incorporate the intermediate roughness scales and incidence angles not properly modeled by the two-scale model. The "Integral Equation Method (IEM)" [43, 44], for example, unites both Kirchhoff and SPM approximations. It is an iterative procedure, which solves the pair of integral equations for the tangential electromagnetic fields at the interaction interface of the wave and the rough surface. The Integral Equation Method reduces to the Kirchhoff approximation and first-order SPM at high and low frequencies, respectively. Multiscale composite models incorporating waves of intermediate-scales have also been proposed; e.g., the "three-scale model" [99, 109] and the "small-scale approximation (SSA)" [130, 131].

Detailed explanations of the concepts outlined above are given in [126, 129] and references contained therein. Elfouhaily & Guérin [34] present a relatively recent survey of the different models and approaches used for approximating radar backscatter from random rough surfaces. Kasilingam & Shemdin [68] present quantitative comparison of different models used specifically for SAR imaging of the ocean surface. At moderate incident angles (20° - 70°), the two-scale model adequately describes the basic properties of radar backscatter from the ocean surface for commonly occurring sea states.

2.3.3 The Two-Scale Model, Bragg Scattering, and SAR Imaging of the Ocean

The small-scale features in the two-scale model are assumed to have small slopes and displacements, and short correlation over time and space; small segments or facets on the wavelength scale of the capillary waves can thus be considered independent from each other [100]. Large-scale features are assumed to be slowly undulating, having smaller curvatures; the small-scale features can thus be thought of as flat plates or facets riding on the large-scale waves. The small-scale features are primarily responsible for the backscattering while the long-scale features advect and modulate the small-scale facets [138]. The sum of all large-scale waves determines the surface height. The amplitude of the Bragg waves across each facet determines the radar cross-section of the plate. The slope and local angle of incidence of the facet is determined by the slope of the underlying large-scale waves. The facet motion is determined by the instantaneous surface velocities of the large-scale waves, caused mainly by the long-wave orbital velocities. A one-dimensional illustration of the two-scale ocean surface is shown in Fig. 2.3. The long-scale waves change the local angle of incidence of each facet; this angle modulation is called “tilting”.

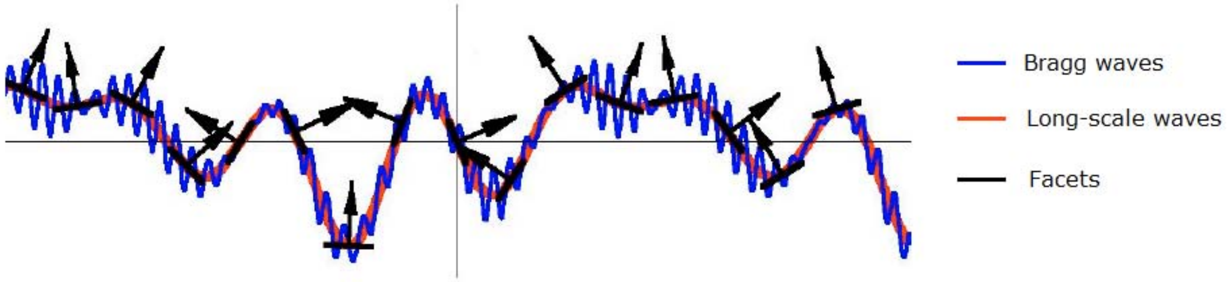

Figure 2.3: Illustration of the two-scale composite ocean surface model. The facets ride on the long-scale waves, and their local angle of incidence is tilted by the slope of the local long-scale wave component (adapted from [65]).

From both the IEM and SSA models, ignoring the long-scale waves, the first-order normalized backscatter radar cross-section (rcs) for small-scale waves is given by [99, 109, 138]:

$$\sigma_{ojj} = 16\pi k^4 \cos^4\theta_i \left|g_{jj}(\theta_i)\right|^2 \left[\Psi\left(2k\sin\theta_i, 0\right) + \Psi\left(-2k\sin\theta_i, 0\right)\right] \tag{2.5}$$

where the subscripts ii denote the radar transmit and receive polarization, $k = 2\pi/\lambda$ is the radar wavenumber, λ is the radar wavelength, θ_i is the local incidence angle, $g_{jj}\left(\theta_i\right)$ is the scattering coefficient, and $\Psi(k_x, k_y)$ is the 2-dimensional one-sided short-wave ocean surface height spectrum (the subscripts x and y refer to the axis in and perpendicular to the plane of incidence, respectively). For HH and VV polarizations, the scattering coefficients take different forms; see [129] for a detailed discussion.

For small-scale waves, in the first order, the ocean wave-spectrum shows that only ocean waves of wavenumber $2k \sin\theta_i$ contribute to the backscatter. This is the classic resonant "Bragg scattering" phenomenon, with the Bragg condition:

$$\lambda_B = \frac{\lambda}{2\sin\theta_i} \qquad or \qquad k_B = 2k\sin\theta_i \tag{2.6}$$

Fig. 2.4 illustrates Bragg scattering from small-scale waves; the Bragg wavelength λ_B is equal to the projection of the radar wavelength on the ocean surface, propagating radially (towards or away) in the radar look direction. A small-scale Bragg wave causes the electromagnetic wave fronts scattered from its different portions to be in-phase and add constructively. The scattering is strongest when the small-scale waves are traveling radially (towards or away) in the radar look direction. Due to Bragg scattering, the ocean radar backscatter cross-section from small-scale waves is directly proportional to the amplitude of the small-scale waves on the ocean surface.

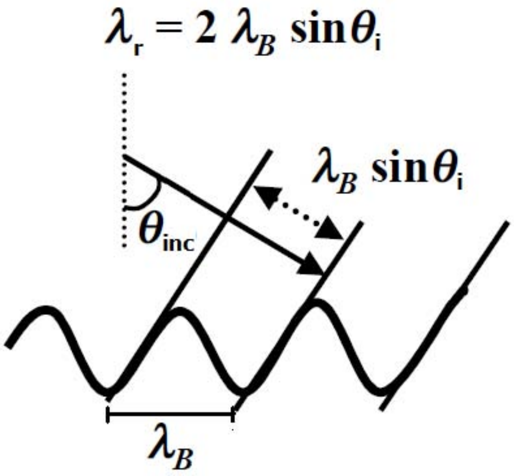

Figure 2.4: Illustration of Bragg scattering from small-scale waves on the ocean surface (adapted from [65]).

As noted previously, long-scale waves cause "tilting" of the short-scale facets, and in that case the backscatter cross-section becomes a function of the facet slopes parallel and normal to the radar look direction, denoted by s_p and s_n respectively:

$$\sigma_{ojj} = T\left(s_p, s_n\right)\left[\Psi\left(2k\sin\theta_i^{'}, 0\right) + \Psi\left(-2k\sin\theta_i^{'}, 0\right)\right] \tag{2.7}$$

where $\theta_i^{'}$ is the effective local incidence angle.

Eqn. (2.7) is the basic formulation of the two-scale model. Explicit expressions for $T\left(s_p, s_n\right)$ are given in [105] and [129]. Tilting causes depolarization of the scattered radar wave, i.e. $T\left(s_p, s_n\right)$ is a function of both HH and VV polarizations, even for a single H or V incident radar wave.

Another well-known effect of long-waves on short-scale Bragg waves that is observed in radar scattering is “hydrodynamic modulation”: the non-uniform modification of short-wave amplitudes by the long-scale waves causes a change in the local short-wave roughness [68]. The long-wave orbital velocity distribution causes short waves to converge and diverge in the long-wave crests and troughs, respectively. This causes preferential formation of short waves at the crests as compared to the troughs.

Both tilt and hydrodynamic modulation are greatest for range-traveling waves and minimal for azimuth-traveling waves. The processes are also polarization dependent, being stronger at horizontal polarization than at vertical polarization. Fig. 2.5 shows an illustration of tilt and hydrodynamic modulation on short-scale waves.

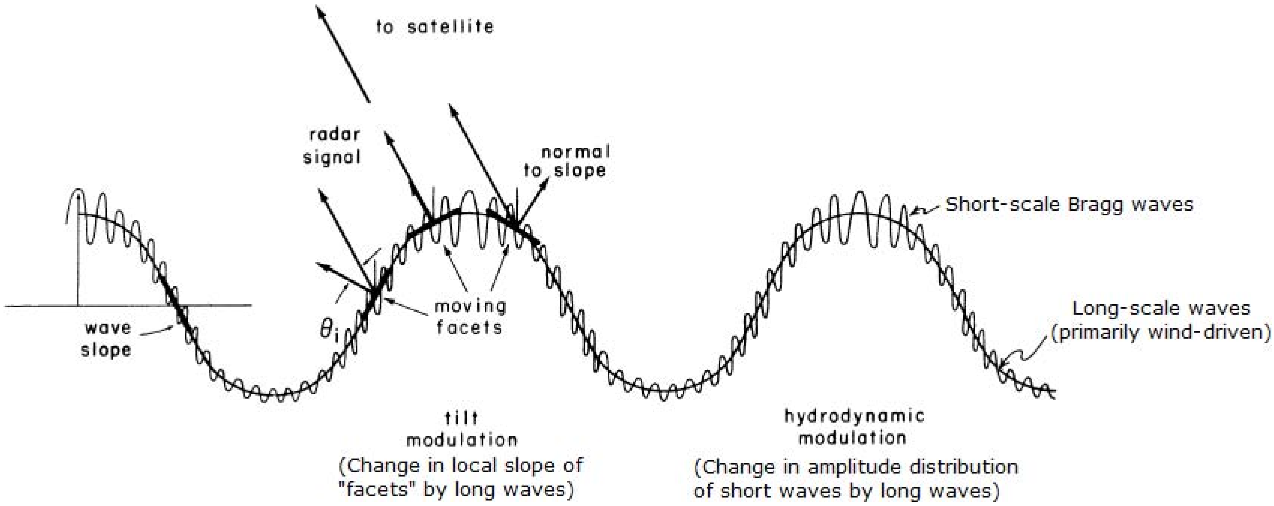

Figure 2.5: Illustration of tilt and hydrodynamic modulation. The long-scale waves change both the orientation (tilting) and the amplitude distribution (hydrodynamic modulation) of the short-scale waves (adapted from [63]).

Both tilting and hydrodynamic modulation are phenomena that occur in regular real-aperture radar imaging of the ocean. Since the ocean surface is in continuous motion, and SAR imaging is not instantaneous, rather spread over some time interval, so SAR processing causes an additional modulation effect, known as "velocity bunching." This effect occurs due to the azimuth-traveling long-wave components. The azimuth-velocity component of an ocean surface scattering element appears as an additional Doppler shift in SAR processing, causing a shift in the apparent position of the scattering element in the azimuth direction. The periodic orbital motion of the long-scale waves thus causes an apparent bunching and spreading in the scatterer density in the image, shifting the azimuth-traveling waves from their true position in the SAR image [63]. For small azimuth-velocities of the long-waves, the apparent shift is linear, while for higher velocities, the azimuth shift becomes non-linear, causing azimuth smearing and downgrading of azimuth resolution.

The three long-wave effects discussed above, i.e. tilting, hydrodynamic modulation, and velocity bunching, can be mathematically described through a modulation transfer function (MTF):

$$R^{SAR}(k) = R^{Tilt}(k) + R^{Hydro}(k) + R^{Bunch}(k) \tag{2.8}$$

Details on MTF characterization in radar and SAR modeling are given in [5, 59, 105]. For further detailed quantitative discussions on SAR imaging of the ocean surface, see [5] and [60].

2.4 Ocean Surface Currents from Sequential SAR Intensity Imagery

Biogenic slicks associated with organic productivity, from fish to phytoplankton blooms to upwelling, are identifiable in SAR intensity imagery due to their lower backscatter. The discussion below details how biogenic slicks decrease the SAR backscatter. Although the discussion deals primarily with slicks associated with upwelling, it can be generalized to monomolecular slicks from any source.

2.4.1 Ocean Upwelling and Surface Slicks

Ocean upwelling is the ascending motion of water from below to the surface, resulting from divergence at the surface and convergence below. In the coastal regions, upwelling activity commonly results in response to coastline-parallel wind forcing, which produces net surface water mass transport to the right of the wind direction in the Northern Hemisphere and to the left of the wind direction in the Southern Hemisphere. The direction of net surface water mass transport is dictated primarily by Earth's rotation, specified by the Coriolis force. Although coastal upwelling zones cover only about 0.1% of the total ocean surface area, yet they are biologically the richest parts of the oceans, producing about 50% of the world's fish supply [114]. The colder water brought up to the surface by upwelling is also of meteorological and climatological importance due to its influence on the atmosphere [140].

In the Northern Hemisphere coastal regions, upwelling occurs because steady wind blowing parallel to the coastline causes net surface water transport to the right of the wind direction due to Coriolis effect; this offshore flow is called "Ekman transport" and is extended offshore in regions experiencing strong winds for long periods of time. The offshore transport causes deeper water to move inshore and upward, bringing low temperature, high nutrient, low oxygen, and lower salinity waters to the surface. Coastal upwelling can also occur due to spatial variations in wind fields: wind stress curl, which is often strong nearshore, can cause surface divergence, the upper layer waters diverge outward and deeper waters move upward to replace them. Areas of intense coastal upwelling include the US West Coast (especially in the summer), northwest coast of Mexico, east coast of Somalia and the Arabian Peninsula [65]. Coastal upwelling in the Northern Hemisphere is illustrated in Fig. 2.6. Wind blowing from North to South along the shore causes net Ekman transport to the right, i.e. away from the shore (Fig. 2.6a). The water displaced offshore is replaced by water from below the Ekman layer (Fig. 2.6b).

Open-ocean upwelling occurs in the equatorial ocean because of westward Trade winds in both Northern and Southern Hemispheres, causing sea surface divergence around the equator.

The cold, nutrient-rich upwelled water encourages phytoplankton blooms at the surface. Phytoplankton are microscopic plants that live in water, both saline and fresh. They are the principal source of organic matter in the oceans and are the first link in the marine food chain. Like all plants, they use chlorophyll for photosynthesis. These phytoplankton undergo increased photosynthesis activity at the surface due to better availability of sunlight and increased nutrient availability due to upwelling. The phytoplankton release extracellular products, mainly photosynthesis by-products, in the form of biogenic surface slicks; most of these

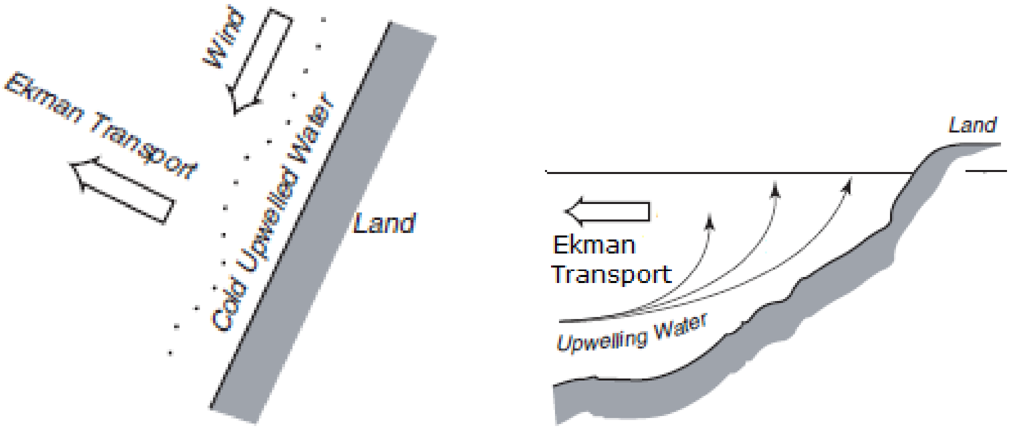

(a) Plane view (b) Cross-sectional view

Figure 2.6: Coastal upwelling in the Northern Hemisphere. Northerly wind causes net transport away from the shore, inducing colder waters from below to rise up to the surface (adapted from [120]).

surface slicks are surface-active (surfactants) which adhere and accumulate at the air-sea interface [132].

Besides phytoplankton, which are the primary producers of surface slicks, bacteria, fish, and zooplankton also produce surface slicks. Surface slicks (of any origin) may appear in a convergence zone of an eddy, particularly the submesoscale spiral eddies that appear in the Southern California Bight (SCB). Studies using ERS 1/2 SAR [31] and airborne SAR [85] in the SCB demonstrate how spiral eddies can be detected through convergence-zone slicks. The study in [31] shows that surfactants can converge within small-scale eddies and delineate sea surface slicks with widths in the range tens to hundreds of meters and lengths greater than 10 km. Marmorino et al. [86] conclude from their analysis of the US East Coast Gulf Stream biogenic slicks that the slicks-stream can be used as current tracers in airborne SAR imagery, however they did not identify the time scales at which the advection due to currents would be identifiable.

2.4.2 Surface Slick Signatures in SAR Intensity Imagery

Biogenic slicks appear as low backscatter regions in SAR imagery. Two physical phenomena are responsible for this: wave damping due to monomolecular biogenic slicks and increased stability due to lower temperatures in upwelling zones. Identification of biogenic slicks in SAR intensity imagery can be a challenge due to various other atmospheric-oceanic phenomena that can appear as low-backscatter features.

2.4.2.1 Marangoni Damping due to Surface Slicks

Biogenic surfactants released by phytoplankton generally form monomolecular layers on the sea surface [6, 65]. The effect of these monomolecular slicks is to damp the surface capillary waves by "Marangoni damping." At the air-water interface, the surface tension is reduced due to the monomolecular slicks. Due to the regular gravity-capillary surface waves, local contractions and expansions of the surface film cause a surface tension gradient, which leads to a surface shear stress. Unlike clear water, a viscoelastic slick layer has non-zero viscous stress, which is balanced by the tangential "Marangoni stress" from the surface tension gradients [4]. The shear stress causes strong velocity gradients in the shear/boundary layer, which leads to enhanced viscous dissipation and enhanced damping of surface waves.

Marangoni stress is stronger in regions where sharp variations of surface slicks occur, e.g. coastal upwelling regions. Fig. 2.7 shows a sketch of Marangoni stress in a coastal upwelling zone. Upwelling causes a local increase in the phytoplankton concentration and biogenic surfactants released from them form a layer on the surface, which cause the Marangoni stress as discussed above.

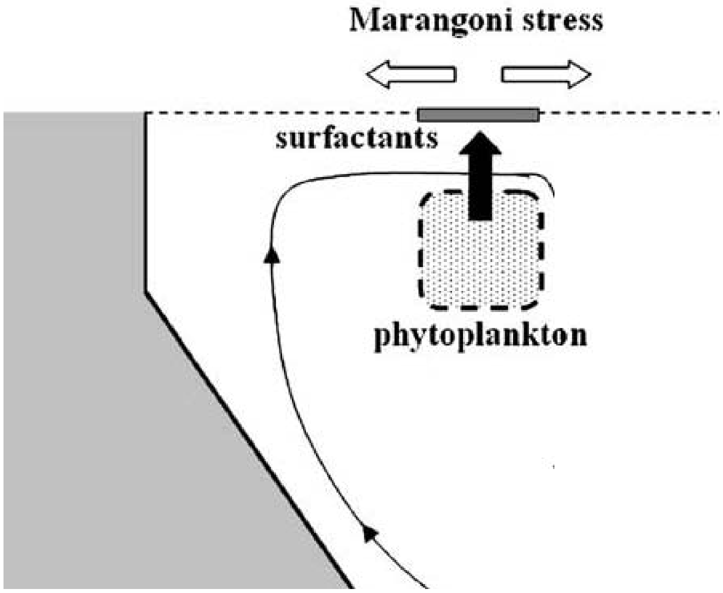

Figure 2.7: Marangoni stress due to coastal upwelling. Upwelling results in increased concentration of phytoplankton and biogenic surfactants. The horizontal gradients of surface tension due to the surfactants results in a Marangoni stress at the surface (adapted from [13]).

The waves associated with the shear stress, called "Marangoni waves", are mostly longitudinal waves in the shear layer, and are heavily damped on the scale of one wavelength. The surface waves experience maximum damping in the presence of a monomolecular slick when they are in resonance with the Marangoni waves according to the linear wave theory. Since waves of different frequencies travel at different phase speeds in water, specified by their dispersion relationships, so resonance occurs when both waves have the same wave number at a given frequency.

According to Marangoni wave theory, the relative viscous damping ratio $y\left(k_w\right)$, i.e. the ratio of the viscous damping coefficient of a slick-covered water surface (Δ_s) to a slick-free water surface (Δ_o), is a strong function of the surface wave wavelength λ_w or wavenumber k_w [4]. For an active radar incident on the water surface, the normalized radar backscatter damping ratio (ratio of slick-free backscatter coefficient σ_o^o to slick-covered water surface backscatter coefficient σ_s^o) is a complex function of $y\left(k_w\right)$ and wind input energy, nonlinear wave-wave interactions, viscous dissipation, and wave-breaking (all contained in the term $S\left(k_w\right)$) [45,69]:

$$\frac{\sigma_o^o}{\sigma_s^o} = \frac{\Psi_o\left(k_w\right)}{\Psi_s\left(k_w\right)} = \frac{\Delta_s}{\Delta_o} S\left(k_w\right) = y\left(k_w\right) S\left(k_w\right) \tag{2.9}$$

where $\Psi_o\left(k_w\right)$ and $\Psi_s\left(k_w\right)$ are the ocean surface wave height spectrums for the slick-free and slick-covered surfaces, respectively.

For explicit formulations for $S\left(k_w\right)$, see [4,45]. It should be noted that for Marangoni damping, $y\left(k_w\right)$ is a strong function of the wavenumber k_w while $S\left(k_w\right)$ is only weakly dependent on k_w. The backscatter damping ratio thus follows the same general functional dependence on k_w as $y\left(k_w\right)$.

2.4.2.2 Thermal Effects

SAR imaging of upwelling and surface slicks may also result due to thermal effects. The colder upwelled waters increase the air stability by causing changes in the air-sea interface temperature gradient. Stability increase over the ocean surface reduces the wind stress on the waves, effectively reducing the surface roughness, which leads to low backscatter [65]. Colder temperatures at the surface change the viscous properties of the surface layer, which also causes increased damping of the Bragg waves [27].

However, thermal effects have less of an impact on low backscatter from surface slicks. Although Chlorophyll-a (Chl-a), a specific type of chlorophyll which is the major pigment in phytoplankton and is generally used as an index of phytoplankton biomass, and Sea Surface Temperature (SST) delineate similar regions at the initial stages of upwelling, biological activity and heat fluxes become independent as time progresses [26]. Higher concentration of Chl-a in upwelling zones in fact eventually causes the temperature to rise because of higher absorption of sunlight by Chl-a [67]. Another factor contributing to the temperature rise is the reduced evaporation due to the surface slicks [46]. The primary backscatter damping mechanism is Marangoni damping due to monomolecular biogenic slicks.

2.4.2.3 Effect of Wind and Other Low Backscatter Features

Since sea surface roughness is primarily caused by the wind stress, so under low wind conditions, there is not enough capillary wave action on the surface, which reduces backscatter. In this case the Bragg backscatter is small in magnitude, so even an ocean surface without slicks would appear as low-backscatter. Strong winds, on the other hand, will tend to roughen up the surface, causing the low backscatter from a slick over the ocean to be contaminated with higher backscatter. Furthermore, higher wind speeds tend to disperse the surface slicks. The slick backscatter damping ratio is thus affected by both low and high winds. In general, the chances of SAR detection of biogenic surface slicks on the ocean surface decrease with increasing wind speed: higher wind speed causes higher waves, removing surface films from the sea surface through wave breaking processes and upper layer mixing [3,125]. The lower wind speed threshold for biogenic surface slick detection in SAR is not well-known, while the higher wind speed threshold has been noted to be in the range of 6-7 m/s [54,94]. For the physical interaction of surface winds with oil slicks and biogenic slicks, see [77,87].

Low-backscatter signatures in SAR intensity images may also occur due to rain, wave-current interactions, conditions in the marine atmospheric boundary layer, and oil slicks [64,125]. Although microwaves in the C- and X-band are generally not affected by clouds, they are attenuated by rainfall events in two ways: volume scattering in the atmosphere and Bragg wave damping on the sea surface by raindrop impact. Newly formed sea ice is relatively smooth and thus also appears as a low backscatter feature in SAR. Distinguishing surface slicks from other low backscatter features over the ocean is one of the major challenges in SAR identification of slicks. Also, due to the above-mentioned phenomena, it is not always possible to detect surface slicks in SAR imagery even if they exist on the surface. These restrictions limit the use of biogenic slick tracking for current detection in SAR images.

2.4.3 Ocean Surface Currents from Biogenic Slick Tracking

Since biogenic slicks damp SAR backscatter, so slick-causing features (upwelling zones, phytoplankton blooms, etc.) should, in principle, be identifiable in SAR intensity imagery by virtue of their lower backscatter as compared to the surrounding ocean surface. Further, as these features are non-stationary at the least on the scale of a few hours due to wind and current forcing, so, theoretically surface ocean currents should be derivable from SAR intensity imagery by tracking such features through sequential imagery.

A few published studies exploring feature tracking in SAR intensity imagery show that surface slicks act as passive tracers for advection due to surface currents. Lyzenga and Marmorino [82] used feature correlation to track ocean surface slicks imaged by airborne SAR to generate surface currents and current gradients, and compared their results from a single pair of images 20 minutes apart with ADCP currents averaged over 10-20 m depths; the comparisons showed reasonable agreement, within SAR geolocation error bounds. Surface currents were estimated in two cases by Liu & Hsu [80] through wavelet feature tracking in Envisat ASAR & ERS-2 SAR datasets, however they didn't compare their results with any other ocean current measurements. In Marmorino et al. [85], surface slicks in spiral-eddy convergence zones were tracked to estimate surface currents in a few cases of airborne SAR observations at time separations of around 1.5 hours. More recently, Gade et al. [47] compared the results of current generation from feature tracking on both natural and man-made surface slicks (oil spills). Currents were generated using cross-correlation feature tracking on biogenic surface films (ERS-2 SAR and Landsat Thematic Mapper data) and oil spills (Envisat ASAR sequential images). Comparisons with currents generated from a model showed that currents from feature tracking were larger in magnitude; this magnitude difference is attributed to local wind forcing at the sea surface, which is not seen in the model currents since they are a mean over the upper-ocean grid point (8 meters in this case).

Ciappa et al. [25] have shown that ocean surface currents can also be estimated from SAR intensity images by tracking macro-algae movement through the Maximum Cross-Correlation (MCC) method. It should be noted that macro-algae blooms, unlike the micro-algae blooms associated with upwelling, form a few-inches thick layer at the sea surface, and appear as a rough and reflective surface.

Previously published work on biogenic slick feature tracking in SAR imagery for estimation of surface currents has been restricted to processing and analysis of relatively small and limited datasets, and a concise general technique for the same has not been reported. Comparisons with other datasets have been scarce or performed for very specific cases. The research undertaken here attempts to fill these gaps by using a semi-automated algorithm employing the MCC method to process large datasets and performing comparisons with ocean currents measured by coast-based High frequency (HF) radar stations. For most of their mission coincidence time frame (2002 - 2011), ESA's Envisat and ERS-2 remote sensing satellites with onboard C-band SAR instruments remained in a specific orbit configuration where ERS-2 followed Envisat in the same orbit with a time-lag of 30 minutes. This small time-lag with their high spatial resolution makes these SAR sensors a unique resource for measurement of ocean surface currents. In the primary study area, the California Current System (CCS), this 30-minute separation is well-suited for observing advection of features which exist at submesoscale to mesoscale time and length scales (Sec. 3.2.1).

2.5 Ocean Surface Currents from SAR ATI

Along-Track Interferometry is used to measure moving target velocity in the range (Cross-Track) radial direction. This section describes the basic theory of ATI velocity measurement and its application to ocean surface current measurement. Along-Track Interferometry measurement of currents from airborne systems is well established, however spaceborne ATI is still largely unexplored. TerraSAR-X ATI capabilities are discussed at the end of this section.

2.5.1 ATI for Radial Velocity Measurement

Along-Track Interferometry is performed by receiving returns from a scene by two antennas displaced in the azimuth direction, so that the signals received from moving features would be different from those received from stationary features. The viewing geometry between the two antennas is essentially the same, with the azimuth separation causing an acquisition time lag. Assuming the atmospheric conditions between the two acquisitions do not change significantly to effect the phase of the scattered signal, the phase difference between the two received signals will be solely due to the scattering target characteristics. For a stationary target, the phase difference should be ideally zero, while for a target that changes its position between the two acquisitions, this movement is incorporated in the change in phase between the two signals.

For airborne and spaceborne systems, ATI data can be acquired by placing the separate antennas along the flight axis of a single platform or using two different platforms in the same flight/orbital configuration following each other. Assuming the time lag between the two acquisitions is sufficiently small such that the moving features do not lose coherence, the differences between pixels imaging the same targets are mainly due to changes in the slant-range-to-target. Consider two antennas operating independently, both transmitting and receiving at the same wavelength λ, imaging the target at times t_1 and $t_2 = t_1 + \Delta t$ respectively, where Δt is the time lag. The respective phases of the scattered signals received at the two antennas are:

$$\phi_1 = \frac{2\pi}{\lambda} 2R(t_1) \qquad , \qquad \phi_2 = \frac{2\pi}{\lambda} 2R(t_2) \tag{2.10}$$

where $R(t)$ is the slant-range to target at the time of imaging. The phase relationship can be easily understood by the fact that the phase will change by 2π over a distance of λ; the additional factor of 2 appears because of the signal's round-trip propagation.

The phase difference between the two signals, called the "interferometric phase", is then:

$$\Delta\phi = \phi_2 - \phi_1 = \frac{4\pi}{\lambda} \left[R(t_1 + \Delta t) - R(t_1)\right] = \frac{4\pi}{\lambda} v_r \Delta t \tag{2.11}$$

where v_r is the average radial (Along-Track (AT)) velocity of the moving target during the time lag interval Δt.

If both antennas are moving at the same velocity v_s, and the AT separation between the two antennas, called "Along-Track baseline", is B_{AT}, the time lag will be $\Delta t = \frac{B_{AT}}{v_s}$ (see imaging geometry in Fig. 2.8). The phase difference can then be written as:

$$\Delta\phi = \left(\frac{4\pi B_{AT}}{\lambda v_s}\right) v_r = \left(\frac{2k B_{AT}}{v_s}\right) v_r \tag{2.12}$$

where k is the radar wavenumber.

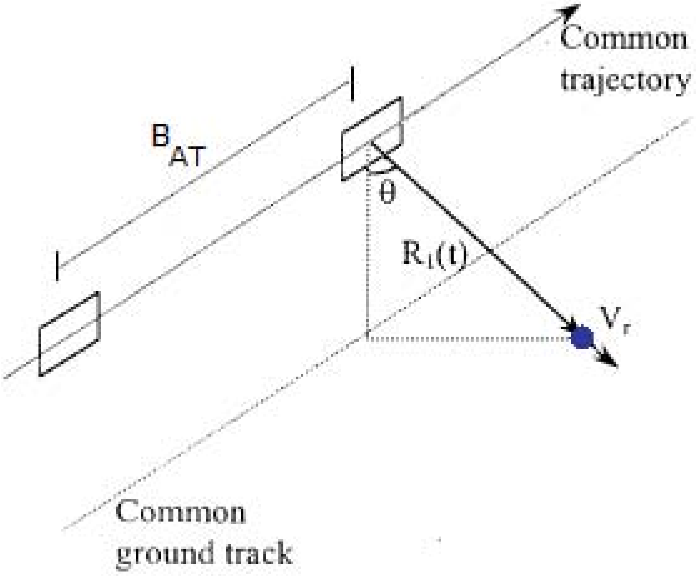

Figure 2.8: Illustration of ATI antenna configuration (adapted from [89])

If only one antenna is transmitting and both are receiving, then the time lag is reduced by half: $\Delta t = \dfrac{B_{AT}}{2v_s}$; the phase difference in this case will be:

$$\Delta\phi = \left(\frac{2\pi B_{AT}}{\lambda v_s}\right) v_r = \left(\frac{k B_{AT}}{v_s}\right) v_r \tag{2.13}$$

Using the above equations relating AT interferometric phase to radial velocity, the radial velocity of a moving target can be derived. The goal of generating two-dimensional current fields can be achieved by either using dual-beam interferometry as proposed in [41] or using two ATI systems in tandem with different squint angles[c] [115].

Due to noise and antenna pattern mismatch, it is nearly impossible to achieve the ideal baseline in ATI systems. Generally, all these effects are collected into a new parameter, called the “effective baseline (B_{ATeff})” to specify the baseline degradation. This effective parameter is then used in radial velocity calculations.

---

[c] Squint angle defined in Appendix C

2.5.1.1 Phase Calibration and Unwrapping

The above derivation assumes that the two antennas are in exactly the same orbit and follow the same ground path, i.e. the ATI system has an ideal AT baseline specified by the linear distance between the antenna phase centers, and there is no XT baseline. In reality, orbital perturbations and antenna issues often cause some XT baseline to be present. Cross-Track interferometric phase does not depend upon velocity of the target, rather it is affected by the topographic variations. Because the total interferometric phase cannot differentiate between the AT and XT phase components, so XT phase correction has to be applied to identify the AT-phase component from the total interferometric phase, and get suitable estimates of radial velocities. Besides XT phase, phase trends from phased array antenna configurations and receiver electronics also cause phase trend contamination. Stationary targets, most often land areas in the image, are often used for phase calibration. Other experimental methods for phase calibration use azimuth displacement of range-moving targets, e.g. in [2], a ship was used, whose velocity was determined by the well-known wake-displacement method [96]. Shemer et al. [116] assumed that the correction calculated from an ocean region with no currents and only Bragg wave contributions is sufficient.

Depending upon a radar system's velocity-to-phase sensitivity and the expected velocity range of the feature of interest, the Along-Track phase can be wrapped over a modulo of 2π, i.e. it is ambiguous over integer multiples of 2π. The task of recovering the true unambiguous phase from this ambiguous or "wrapped" phase is called "phase unwrapping." A relatively simple method is to specify realistic minimum and maximum velocity ranges to restrict the phase interval; other methods involve using a target of known velocity, and statistical estimation [9, 92].

2.5.2 Measurement of Ocean Surface Currents by ATI

As discussed in Sec. 2.3, for moderate incidence angles, the primary ocean backscattering phenomenon at microwave wavelengths is Bragg scattering from short-scale waves modulated by orbital velocities of large-scale waves. This implies that any ocean surface phase variations ϕ_v detected by coherent radar in the XT direction would be the sum of three components in the XT direction:

$$\phi_v = \phi_{short} + \phi_{long} + \phi_{curr} \tag{2.14}$$

where ϕ_{short}, ϕ_{long}, ϕ_{curr} refer, respectively, to phase variations due to phase velocity of short-scale waves, orbital velocity of long-scale waves, and underlying currents.

To determine the phase variation due to the surface currents, the wave contributions to the total phase must be removed. One method to estimate the wave components is through using microwave backscatter models [52, 112]. If the general wind conditions at the time of acquisition are known, it is possible to derive the overall wave spectra from the ATI dataset [90]. Dual-frequency ATI measurements also allow for the derivation of Bragg wave spectra from the data [91]. In specific cases, the long-wave orbital velocity contributions can also be removed by averaging spatially over a few wave periods; this is because the length scale of orbital velocity variations is equal to the ocean wavelength and the mean variation is zero under linear approximation [116]. The effects of long-wave modulation of Bragg waves can be reduced by spectral averaging [90].

Use of ATI to generate ocean currents was first proposed in two seminal papers in the late 1980s [48,49]. Derivation of currents from ATI has been demonstrated on many airborne SAR ATI systems. Ainsworth et al. [2] derived XT currents using the Jet Propulsion Laboratory (JPL) AIRSAR instrument and showed that interferometric phase can be absolutely calibrated using range-moving targets under certain conditions. A squinted dual-beam interferometric SAR was used in [95] to generate 2-D vector currents from a single aircraft pass. Ferrier et al. [39] used an X-band airborne SAR in double-baseline mode to derive XT currents. In [116], an L-band airborne SAR was employed to derive surface currents in the nearshore region. Graber et al. [52] compared XT currents generated from an airborne L-band SAR with HF radar measured currents and found good agreement between the two.

Derivation of surface currents for rivers and coastal waters from the shuttle-based Shuttle Radar Topographic Mission (SRTM) ATI data has been demonstrated in [106] and [108] at a spatial resolution of ≈1 km. However, because the interferogram phase data from SRTM was not absolutely calibrated, the derived currents were only relative, not absolute. The derived currents were converted to an absolute scale by forcing them to conform to expected results in specific areas. Also, the processing did not involve corrections for short-scale and long-scale wave contributions; it was assumed that the wave contributions are too small when compared with the noise in the interferogram.

2.5.3 TerraSAR-X ATI Mode Operation

TerraSAR-X, in operation since 2008, is the first satellite-based SAR systems that offer ATI capabilities. The onboard active phased array imaging antenna can be operated in special modes to logically divide it into two antennas on the same platform, thus allowing for ATI acquisitions with a short time lag. Along-Track Interferometry acquisition using a single platform offers the advantages of imaging from exactly the same obit, with the same imaging geometry, for both fore and aft antennas. TerraSAR-X can acquire ATI data using either the “Dual Receive Aperture (DRA)” or the “Aperture Synthesis (AS)” mode. Both modes transmit with one antenna and receive the returns with two virtual antennas.

The TerraSAR-X platform carries a redundant radio frequency distribution loop in the electronic receive chain. In the DRA mode, the phased array antenna is logically split in the AT direction for signal reception, and the signal is effectively received by two antennas at the same time; for transmission, the full antenna is used, while the receive section is logically split into two parts. Ideal DRA mode operation allows for a baseline that is half the antenna phase center separation, i.e. 0.25 times the total phased array antenna length, however this is rarely achieved in practice.

The DRA mode utilizes the redundant receive chain, which is undesirable due to complex reconfiguration procedures and concerns about using the main and back-up receive chain at the same time; furthermore, conventional SAR acquisitions are not possible during DRA mode operation. The alternate AS ATI mode utilizes a multiplexed single receiver for the reception antenna at double the regular pulse repetition frequency (PRF), thus creating two receive antennas which receive the signals alternately [107]. The antenna geometry and the effective AT baseline remain the same as the DRA mode, but only a single receive electronics chain is used. In the AS mode, the swath width is halved due to doubling of the PRF, and azimuth ambiguities (ghosting) and noise level are increased as compared to the DRA mode. However, switching from conventional SAR operation to AS mode is relatively easier than switching to the DRA mode.

A theoretical study regarding ocean current measurement from both ATI modes is presented by Romeiser & Runge [107]. The first results of river currents derived from TSX AS mode ATI data have been published recently in [111]; they calibrated the phase using phase returns from land and corrected for wave contributions to interferometric phase using a numerical model. The derived radial currents had an effective spatial resolution of ≈1 km. They further constrained the derived currents to the full current vector field by constraining them to a flow parallel to the river bed. The preliminary results of river currents from the DRA mode data have been presented in [110].

2.5.3.1 Absolute Phase Calibration for TerraSAR-X DRA ATI Datasets

One of the primary problems with using TSX ATI data has been lack of absolute phase calibration. Although ATI through TSX offers the advantage of a single platform with no direct XT interferometric phase contributions, the onboard receiver configurations for ATI mode operation introduce phase at the time of data acquisition. For the AS mode ATI, the problem of absolute calibration has been solved by eliminating the channel balancing step during data acquisition [123]. For the DRA mode, the primary reason for phase drift is inadequate antenna pattern sidelobe suppression at the time of reception when the single phased area is logically split into two antennas length-wise. Absolute calibration requirements then currently restrict utilization of DRA mode dataset to cases where there is adequate land in the scene.

To explore other options for absolute phase calibration, experiments will be conducted in this research with experimental DRA mode data acquired in April-May 2010, at different geographical locations. The phase trend in ATI generally manifests itself as a relatively long-scale trend over each line of constant range. Analysis will be made whether it is possible to arrive at an estimated absolute calibrated phase without using stationary land features.

Chapter 3

Ocean Surface Currents from MCC and Doppler Centroid Methods

3.1 Introduction

This chapter describes in detail the area of study, the methodology established to derive surface currents from Synthetic Aperture Radar (SAR) intensity images, and performs analysis and comparison with High frequency (HF) radar and Doppler Centroid currents. Sec. 3.2 delineates the area of study and its characteristics. The Maximum Cross-Correlation (MCC) method and data processing details for Envisat-ERS2 30-minute lag image pairs are discussed in detail in Sec. 3.3. The velocity wavenumber spectra of the MCC SAR currents are analyzed in Sec. 3.4. A comprehensive comparison and analysis is made with HF radar vectors in Sec. 3.5. Radial currents from the Doppler Centroid method are compared with HF radar radials and MCC SAR radials, respectively, in Sec. 3.6 and 3.7. .

3.2 Study Area

The primary study area of the California Current System (CCS) and its characteristics are described below, along with a brief overview of the U.S. East Coast ocean.

3.2.1 The California Current System (CCS)

The California Current System is an eastern boundary current system along the US West Coast, which is well-known for wind-driven upwelling that occurs in the spring-summer (April-August) when surface winds are aligned nearly along-coast, persistently blowing equatorward. The resulting upwelling cold-water filaments can range from submesoscale (1-10 km) to mesoscale (20-100 km) and sometimes grow as large as

200 km [23]. The CCS is relatively well understood, and its oceanographic characteristics at the meso- and larger scales are well-known; the dynamics of the CCS are primarily characterized by strong predominantly northwestward winds and a relatively narrow shelf with abrupt offshore transitions to deep basins (for a good review, see [23, 62]). The high upwelling in the summer is due to offshore Ekman transport when surface wind blows southward along the coast or a strong wind stress curl is present [97]. For the purpose of this study, the region of interest in the CCS is the nearshore region of high biological productivity off the US West Coast (up to about 200 km offshore) [61]. The CCS study area is shown in Fig. 3.1.

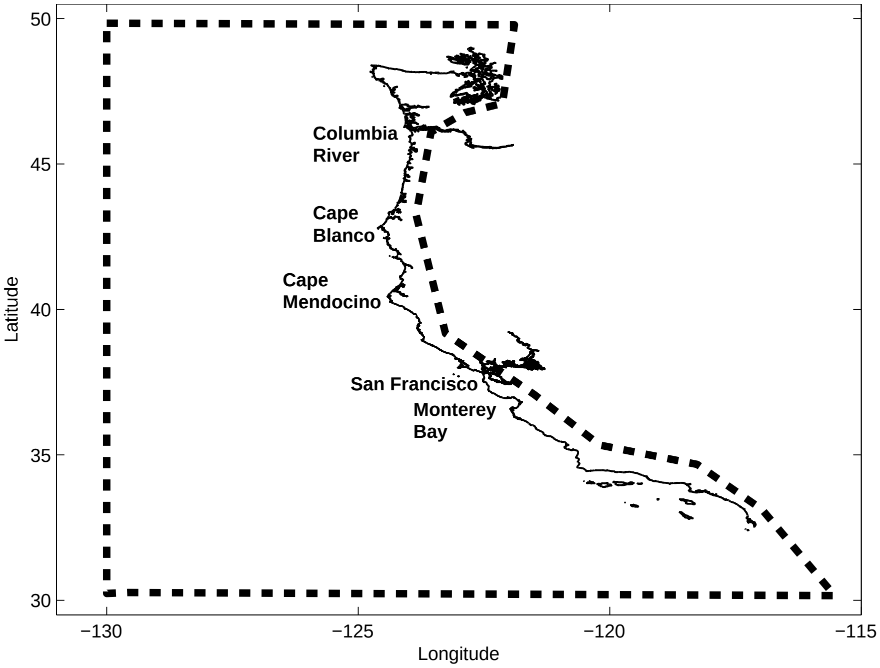

Figure 3.1: Primary study area for surface current estimation using MCC SAR. The solid thin line is the US West Coast, the thick dashed line is the study area over which SAR images were acquired.

In the nearshore CCS, meso and submesoscale current features are expected to vary regionally with respect to offshore distance and bathymetry. Analysis of temporal and spatial scales was performed by Roesler et al. [104] for 6 km resolution HF radar surface currents for 2008 in a near-linear coastal region of the CCS, up to 150 km offshore. The HF radar currents were averaged over 3 days to remove tidal and inertial signals. Length scale analysis, using 10 km non-overlapping bins of distance offshore, showed that the length scale of cross-shore currents grows with distance offshore, from 5-10 km to 50 km. The length scale of along-shore currents is elongated along-shore; it is not appreciably affected by distance from the coast and has a relatively consistent value of 50-60 km. Time scales were also analyzed over each 10 km non-overlapping bins of distance offshore, using the 3-day averaged non-overlapping HF radar current data. Time scales were seen to increase with distance offshore, from about 10 days close to the shore to about 30 days in the open ocean.

Phytoplankton that rise to the surface during upwelling undergo increased photosynthesis activity at the surface due to better availability of sunlight and increased nutrient availability due to upwelling. The phytoplankton release extra-cellular products, mainly photosynthesis by-products, in the form of biogenic surface slicks; most of these surface slicks are surface-active (surfactants) which adhere and accumulate at the air-sea interface [132]. Besides phytoplankton, which are the primary producers of surface slicks, bacteria, fish, and zooplankton also produce surface slicks. The existence of monomolecular surface slicks causes damping of the surface capillary waves through "Marangoni damping", which in turn reduces the SAR Bragg backscatter from the ocean surface (Sec. 2.3). Surface slicks (of any origin) may appear in a convergence zone of an eddy, particularly the submesoscale "spiral eddies" that appear in the Southern California Bight (SCB). Studies using ERS 1/2 SAR [31] and airborne SAR [85] in the SCB demonstrate that spiral eddies can be detected through convergence-zone slicks. The study in [31] shows that surfactants can converge within small-scale eddies and delineate sea surface slicks with widths in the range tens to hundreds of meters and lengths greater than 10 km.

Although some species of phytoplankton can move vertically by adjusting their buoyancy in water, they cannot move horizontally by themselves [11]; thus any horizontal movement of phytoplankton would be due to physical forcing mechanisms, predominantly advection by ocean currents. However, phytoplankton concentration also varies due to biological forcing, i.e. growth, death and sinking of phytoplankton. It is, therefore, important to consider the balance between biological and physical forcing in the CCS in order to infer current advection from spatial variations in phytoplankton (or Chlorophyll-a (Chl-a))which is an indirect measurement of phytoplankton density), which are sources for surface slicks. It has been well established that in the nearshore region, over time scales of 1-10 days and spatial scales of 25-100 km, phytoplankton behave largely as passive scalars and biological forcing mechanisms play only a marginal role in determining their spatial and temporal distributions [30]. Abbott & Letelier [1] show that in the nearshore region, Chl-a and Sea Surface Temperature (SST) respond to similar physical forcing, and have identical decorrelation scales. A more recent analysis in [61] shows that at seasonal time scales, the latitudinal distribution of Chl-a is determined by physical processes upto 100 km offshore; they report a transition from physical to biological control of the Chl-a distribution at distances greater than 100 km offshore. The temporal decorrelation scales of SST and Chl-a in the CCS are strong functions of spatial scales; length scales of up to 25 km are coupled with time scales of up to 24 hours [1, 30, 102]. Spatial statistics of SST and Chl-a are also the same over time scales of 1 day-1 month and spatial scales of 25-100 km [30]. These observations are consistent with the dominance of physical forcing over biological forcing in the nearshore region. In addition to phytoplankton, another manifestation of surface slicks in the CCS is due to afore-mentioned small-scale "spiral" eddies, especially in the SCB, which accumulate surface slicks in their convergence zones. These submesoscale eddies are mostly found at length scales of 10km or less and time scales of less than a day [10, 31, 85]. SAR observations of submesoscale eddies in the SCB find them to be dominantly cyclonic, however this could be due to preferential concentration of surface slicks in cyclonic convergence zones [31]. In [70], a detailed study of submesoscale eddies off southern San Diego, characterized by diameters in the 5-25 km range and persistence of at least a day, using HF radar derived currents shows that they can persist for up to 7 days, follow weak seasonality, and migrate with translation speeds of 4-15 cm/s advected by background currents.

Fig. 3.2 shows a time-length scale diagram for SST and Chl-a pigment patterns in the CCS; the scales are defined by the coherence loss in patterns when the autocorrelation falls below 90% confidence limits. These results are from a study conducted by Denman & Abbott [30] using Coastal Zone Color Scanner (CZCS) ocean color (OC) and Advanced Very High Resolution Radiometer (AVHRR) SST datasets; a coupled biological-physical model by Powell et al. [102] also showed the same time scales. Chl-a, however, does have a smaller scale of spatial variability as compared to SST at the meso and sub-mesoscale, i.e. Chl-a responds faster to physical forcing than SST [83]. Also included in Fig. 3.2 is a depiction of the dominant time-length scales of submesoscale eddies.

The CCS is thus well-known to have sources of biogenic slicks which can be investigated for feature tracking through SAR imagery. Furthermore a large amount of published references of currents and other related variables are available for this region. At the submesoscale to mesoscale length-time scales of the

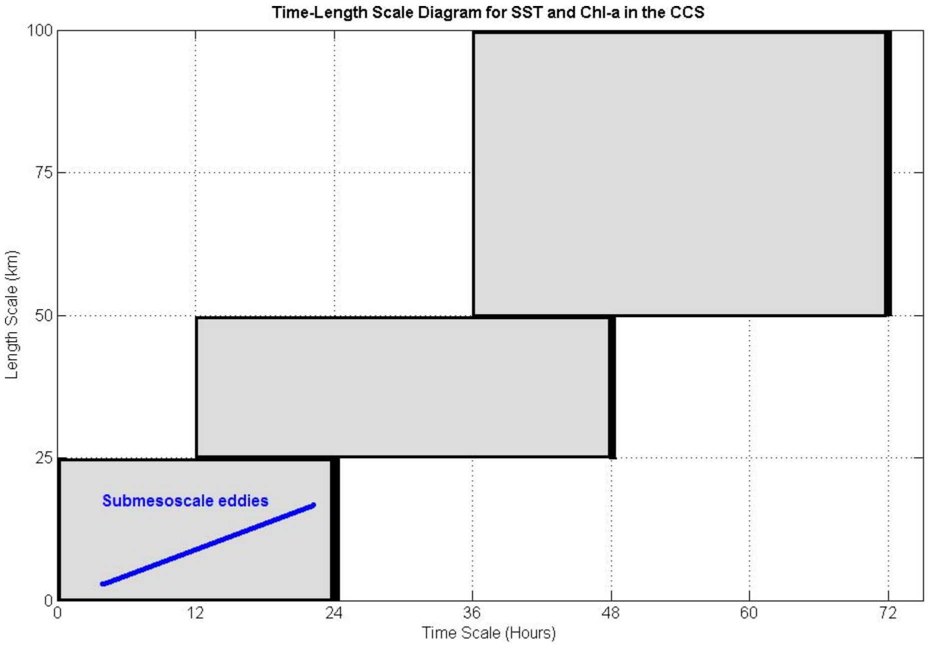

Figure 3.2: Time-length scale diagram for SST and Chl-a in the nearshore California Current System [30,102]. The boxes define the coupling between time and length scales. The dominant scales of submesoscale eddies are also represented (blue line).

nearshore CCS surface currents, and of the slick-causing features, described above, SAR observations at a resolution of 12.5 m, swath widths of 100 km, and a time separation of 30 minutes, are well-suited for observing surface slick advection due to ocean surface currents. Currents from coast-based HF radar stations along the California Coast will be used as reference dataset for comparison with currents generated from SAR through the MCC method.

The California Current System has also been modeled extensively at grid resolution sufficient to capture submesoscale features. Capet et al. [19–21] describe simulations of up to 750 m resolution in this location. The wavenumber spectra of their modeled surface current fields follow a spectral slope (k^{-2}) that is shallower than that predicted by ordinary quasi-geostrophic (QG) theory (k^{-3}), but steeper than that predicted for three-dimensional turbulence and surface quasi-geostrophic (SQG) theory ($k^{-5/3}$). High frequency radar surface current observations also show agreement with the k^{-2} spectral slope at submesoscale wavenumbers [73]. Capet et al. [20] associate this slope with the presence of submesocale fronts and filaments squeezed between the mesoscale and submesoscale eddies in this region. Capet et al. [21] relate these fronts and the distribution of spectral energy with important conclusions about upper-ocean energy cascades.

3.2.2 The U.S. East Coast Ocean

The coastal currents off the U.S. East Coast are characterized by a shallow continental shelf, with nutrients and organics coming from freshwater out-flow and by upwelling over the shelf in certain regions, especially in the summer when Southerly winds generally blow nearly along-shore [12, 17, 81]. Surface slicks are also known to be associated with the Gulf Stream [82]. East Coast upwelling has been observed in SST, OC, and SAR images [26, 27].

A few Envisat ERS-2 30 min lag pairs were acquired over the U.S. East Coast just to demonstrate that the developed method can work over any coastal area with surface slicks. However, comprehensive analysis is restricted only to the CCS on the U.S. West Coast.

3.3 The Maximum Cross-Correlation (MCC) Method for Surface Currents from SAR

This section describes the MCC method and its parameters. The data processing strategies for application of this method on 30 min lag sequential SAR images are then discussed in detail, and output current field examples are shown.

3.3.1 The MCC Method

The MCC method, illustrated in Fig. 3.3, is an automated procedure that tracks the movements of patterns across sequential images by cross-correlating a pattern template subwindow in an initial image within a specified search window in a second image [36]. The displacement vector between the two sequential images is defined to have its origin at the center of the initial pattern subwindow in the first image and the endpoint at the center of the subwindow location with the maximum cross-correlation in the second image. The velocity vector is calculated using the time separation between the sequential images. The use of MCC for generating ocean surface currents from feature tracking in thermal infrared (TIR) and OC imagery is well-established [14, 28, 36].

One of the requirements for MCC to work well is that the time-separation between the sequential images should not be large enough such that the features being tracked decorrelate significantly. Crocker *et*

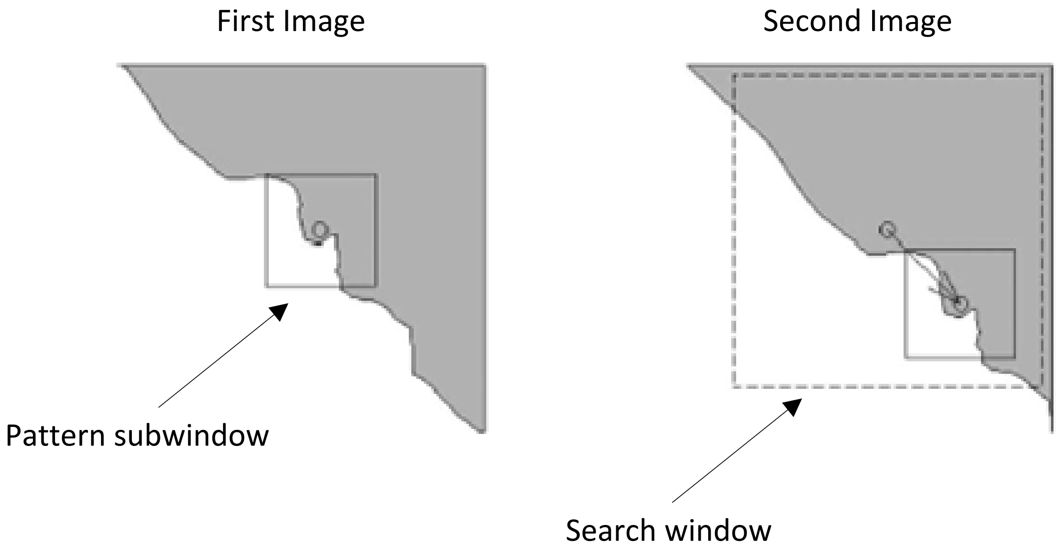

Figure 3.3: The Maximum Cross-Correlation (MCC) method. The solid box in the first image is the template subwindow which selects the pattern. This pattern is tracked in the search window (bigger dashed box) in the second image.

al. [28] showed that for sequential infrared (IR) and OC images at 1 km resolution, the MCC method can function well for time separations up to 24 hours between them. Submesoscale features captured by the finer resolution of SAR will evolve on somewhat faster time scales (Sec. 3.2.1), so the 30 minute separation of the Envisat & ERS-2 configuration is an ideal dataset for this purpose.

The other two main parameters which control the MCC method are the sizes of the template subwindow and the search window. The size of the template subwindow should be large enough to contain enough pixels to define a pattern; however, the larger the subwindow size, the more it smooths out the structure of the flow. The template subwindow size thus has to be defined keeping in mind a balance between the above two factors. The search window in the second image is set in order to resolve the maximum expected velocity.

A raw velocity field output from the MCC method contains vectors at every grid point, with varying values of cross-correlation. Post-process filtering has to be applied to the raw vector field to get a vector field that depicts the geophysical characteristics of ocean surface currents. As a first step, a minimum correlation cutoff value is used to remove vectors that result from low values of pattern cross-correlation. Vectors associated with single-pixel displacement or having a magnitude larger than a defined threshold value are also removed. Finally, a nearest-neighbor filter is used to ensure spatial coherence. For each grid point in the vector field, the target vector is compared with all other vectors in its immediate neighborhood. The comparison can be made in many ways, the most common method is to use difference thresholds for u- and v-component magnitudes and direction, and the number of neighborhood vectors violating any of these thresholds is determined. If the number of neighborhood vectors that exceed the defined difference thresholds is greater than a specified limit, the target vector is flagged and discarded. In its common form, the nearest-neighbor filter is thus characterized by the neighborhood size, choice of thresholds for u- and v-components magnitudes, choice of threshold for direction, and choice of the number of neighborhood vectors that must agree to the target vector within these thresholds to keep the target vector.

One important additional step in the processing of TIR and OC imagery for MCC is cloud filtering. This will not be needed for SAR as clouds are transparent for the microwave range of frequencies used for SAR remote sensing.

3.3.2 Generating Currents from 30-minute Lag SAR Images

The data processing chain for the Envisat, ERS-2 30 minute lag image pairs is shown in Fig. 3.4 as a flowchart. Each processing step is described in detail below. Since the Envisat and ERS-2 SAR intensity images are acquired from two different instruments, they were radiometrically calibrated to normalized backscatter σ^o as a first step.

SAR datasets for both Envisat and ERS-2 are delivered as “scenes” of maximum along-track length of 100 km. This poses a problem when an image “strip” of length $>$ 100 km is ordered from the archive: the image strip is delivered as a sequence of 100 km scenes with some overlap between consecutive scenes. Since the Envisat and ERS-2 SAR images do not cover the exact same area on the ground, mosaicking these separate scenes into one image strip is required, for each of Envisat and ERS-2, separately. However, during initial experiments, it was noticed that consecutive scenes in a strip do not have the exact same geolocation, rather there is a “sliding” shift between them in the direction of cross-track imaging; an example of this is shown in Fig. 3.5.

The magnitude of this slide-shift varies for different strips. The geolocation error due to this slide-shift

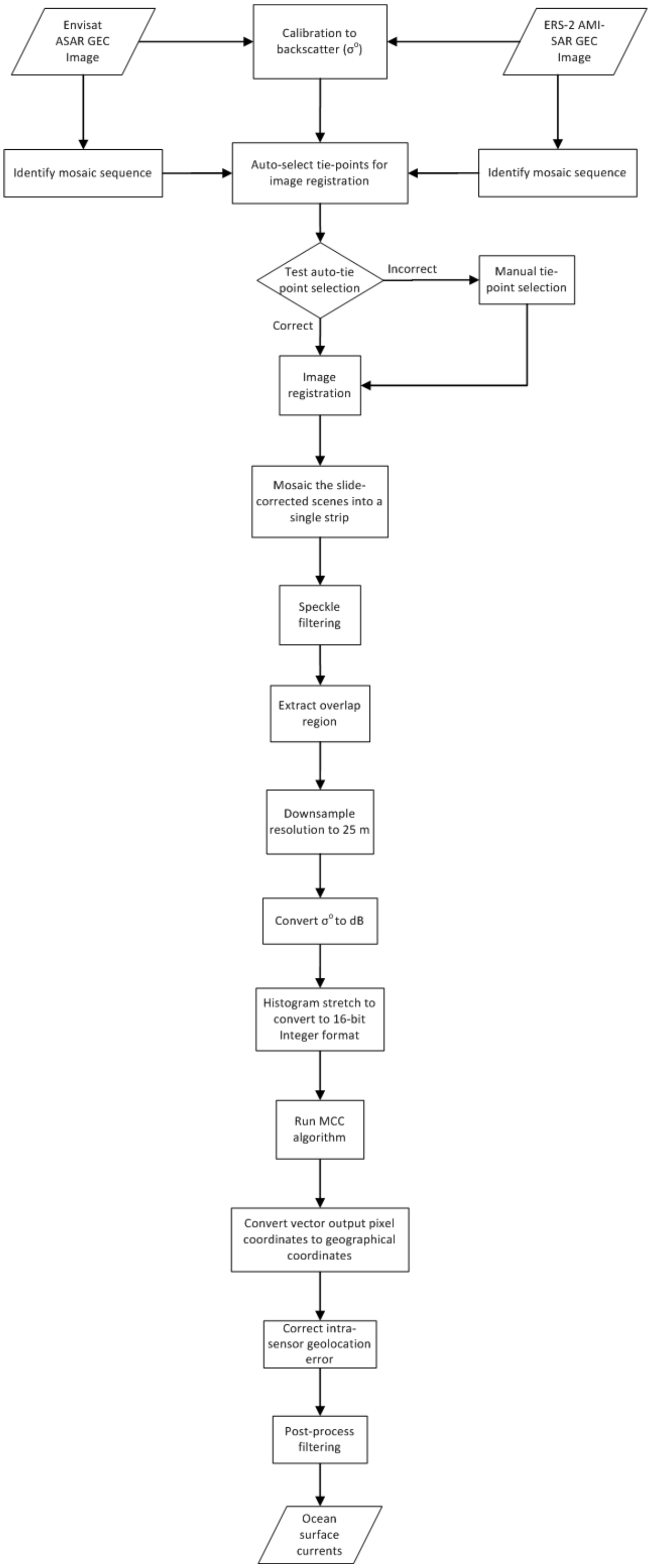

Figure 3.4: Data processing flowchart for generating currents from 30-min lag SAR images (see Sec. 3.3.2 for detailed description).

has to be corrected first before mosaicking the scenes into a single seamless strip. The requisite geolocation correction was performed through image registration. For consistency, the northern-most scene was always chosen as the base image in the geo-registration process. For strips with more than 2 scenes, a consecutive registration process was used, i.e. the 3rd scene in the strip was registered to the warped 2nd scene as base, the 4th scene in the strip was registered to the warped 3rd scene as base, and so on.

Since the geolocation error between overlap scenes is only a translation due to slide-shift in one direction, and there is no perceptible rotation or skew error, a polynomial of the first degree with bilinear resampling was deemed sufficient for image registration. Automated area-based matching algorithms were used for tie-point selection between the overlapping scenes, which were then used to generate the fit param-

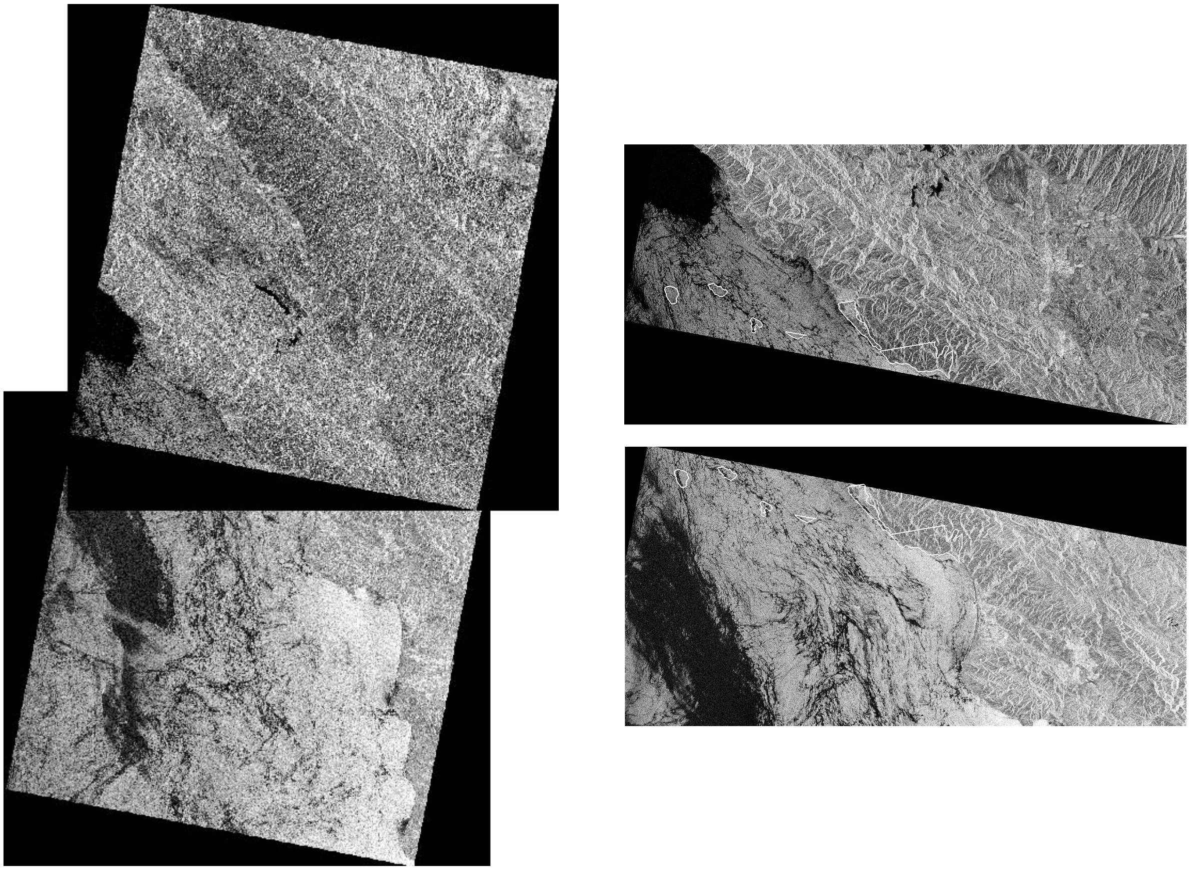

Figure 3.5: Example of the slide-shift geolocation error between overlapping scenes in a single strip. An Envisat ASAR strip comprised of two scenes is shown in the left panel, calibrated to σ^o and converted to dB for visualization. The right panel shows a zoomed in view of the overlap region of the two scenes; the white polygons represent a vector overlay tied to the coordinates of the northern (top) image.

eters of the one-degree transformation polynomial between the base and warp images.

The automated methods for tie-point selection did not work properly in all cases. An automated procedure for testing the automated tie-point selection and subsequent image registration was developed and manual tie-point selection and registration had to be performed for the cases which failed the test. This testing procedure is described in Section 3.3.3. For the West Coast, out of a total of 94 multi-scene Envisat-ERS2 image pairs, 60 pairs (63.8%) failed this test in either Envisat or ERS-2 image registration and manual processing had to be performed for them.

After correcting for the slide-shift in all scenes of the strip, a single seamless strip is generated through mosaicking. Geolocation errors also exist between the Envisat and ERS-2 images, corrections for these are discussed further below.

SAR intensity images have a characteristic "speckle" noise due to the coherent integration of randomly distributed backscatter phase from multiple scatterers within one ground resolution cell. The grainy speckle noise results in a SAR intensity image that does not have a constant mean radiometric level in homogeneous areas. In SAR intensity images, speckle noise has an exponential distribution, and can be statistically modeled as multiplicative noise. Speckle can be reduced at the cost of resolution by "multilook processing" on the Doppler spectrum [29]. Although the SAR intensity images were already multi-looked, there was still significant speckle noise in the images. Spatial filters were used to further suppress speckle: successive Lee, Median, Median (3 x 3 pixels) were applied to preserve edges while smoothing.

The mosaicked speckle-filtered Envisat and ERS-2 image strips were then spatially subset to the region of mutual coverage. For ease in data handling and faster processing, the images were downsampled at this point by a factor of 2, from the native 12.5 m resolution to 25 m resolution.

In the calibrated σ^o image, ocean has low backscatter values in general, and the features of interest (biogenic slicks) are at even lower backscatter due to damping effects (Sec. 2). It is useful to increase the contrast of these low intensity values; this is done through applying a dB transformation, which maps a narrow range of low calibrated backscatter values into a wider range of output values, at the cost of decreasing the overall dynamic range in the image [50]. The higher values of calibrated backscatter are mapped into a narrower range in the output, but this is not of concern as higher backscatter values in the image are over land.

At this point in the processing chain, the SAR images were stored in single-precision (32-bit floating point) format. The legacy MCC program, however, takes data input only in 16-bit integer format. The processed SAR images were thus converted at this stage to 16-bit integer format through linear histogram stretching.

The MCC program was run with a maximum velocity threshold of 60 cm/s for the search window. High-velocity jets in the CCS are known to achieve velocities in excess of 50 cm/s [23]; Crocker et al. [28] used a maximum velocity threshold of 70 cm/s for defining the search window for running MCC on IR and OC imagery. For testing purposes, a few datasets were processed using two different maximum velocity limits of 60 cm/s and 70 cm/s. In the case of 70 cm/s velocity threshold, there were only a few vectors generated with magnitude higher than 60 cm/s, and most of them were discarded during post-process filtering. The velocity threshold of 60 cm/s was chosen as a constant value for processing all datasets. For a pixel resolution of 25 m and a time separation of 30 minutes, this corresponded to a search box of 75 x 75 pixels. The pattern subwindow size was chosen to be 1.1 km x 1.1 km (44 x 44 pixels), adequate enough to track the features that exist in the range of tens of meters up to 2-3 km, yet small enough to not smooth out the fine-resolution during pattern matching. Thus, the resolution of the MCC velocity field will be less than the 25 m SAR images (1-2 km is chosen here).

The MCC program takes the input integer-format sequential images as 2-D arrays and the output vectors are given in terms of pixel coordinates. Using the map projection information attached with the input images, the pixel coordinates were converted to geographic coordinates (longitude and latitude). The output grid resolution of the current fields was 1.87 km.

The slide-shift geolocation error between consecutive scenes in the same strip and its correction was described above. Besides that, there is also a slide-shift error between the Envisat and ERS-2 images. The correction for this intra-sensor slide-shift depends upon the number of scenes in the image strip for each sensor. In the simpler case where the image strips for both Envisat and ERS-2 are composed of only one scene each, this geolocation error can be treated simply as a uni-directional slide-shift between the two images. The input images to the MCC algorithm are not land-masked, and ideally the cross-correlation over land should not show any movement vectors over the time-period of 30 minutes. Any vectors over land are thus a depiction of the geolocation error between the two sensors. Experiments indicated that the vector magnitudes are nearly constant over land, with some outlying vectors near the image edges and coast-ocean boundaries. The intra-sensor geolocation error in this case is corrected by first calculating the overall mean of the shift vectors over land and then removing this mean value from the ocean current vectors. Note that while calculating the mean shift, vectors near the coast-ocean boundary are ignored, along with any vectors that are statistical outliers (any vectors outside 1.5 standard deviation range, calculated from the total set of vectors over land).

The intra-sensor geolocation error correction gets more complicated when either or both of Envisat and ERS-2 strips have multiple scenes: every scene in each strip is on a slightly different geolocation grid. Assuming that image registration during the mosaicking process for each strip is accurate enough, the overall mean shift vectors over land should give a shift vector close to the true shift vectors between every pixel in the overlap region of the two sensors. While calculating the mean shift vector over land, the same pruning process is used as in the case of single-image strip: vectors near the coast-ocean boundary and vectors that are statistical outliers (vectors that fall outside the 1.5 standard deviation limit) are ignored. Due to the underlying assumption above, the accuracy of the geolocation correction for mosaicked strips depends upon the accuracy of the image registration in the mosaicking process.

The raw MCC output vectors fields were post-processed using the filters described above. The cross-correlation minimum cut-off was set at 0.2; this was an empirical value decided by experimenting with a few sample cases. Vectors associated with single-pixel displacement and a maximum velocity of 60 cm/s were removed. The nearest-neighbor filter was used with a neighborhood size of 5 x 5 grid points, with the target vector at the center grid point. The direction difference threshold was set at 60° and the u- and v-component difference thresholds were set at 0.8 times target vector u- and v-component magnitudes, respectively. If more than 3 neighborhood vectors violated any of the above thresholds, the target vector was discarded. Post-process filtering is the final step in the processing chain.

3.3.3 Procedure for Testing Automated Tie-Point Selection and Registration

As mentioned above, an automated procedure for testing tie-point selection and subsequent image registration prior to scene mosaicking in a strip needs to be devised. This procedure was developed based on the MCC algorithm, and is shown in Fig. 3.6 as a flowchart. For any two consecutive scenes in the strip which need to be geo-registered, the auto-tie point algorithm is run with different settings. If the auto tie-point algorithm gives unrealistic values of points (e.g. sometimes the top-left corner in both images is erroneously chosen as a tie-point), then the images are not registered, and manual tie-point selection is required in this case.

In the other case, when realistic tie-points are chosen, the images are registered using the selected tie-points, subset to their overlap area, downsampled to 25 m resolution, transformed to dB, and converted to 16-bit integer format through histogram stretching. These images now cover only the overlap area between the consecutive scenes. To check for geolocation errors in these subset images, the MCC algorithm is run over them, with a pattern subwindow size of 25 x 25 pixels and a search window size of 50 x 50 pixels; these window sizes are chosen as a balance between efficient processing and assumptions regarding expected maximum geolocation errors. A time-separation value of 1 sec is used, so that the output vectors effectively give the shift vectors in cm units.

The raw vectors from the MCC algorithm are filtered at a minimum cross-correlation coefficient threshold of 0.3. If the MCC vectors are non-existent or have zero values above the 0.3 cross-correlation threshold, this indicates that the images have been properly geo-registered. If the number of non-zero MCC vectors is more than 10% of the total number of vectors, that means there is a possibility of georegistration error. In this case, the vectors are filtered again by removing outliers (vectors that fall outside the 1.5 standard deviation range), and the overall mean of the filtered vectors is calculated. This overall mean vector is a quantitative measure of the geolocation error in cm. This can easily be converted into the 25 m pixel georegistration error (see Sec. 3.3.4).

A summary of these parameters is generated, which identifies the multi-scene strips which need manual tie-point selection and geo-registration.

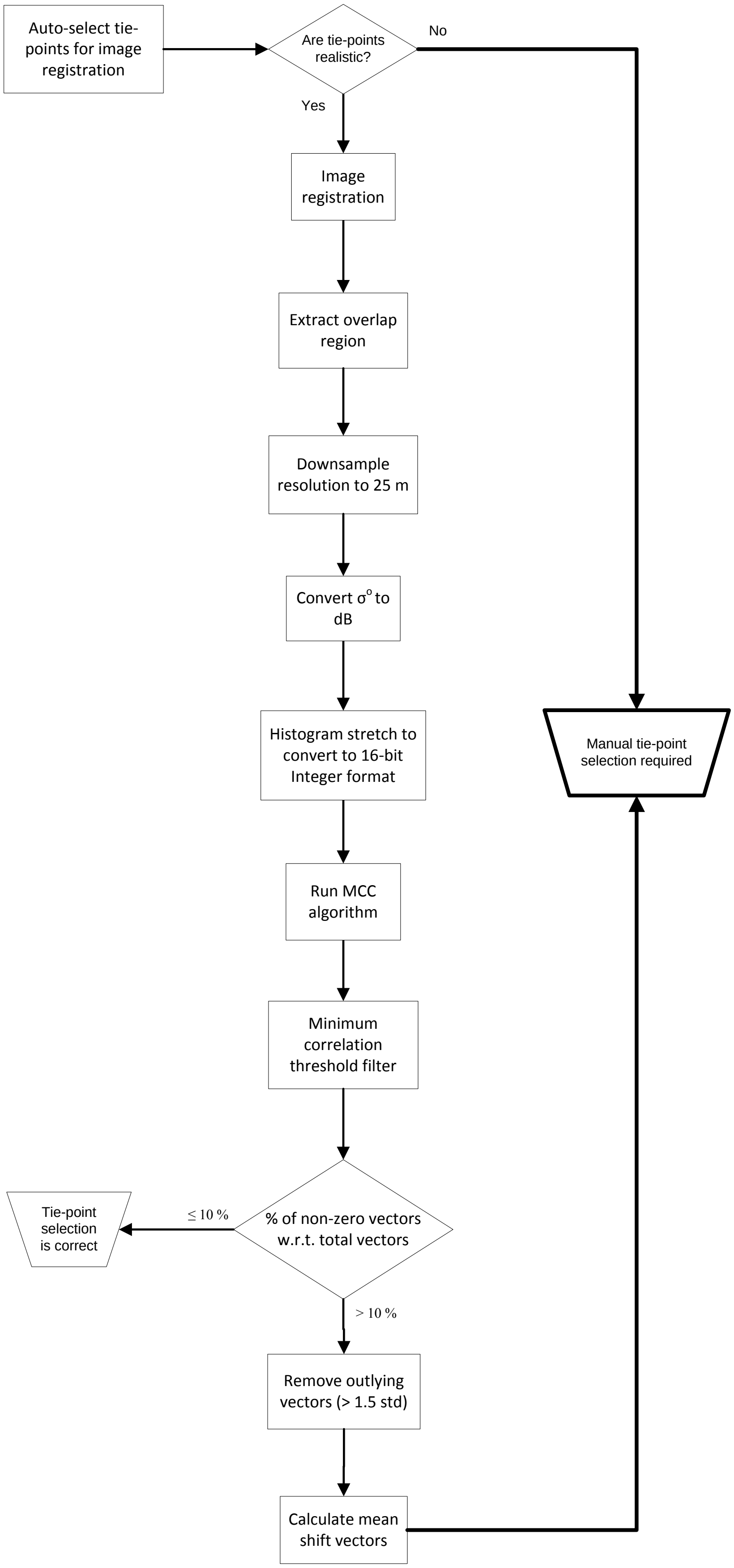

Figure 3.6: Data processing flowchart for testing automated tie-point selection and image registration (see Sec. 3.3.3 for detailed description).

3.3.4 Absolute Accuracy of MCC SAR Currents

As a rudimentary control on absolute accuracy of the output currents, any velocities associated with the displacement of a single pixel are discarded in the post-process filtering. This means that any velocities below the magnitude value of $\frac{25\ m}{30\ min} = 1.39\ cm/s$ are considered unreliable.

The geolocation errors in a multi-scene strip and between the two sensors, described in detail above, both play a fundamental role in defining the absolute accuracy of the estimated currents. The correction for intra-sensor geolocation errors indirectly depends upon the accuracy of the image registration process during strip mosaicking for each sensor. For the mosaic slide-shift geolocation error, preliminary analysis with a few image pairs shows that after correction, residual geolocation errors have a maximum range of 4-6 pixels. For the 12.5 m pixel resolution, this amounts to a 50-75 m displacement error, and an absolute velocity error of ±2.77 to ±4.16 cm/s for the 30-min lag image pairs; at this point, a mean value of $\pm 3.47\ cm/s$ is used as a rough measure for the mean accuracy of MCC SAR currents. In the future, it should be possible to calculate the geolocation uncertainty from each SAR pair and assign an absolute accuracy value to each derived current field.

3.3.5 Output Current Fields Over the CCS

Each Envisat-ERS2 30-min lag image pair was processed independently, with the final results being the post-processed ocean surface current vectors. A total of 124 pairs were processed over the CCS, out of which, 15 had no vectors in the final output. The month distribution of the SAR pairs used is shown in Fig. 3.7a; these numbers depict the pairs selected from the European Space Agency (ESA) archive for their potential of containing biogenic slicks. Fig. 3.7b shows the total number of vectors generated per month; it is not surprising to see highest number of vectors in the spring-summer months when upwelling takes place in the CCS, serving as a primary source for biogenic slicks. However, this plot could be misleading because of the uneven distribution of images over the months. Instead, Fig. 3.7c shows the number of vectors normalized by the number of pairs; this plot shows clearly that more vectors are detected per image in the CCS during the spring-summer months. It should be noted here that the image pairs contain both land and ocean, and ideally the vector counts should be normalized by the total number of ocean pixels in the overlap area of the SAR image pairs, but for estimation purposes this per-pair normalization is sufficient (the assumption made here is that the overall % of land pixels would be nearly the same in all months). Also note that SAR pairs can be of different strip lengths; thus some SAR pairs could have more ocean pixels than others, which could again skew the normalized counts. However, this is also not considered to be a major factor because the longer a stripmap is, the more it would deviate from the nearshore CCS due to the coastal geometry and orbital paths, and the chances of detecting biogenic slicks reduce drastically as distance from the shore increases. In summary, the normalized monthly distribution of vectors plot in Fig. 3.7c is sufficiently correct.

The overall geographical distribution of estimated vectors is shown in Fig. 3.8 as a number density plot. The number density is calculated over a low-resolution 10 km grid for display, and depicts how many vectors were found in each grid cell for every SAR pair processed. For ease of display, the CCS has been divided into 3 portions along the coast. Majority of the vector output is over the SCB, however there are vectors off Northern California and Seattle as well.

An example of surface current generation from one pair is shown in Fig. 3.9. Envisat and ERS-2 strips for this case were comprised of two scenes each. The mosaicked Envisat and ERS-2 σ^o [dB] strips are shown in Fig. 3.9a and Fig. 3.9b, respectively. These images are speckle-filtered, subset to their mutual overlap region, and downsampled to 25 m resolution. The ERS-2 image lags the Envisat image by 30 minutes. Some ocean feature changes can be seen between the two images, however this is clearer in the difference image in Fig. 3.9c, especially in the regions to the west of Santa Catalina Island. The dark linear features in region A seem to have shifted position as a group in the two images, as evident from the alternating increase and decrease pattern seen in Fig. 3.9c. Region B also depicts change in intensity, however this is more of a homogeneous change over a relatively large region, and is not due to advection; the actual cause of this change may be changes in wind patterns, or atmosphere/ocean fronts. Due to the MCC pattern subwindow and search window size definitions, intensity changes of the kind depicted in region B, which might not be due to ocean surface advection, are automatically ignored for the most part. This can be seen in the raw MCC vector field in Fig. 3.9d: there are few vectors over region B. The raw vector field shows a nearly-constant vector flow over land, this is due to the intra-sensor geolocation error. Fig. 3.9e shows the

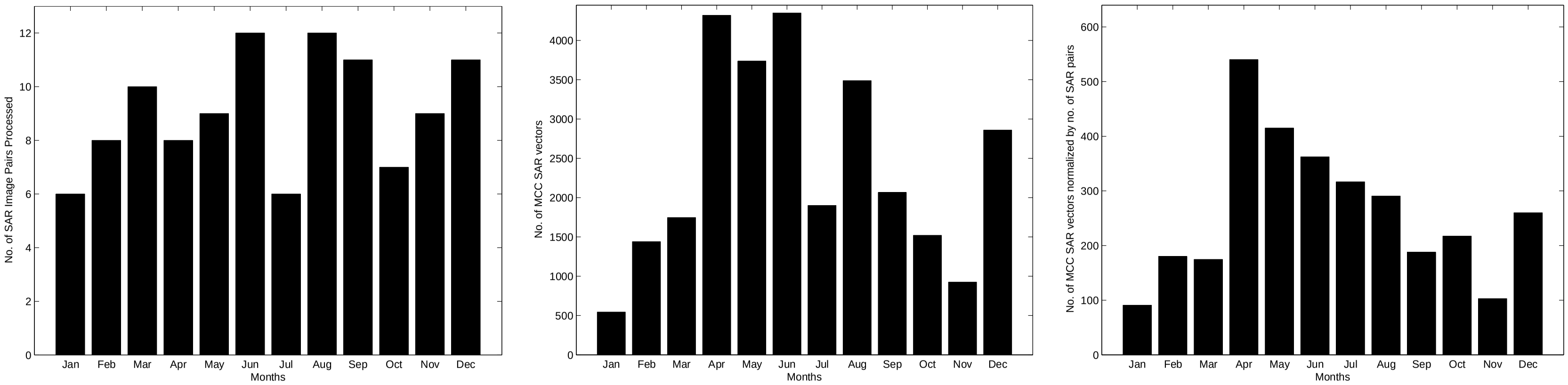

(a) Monthly distribution of No. of SAR pairs

(b) Monthly distribution of total No. of SAR vectors generated

(c) Monthly distribution of total No. of SAR vectors generated, normalized by No. of SAR pairs

Figure 3.7: Monthly counts of SAR pairs and MCC SAR generated vectors: (a) total number of SAR pairs used, (b) total number of vectors generated, and (c) total number of vectors generated, normalized by the number of SAR pairs.

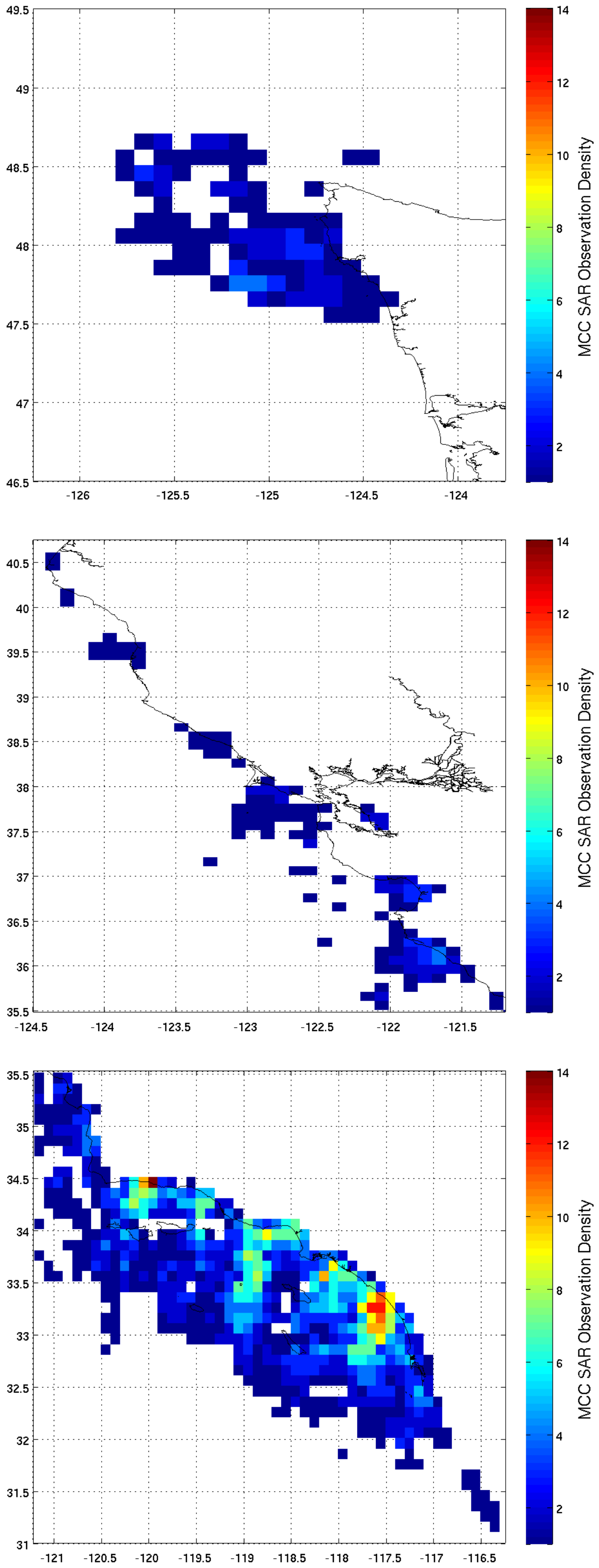

Figure 3.8: Geographical distribution of MCC SAR observation density over the CCS, divided into three regions of latitude for display.

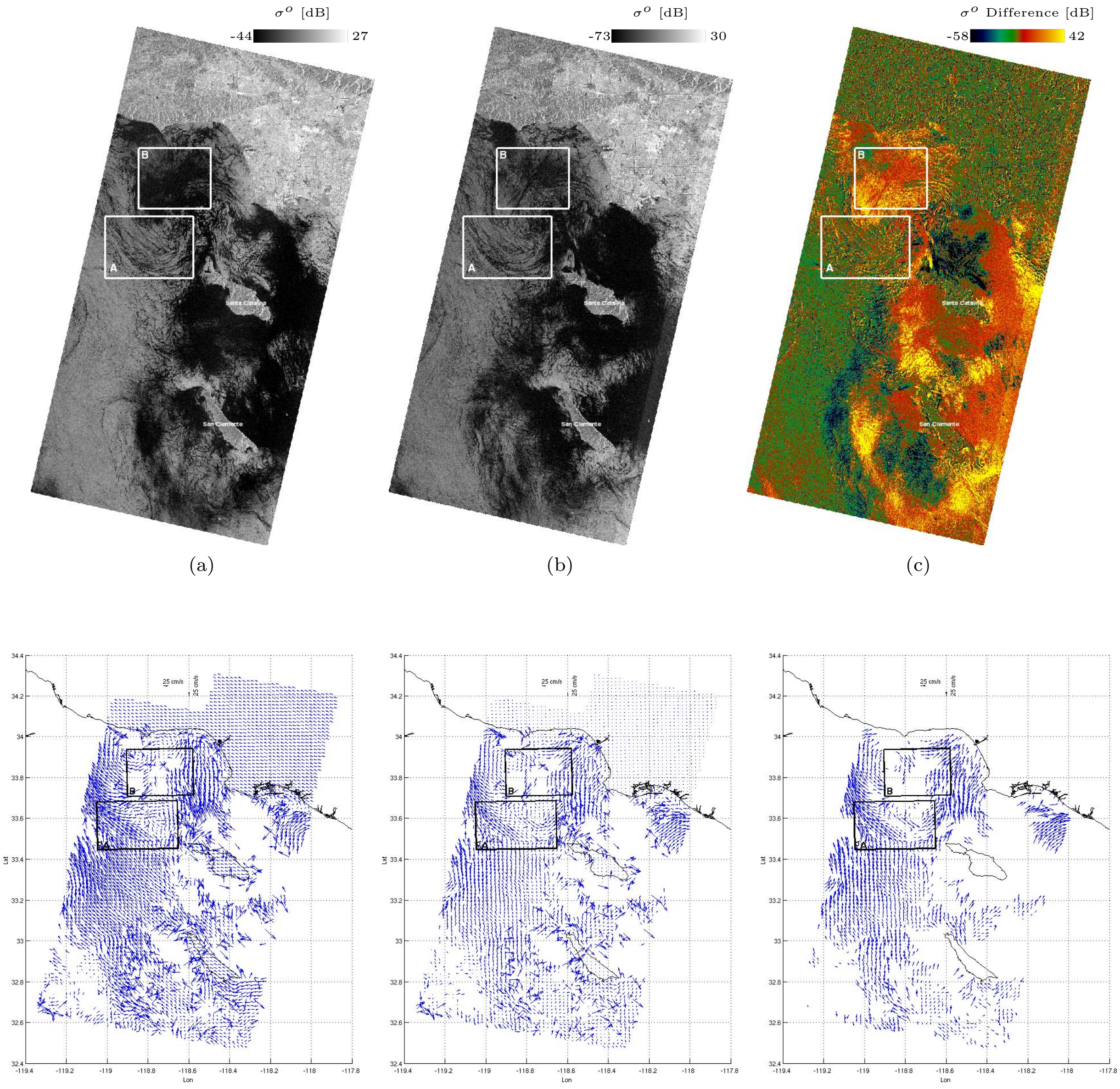

(a) (b) (c)

(d) (e) (f)

Figure 3.9: Sample case of Envisat-ERS2 30-min lag image pair processing. (a) and (b) show the calibrated σ^o [dB] Envisat and ERS-2 images, respectively. The difference image [dB] is shown in (c). (d) shows the raw MCC current field derived from the SAR image pair in (a) and (b), filtered at a cross-correlation coefficient threshold of 0.2. (e) shows the result after intra-sensor geolocation error correction. The final output vector field after post-process filtering is shown in (f). SAR data courtesy ESA.

vector field after correction for this geolocation error. The final vector output after post-process filtering is shown in Fig. 3.9f; notice the elimination of vectors that appear spurious and spatially incoherent, and what appears to be a small-scale eddy in the top left corner of Region B. Note that the vector fields shown in Fig. 3.9d and 3.9e have been filtered at a cross-correlation threshold of 0.2 for display.

Also of interest is the clockwise (anticyclonic) small eddy-type motion on the west of Box B, especially because DiGiacomo & Holt [31] have noted that most small-scale eddies in this region are cyclonic. Manual inspection of the SAR images confirms clockwise rotational motion in this region. It is to be noted that HF radar currents fail to show a complete eddy type motion here (middle panel in Fig. 3.15). Careful inspection further shows an anticlockwise (cyclonic) eddy in Box A, however the overall flow there is not that simple. Between the SAR images, there is a large backscatter change in the region around that eddy in Box A (possible due to wind changes or fronts etc.), due to which the MCC method fails to detect the whole eddy-type motion in this region. At the same time, the vectors in the bottom left portion of Box A (towards North West) depict actual motion.

3.3.6 U.S. East Coast Processing

For the sake of experiment, and to observe if the MCC SAR method works in regions other than the CCS, 18 Envisat ERS-2 image pairs were processed over the East Coast. Out of these, 7 pairs did not generate any vectors. For the 11 pairs with generated vectors, only one was over an area with some HF radar overlap. The MCC SAR vectors for this pair are plotted in Fig. 3.10 along with the HF radar vectors in their native 6 km resolution. The hourly HF radar current fields have been linearly composited (see Sec. 3.5) to bring them to the same time span as the MCC SAR currents; the HF radar vectors have not been filtered for errors. In the bottom part of the plots, both current fields show the same general velocities towards south-west. The northward turning seen in the middle part of hte plots for HF radar currents is present yet not that strong in the MCC SAR currents. In general, both current fields in Fig. 3.10 depict the same general circulation in this region.

Another interesting example can be seen in the output from another processed pair over the East Coast, shown in Fig. 3.11. This region is in the vicinity of the well-known high-velocity Gulf Stream [42, 120]. The

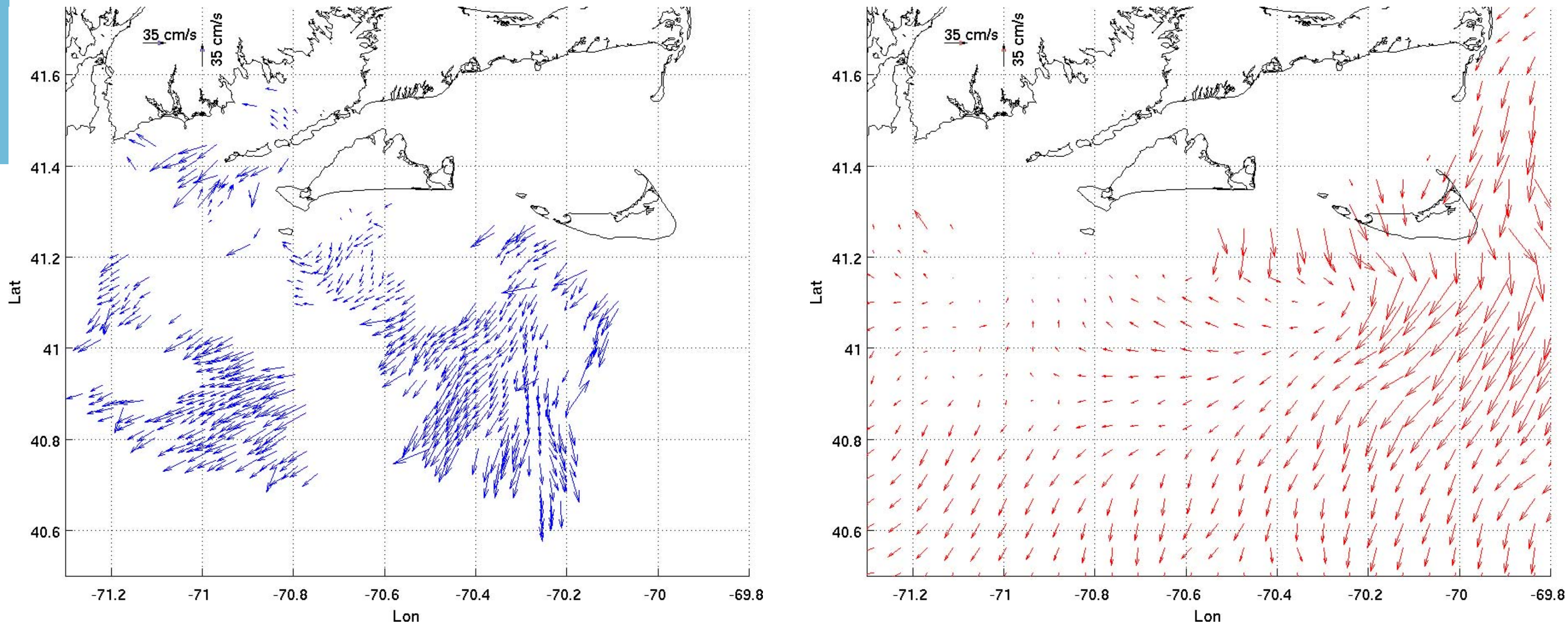

(a) MCC SAR vectors

(b) HF radar vectors

Figure 3.10: Example of coincident MCC SAR vectors (in (a)) and HF radar vectors (in (b)) over the US East Coast.

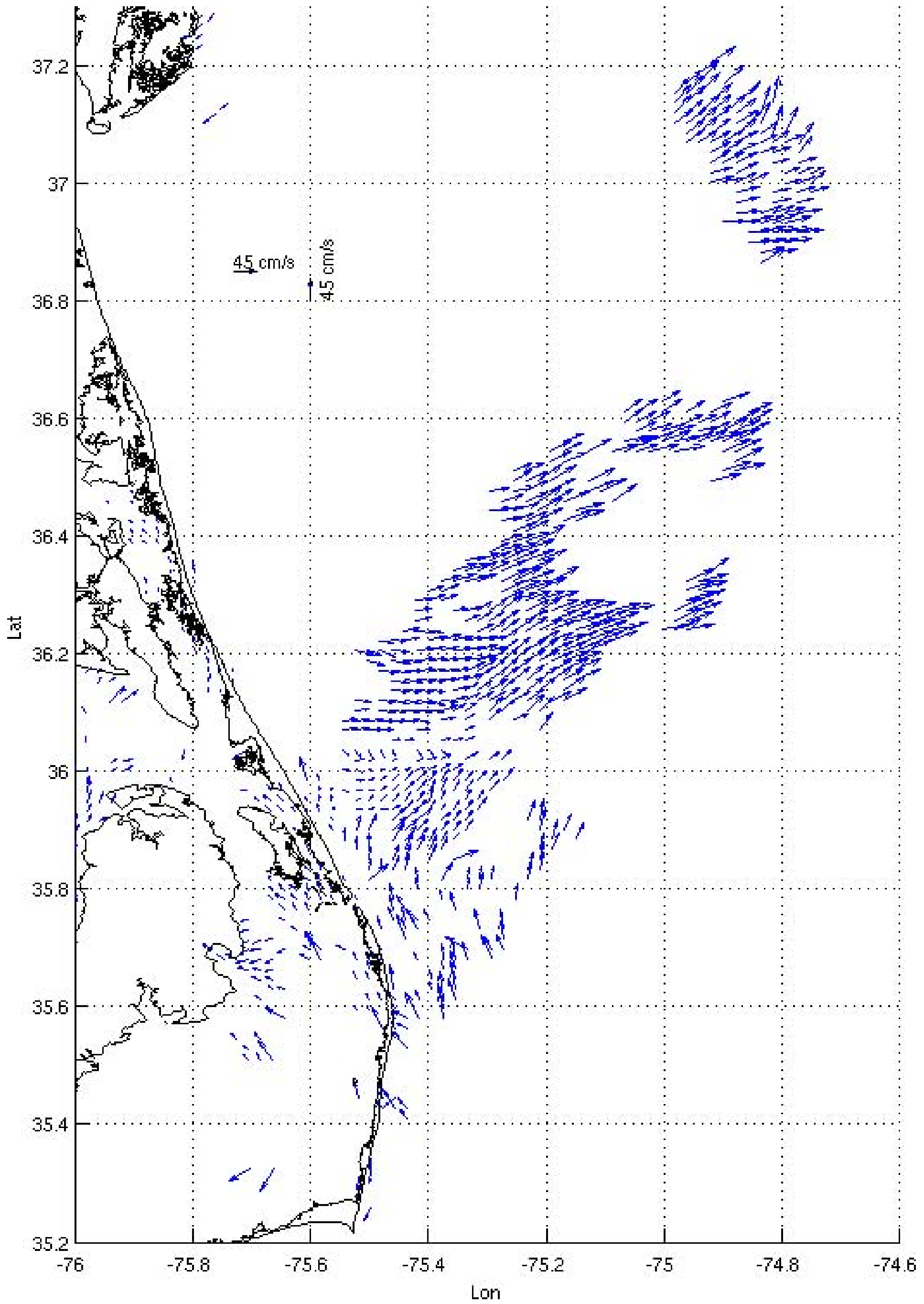

Figure 3.11: Another East Coast MCC SAR current field example. The derived vectors are similar to the general offshore Gulf Stream flow direction in this region.

derived current flow has a preferred direction, which is close to the general Gulf Stream flow direction in this region, though it may be debatable whether the Gulf Stream comes so close to the coast or not. Surface slicks have been observed near the edge of the Gulf Stream by Lyzenga & Marmorino [82] through airborne SAR, and it is possible that these slicks are entrained by the Gulf Stream, causing the near-shore flow to be in the same general direction as the actual further-offshore Gulf Stream. The sources for biogenic slicks near the edge of the Gulf Stream are suggested by Lyzenga & Marmorino [82] to be either increased biological activity in the frontal region or the mixing and advection of biologically richer coastal waters into the Gulf Stream.

It should be noted that the data processing is not optimized for the East Coast, which, in general may need a higher velocity threshold than the 60 cm/s value used for the CCS, due to the presence of high velocity Gulf Stream. The post-process filtering parameters may also need to be tweaked. The US East Coast processing is done only experimentally, and all detailed analysis that follows is performed only for the MCC SAR vectors generated over the CCS.

3.4 MCC SAR Wavenumber Spectrum Analysis

The wavenumber spectrum of ocean currents gives an insight into the kinetic energy distribution in the ocean over a range of spatial scales. Wavenumber spectra of surface velocity over the global ocean were calculated for the geostrophic case by Stammer [119] using satellite altimeter data; however that analysis was restricted to length scales of 100 km and above due to their sampling geometry and because altimeter signals become dominated by noise below length scales of ≈100 km.

In the California Current System, there is substantial velocity variance that resides in the submesoscale range. Capet et al. [19, 21] derived currents from a high-resolution numerical model of the CCS, and were able to derive wavenumber spectra in the submesoscale range down to 1.5 km. Kim et al. [73] used HF radar currents to estimate the wavenumber spectra in the CCS; the high resolution of the HF radar current fields allowed for derivation of wavenumber spectra at length scales as small as 2 km.

In the submesoscale wavenumber regime, theory predicts a power-law decay behavior. Traditional quasigeostrophic (QG) theory specifies a power-law slope of -3 [78], so called ”surface quasigeostrophic theory (SQG)" and 3D isotropic turbulence theory predicts a power-law slope of -5/3 [18, 75], and high-resolution simulations and frontogenesis theory predicts a slope of -2 [19, 21]. The submesoscale wavenumber spectra derived over the CCS using a high-resolution model [19, 21] and HF radar currents [73] both show very good agreement with the k^{-2} power law.

The MCC SAR currents have a basic resolution of ≈1.87 km and should therefore capture submesoscale circulation phenomena very well. Wavenumber spectra computed from these MCC SAR currents should therefore, agree well with the above theoretical and modeled power law spectral decay. Agreement with other spectra will also confirm that the MCC SAR velocities can be used to directly measure the surface velocity of submesoscale processes. The wavenumber spectrum calculated for the Kinetic Energy (KE) in MCC SAR currents is shown in Fig. 3.12, along with the 95% confidence interval (CI) and relevant power-law spectrum slopes: the k^{-2} slope is reproduced, with appropriate magnitude, from Fig. 1 in Capet et al. [21], while the $k^{-5/3}$ and k^{-3} slopes are arbitrary.

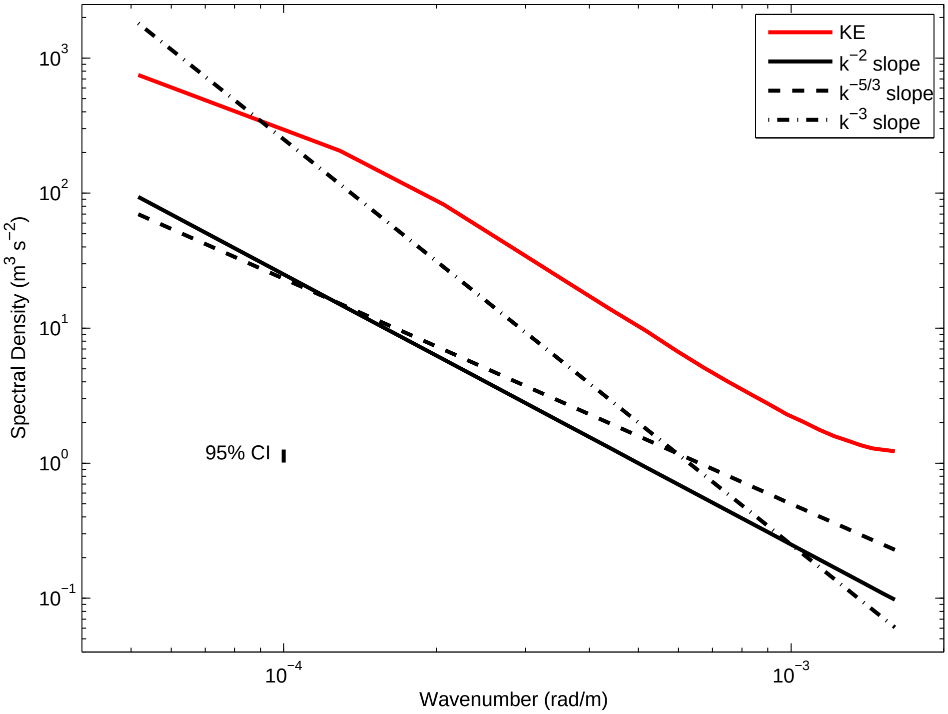

Figure 3.12: Mean KE wavenumber spectrum for MCC SAR currents, averaged over a number of different times and scenes as described in the text. Various power-law slopes are also shown. The k^{-2} slope is reproduced, with appropriate magnitude, from Fig. 1 in Capet et al. [21] while the $k^{-5/3}$ and k^{-3} slopes are arbitrary.

Each current field calculated from a 30-min lag image pair was re-gridded via linear interpolation to a constant 1.9 km resolution field. One-dimensional KE spectra were calculated over these re-gridded vectors, separately along the x-direction (each line of constant latitude) and the y-direction (each column of constant longitude); prior to this, each row/column was conditioned by a Hann window (see Appendix D for specifics on how the spectra were calculated). All of these 1-D spectra from one current field were then averaged together to generate mean 1-D x-direction and y-direction spectra for one field. The spectra for x- and y-directions were found to be very similar (see Appendix E), and for each field, a mean 1-D spectrum representative of the 2-D spectra was generated by averaging the x- and y-direction spectra. This mean KE spectrum for each field was band-averaged to increase the 95% CI. Out of the total 124 processed 30-min lag image pairs, only 96 current fields were used for the wavenumber spectral analysis; other pairs either had less than 15 vectors, or did not produce enough vectors after re-gridding and interpolation to a 1.9 km grid. The overall mean KE spectrum shown in Fig. 3.12 was produced by taking an overall mean of the individual mean spectra from each current field.

The MCC SAR vectors seem to follow the k^{-2} power law in the wavenumber range of 10^{-4} rad/m to 10^{-3} rad/m, in excellent agreement with the kinetic energy spectrum from the model of Capet et al. [21]. The slightly different behavior in the wavenumber range $<10^{-4}$ rad/m may be due to the fact that the 1.9 km interpolation grid is set up over the minimum and maximum distance from the shore present in each derived currents field. Since the features of interest, surface slicks, predominantly exist close to the coast, the probability of detecting vectors gets less as distance from the coast increases. At the same time, all spectra are calculated at a fixed wavenumber resolution and length (by zero-padding during spectra calculation) to achieve constant wavenumbers for all cases for calculating the means. Both of these factors combine to cause larger interpolation errors in the spectra calculation in regions farther from the coast. The tenfold magnitude difference between the calculated spectrum and the k^{-2} slope from Capet et al. [21] may be explained by the many differences between the MCC SAR derived currents and the Capet model: i) the model ignores the ocean region very close to the coast (<50 km distance from the coast) while the MCC SAR vectors are primarily in the nearshore region, ii) the Capet model doesn't include contributions of Stokes drift or waves, and iii) the velocities are at 10 m depth in the ocean, which are not exactly the same as the surface velocities measured by MCC SAR. On the whole, the KE wavenumber spectrum in Fig. 3.12 indicates consistency between spectra derived from MCC SAR currents, high-resolution models, and HF radar currents in the CCS. This also shows that MCC SAR currents can be used to directly measure the surface velocity of submesoscale processes.

Although Fig. 3.12 shows that the log-spectrum calculated from MCC SAR vectors seems to follow a slope of -2, this slope agreement can be further assessed quantitatively using statistical hypothesis testing. Assuming that the log-spectrum has a constant slope in the wavenumber regime being studied here, a linear regression fit can be estimated, and the estimated slope of this regression line can be subjected to t-test with respect to a reference slope. For linear regression, the t-test statistic is given in this case by [133]:

$$t = (b - \beta)\sqrt{n-2}\sqrt{\frac{\sum_{i=1}^{n}\left[\left(W_i - \bar{W}_i\right)^2\right]}{\sum_{i=1}^{n}\left[\left(S_i - \hat{S}_i\right)^2\right]}} \tag{3.1}$$

where b is the estimated linear regression slope, β is the reference slope value, n is the number of points in the spectrum, W_i are the log-wavenumber values, $\bar{W}_i$ is the mean value of the log-wavenumbers, S_i are the log-spectrum values, and $\hat{S}_i$ are the log-spectrum values estimated by linear regression at the log-wavenumber values W_i.

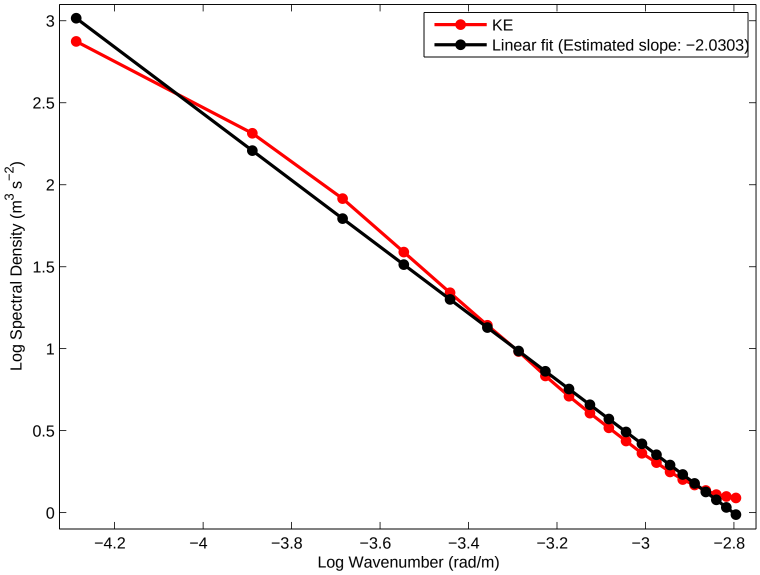

Figure 3.13: Linear regression fit over the mean KE wavenumber spectrum for MCC SAR currents. The linear fit has a slope of -2.0303.

The linear regression fit over the log-spectrum calculated in Fig. 3.12 is shown in Fig. 3.13; the linear fit has an estimated slope of -2.0303. Table 3.1 summarizes hypothesis testing using Eqn. 3.1 for the t-test over the estimated slope. The null hypothesis is set up to be $H_o:\ b = \beta$. For a reference slope of $\beta = -2$, the calculated t-value is less than the critical t-value ($t < t_c$) and the P-value is greater than the significance level ($P > \alpha$); this means that the null hypothesis cannot be rejected for this case and thus the difference between the estimated slope of the regression line and $\beta = -2$ is not significant at 95% confidence level. For a reference slope of $\beta = -5/3$, the calculated t-value is greater than the critical t-value ($t > t_c$) and the P-value is less than the significance level ($P < \alpha$); this means that the null hypothesis is rejected for this case and thus the difference between the estimated slope of the regression line and $\beta = -5/3$ is significant at 95% confidence level. To summarize, the t-test rejects the $k^{-5/3}$ power law at 95% confidence level, while deviation from the k^{-2} power law is insignificant at the 95% confidence level.

3.4.1 Seasonal Wavenumber Spectra

Because of summer upwelling in the CCS, especially along the California Coast, it is instructive to look at the wavenumber spectra for summer (maximum upwelling) and winter (very low upwelling activity). The development of surface variability in the CCS is known to be seasonal, with late summer containing more mesoscale features as compared to winter; the mesoscale energy is transferred to smaller scales via instability [23,62]. Wavenumber spectra calculated for the months of January and June, chosen respectively as representative months for winter and summer, are shown in Fig. 3.14. These spectra are calculated in the same way as the spectrum in Fig. 3.12, with one difference: the region of interest is only along the California Coast (starting from the SCB in the South and up North till approximately 40 deg latitude). A total of 5 current fields were used for the January spectrum, and a total of 12 current fields were used for the June spectrum. They both seem to follow the general k^{-2} slope, however, the difference between their amplitudes is marked in the lower wavenumbers. The small 95% CI indicates that this magnitude difference is statistically significant. The higher amplitude in the lower wavenumbers for June is consistent with the difference in instability features between summer and winter in the CCS, indicating the nonlinear effects of baroclinic instability in the summer. Strub & James [122] show similar seasonal behavior in wavenumber

Table 3.1: Statistical hypothesis tests for MCC SAR wavenumber spectrum slope at $\alpha = 0.05$ significance level. The t-test is used for the estimated slope of a linear regression line over log-wavenumber (independent variable) and log-spectrum (dependent variable) values. The t-test indicates that the slope value of $-5/3$ is rejected, while deviation from the slope value of -2 is insignificant at the 95% confidence level.

Reference Slope	Null Hypothesis	Significance Level	Calculated t-value	Critical t-value	P-value	Decision
$\beta = -2$	$H_o: \ b = \beta$	$\alpha = 0.05$	$\lvert t \rvert = 0.7702$	$t_c = 1.7291$	0.4506	H_o not rejected
$\beta = -5/3$	$H_o: \ b = \beta$	$\alpha = 0.05$	$\lvert t \rvert = 9.2313$	$t_c = 1.7291$	1.8783×10^{-8}	H_o rejected

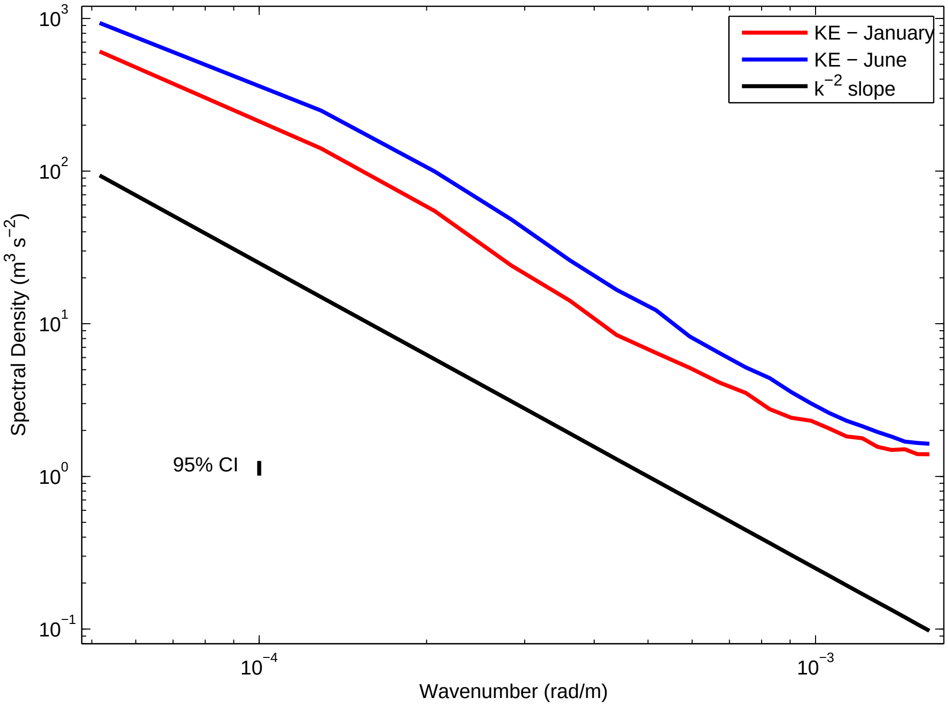

Figure 3.14: Mean KE wavenumber spectra for MCC SAR currents for January and June over the California Coast, calculated in the same manner as in Fig. 3.12.

spectra derived from geostrophic currents based on altimetry observations (see Fig. 8 in that reference).

3.5 MCC SAR and HF Radar Currents Analysis

Coast-based HF radar stations are rapidly developing into an observational tool for ocean surface currents over the US West Coast for the last few years. There have been quite a few validation studies which show their general agreement with other current measurements, ranging from 1 to 19 cm/s (see [73] for a good summary). High frequency radar stations are a unique resource in that they measure surface currents in the coastal zone at high spatial and temporal resolutions, which are difficult to achieve using other methods.

High frequency radar currents datasets over the US California Coast are available at two different spatial resolutions: 2 km and 6 km. MCC currents derived from SAR are compared with both 2 km and 6 km resolution HF radar currents separately. Before comparison, the HF radar currents were filtered at a normalized uncertainty index threshold[a] of 0.8 for both u- and v-components [72]. MCC SAR currents were re-gridded to 2 km and 6 km resolutions for comparison with the HF radar datasets at the same resolution. After re-gridding, any MCC SAR grid points which were at a distance of greater than half the grid resolution from the original grid points were omitted from further analysis. To remove gridding artifacts, velocity vectors with magnitude less than 1 cm/s were discarded. Also, any interpolated grid points which did not have both MCC SAR and HF radar current vectors, and any cases which had less than 6 coincident re-gridded vectors were omitted from further analysis. The HF radar current fields at an hourly temporal resolution were composited by linear weighting (following the method in Chubb et al. [24]) to bring them to the same time span as the MCC SAR currents. Some sample plots of re-gridded MCC SAR and HF radar vectors are shown for both the 2 km and 6 km resolution case in Fig. 3.15. The vector fields in each plot are scaled together to the same reference vector. Both MCC SAR and HF radar vectors show the same general circulation, however some disagreements can also be seen in these sample plots.

3.5.1 Overall Data Distributions

To get a general view of the current fields from MCC SAR and HF radar measurements, it is useful to take a look at their overall data distributions. The following discussion uses the 2 km re-gridded coincident MCC SAR and HF radar current datasets for analysis; the results from 6 km re-gridded coincident datasets are very similar and are thus not discussed here (see Appendix F).

The histograms for magnitude and direction are plotted for both datasets in Fig. 3.16. The magnitude distributions in Fig. 3.16a and 3.16b are similar in nature, but MCC SAR magnitudes peak at a higher value than HF radar magnitudes. This is indicative of a +ve magnitude bias in the MCC SAR measurements, which is about ≈11 cm/s. Note that HF radar currents have only a few values >60 cm/s, which are not shown in Fig. 3.16b. The velocity direction distributions in Fig. 3.16c and 3.16d appear similar overall, with similar mean values, the major difference being the inability of MCC SAR to capture as many North-South direction currents as HF radar measurements.

---

[a] See Sec. 1.6.2.1 for description

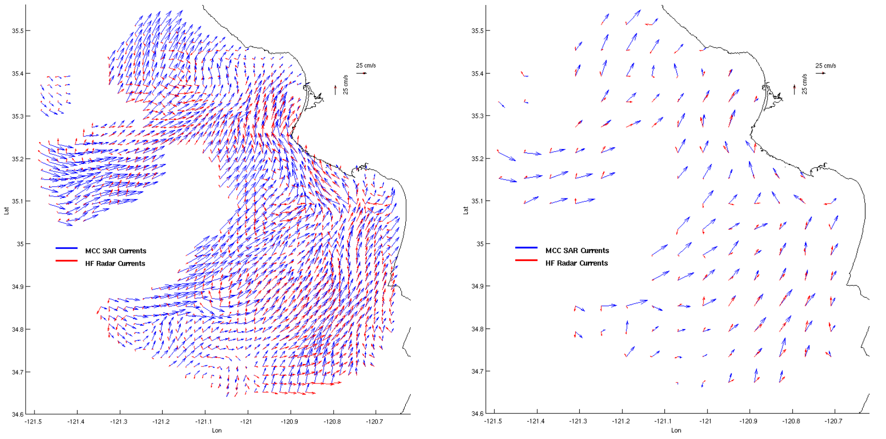

Re-gridded: 2 km resolution Re-gridded: 6 km resolution

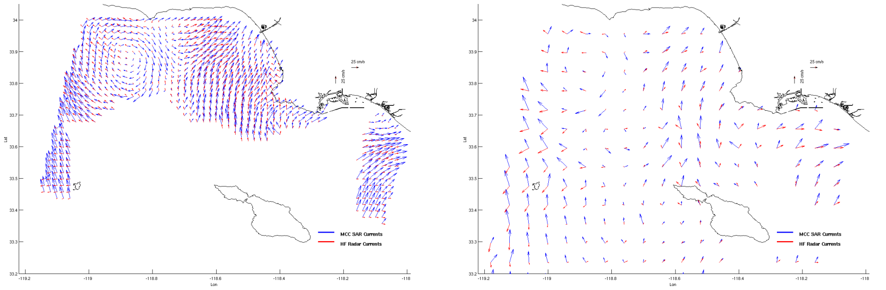

Re-gridded: 2 km resolution Re-gridded: 6 km resolution

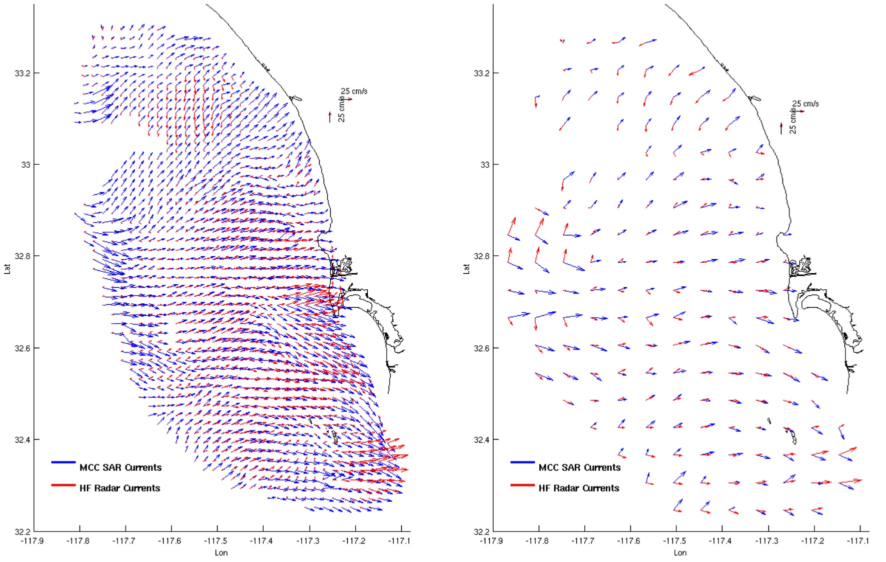

Re-gridded: 2 km resolution Re-gridded: 6 km resolution

Figure 3.15: Some sample plots of the MCC SAR vectors re-gridded to the overlapping HF radar datasets of 2 km (plots on the left) and 6 km (plots on the right) resolutions. The top, middle, and bottom panel each show processed MCC SAR vectors over different regions, along with the HF radar vectors. In each plot, the vectors are scaled to the same reference vector.

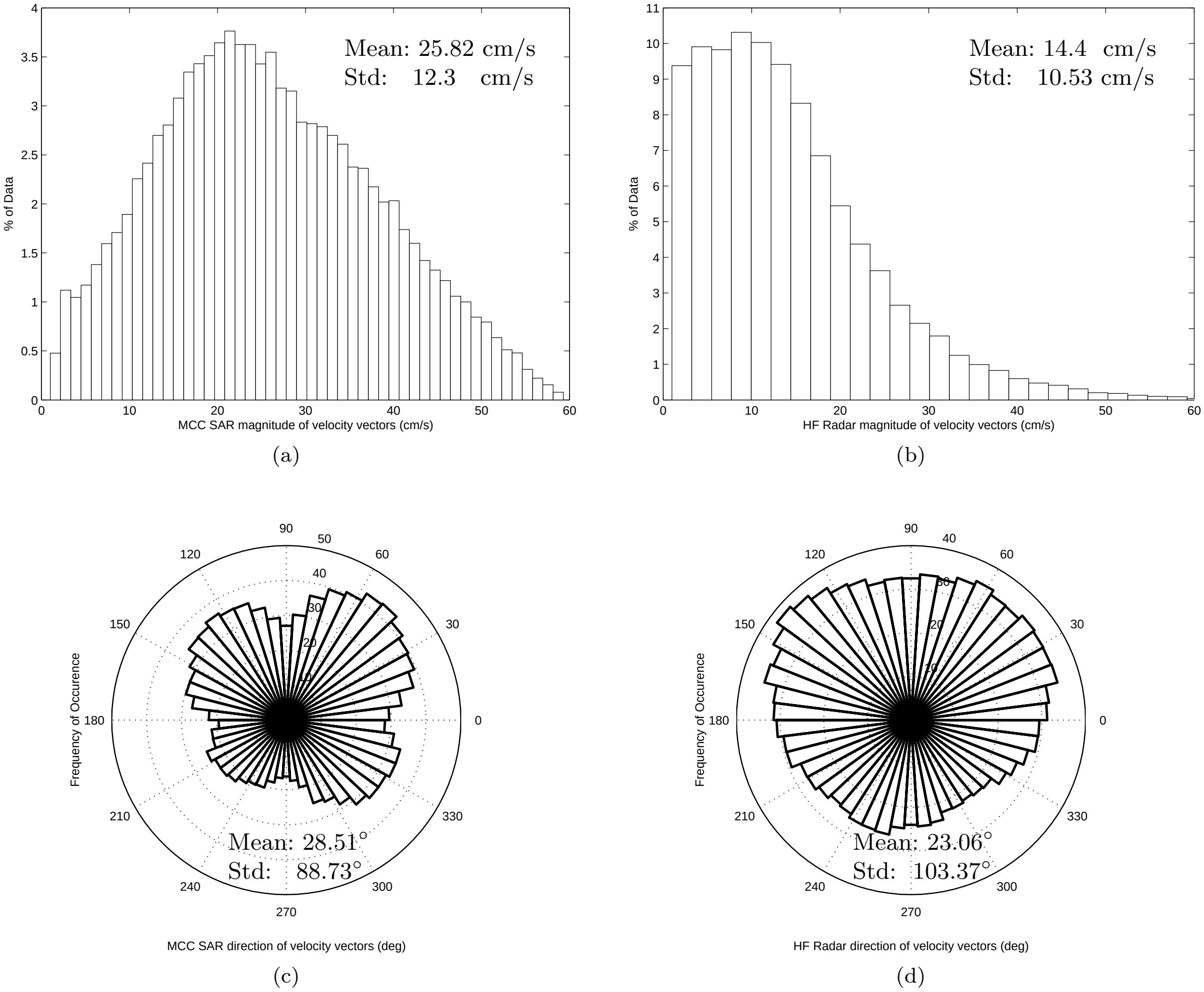

Figure 3.16: Histograms of data distributions for magnitude and direction ((anti-clockwise from East) of re-gridded coincident MCC SAR and HF radar currents. (a) and (b) are histograms for velocity magnitudes of MCC SAR and HF radar currents, respectively. (c) and (d) are histograms for velocity directions of MCC SAR and HF radar currents, respectively.

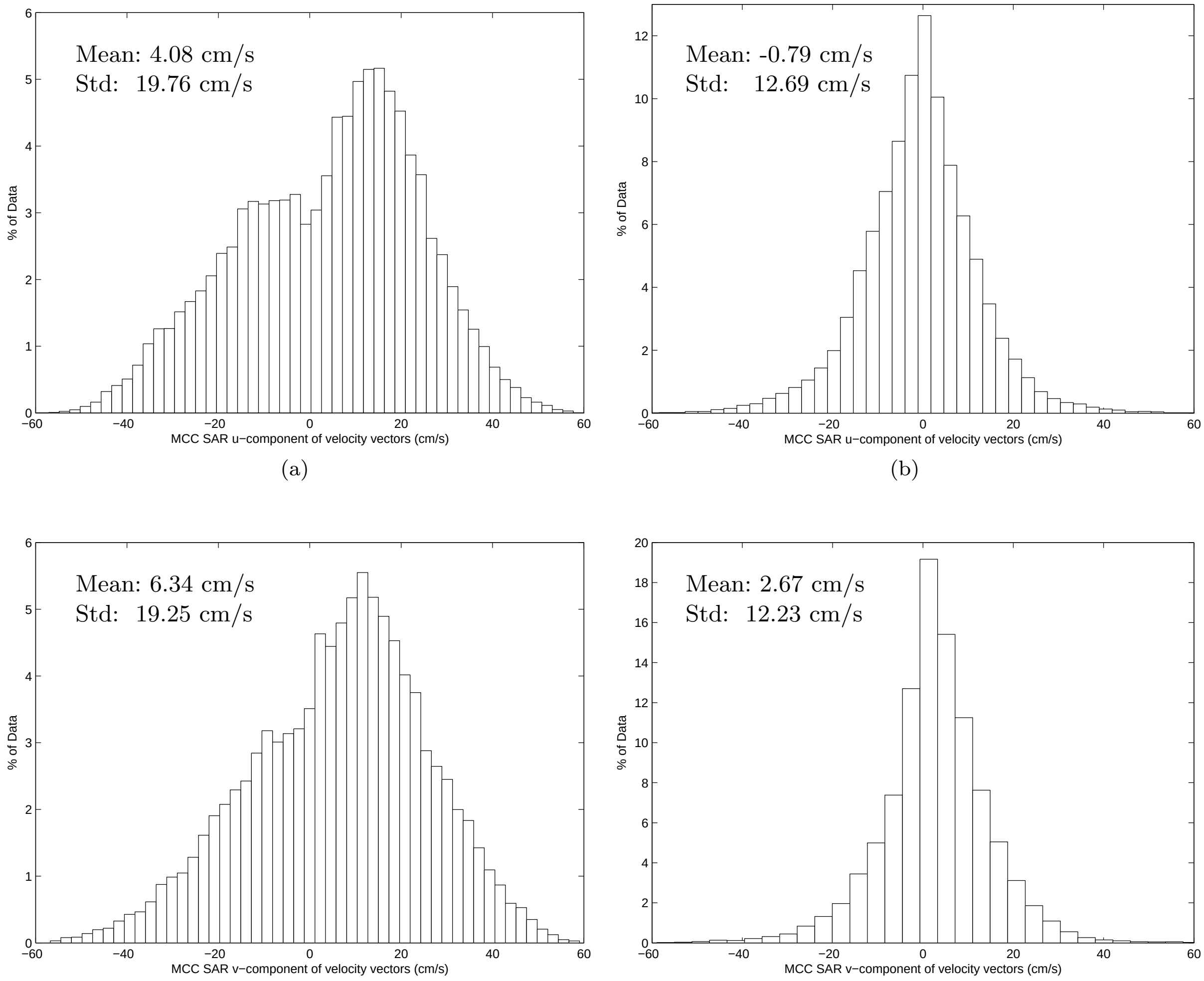

(a) (b)

(c) (d)

Figure 3.17: Histograms of data distributions for vector components of re-gridded coincident MCC SAR and HF radar currents. (a) and (b) are histograms for the u-component of MCC SAR and HF radar currents, respectively. (c) and (d) are histograms for the v-component of MCC SAR and HF radar currents, respectively.

The histograms for u- and v-components of the vectors currents are plotted for both datasets in Fig. 3.17. Once again, a +ve bias can be seen in the overall distributions for MCC SAR components. It is also interesting to note indications of a small peak on the -ve side for both MCC SAR vectors components. For HF radar vector components (Fig. 3.17b and 3.17d), the few values >|60| cm/s are not shown in the plots.

3.5.2 Complex Correlation

To get a quantitative measure of how well the MCC SAR and HF radar current fields agree, their complex correlation was calculated. Complex correlation is defined as follows (after [76]):

$$\rho = \frac{\langle V_{MCCSAR}\cdot V^*_{HFR}\rangle}{\sqrt{\left[\langle V_{MCCSAR}\cdot V^*_{MCCSAR}\rangle\langle V_{HFR\cdot V^*_{HFR}}\rangle\right]}} = |\rho|\, e^{i\phi} \tag{3.2}$$

where the 2-D velocity field (u, v) for either MCC SAR or HF radar vectors is represented as a complex number V, defined by: $V = u + i\cdot v$, and V^* is its complex conjugate.

The average magnitude correlation coefficient $|\rho|$ is defined as:

$$|\rho| = \sqrt{[Re\,(\rho)]^2 + [Im\,(\rho)]^2} \tag{3.3}$$

and the average angular phase difference between the MCC SAR and HF radar current fields is defined as:

$$\phi = \tan^{-1}\left[\frac{Im\,(\rho)}{Re\,(\rho)}\right] \tag{3.4}$$

Physically, the magnitude correlation is a measure of the relative magnitude variations between the two datasets. The phase angle gives the mean counter-clockwise rotation of the HF radar current vectors with respect to the MCC SAR vectors, and is meaningful only when the magnitude correlation is high.

Complex correlation was computed for each set of coincident MCC SAR and HF radar vectors, and its overall distributions, along with the mean and RMS values, are shown in Fig. 3.18 for 2 km re-gridded currents (Fig. 3.18a, 3.18b) and for 6 km re-gridded currents (Fig. 3.18c, 3.18d).

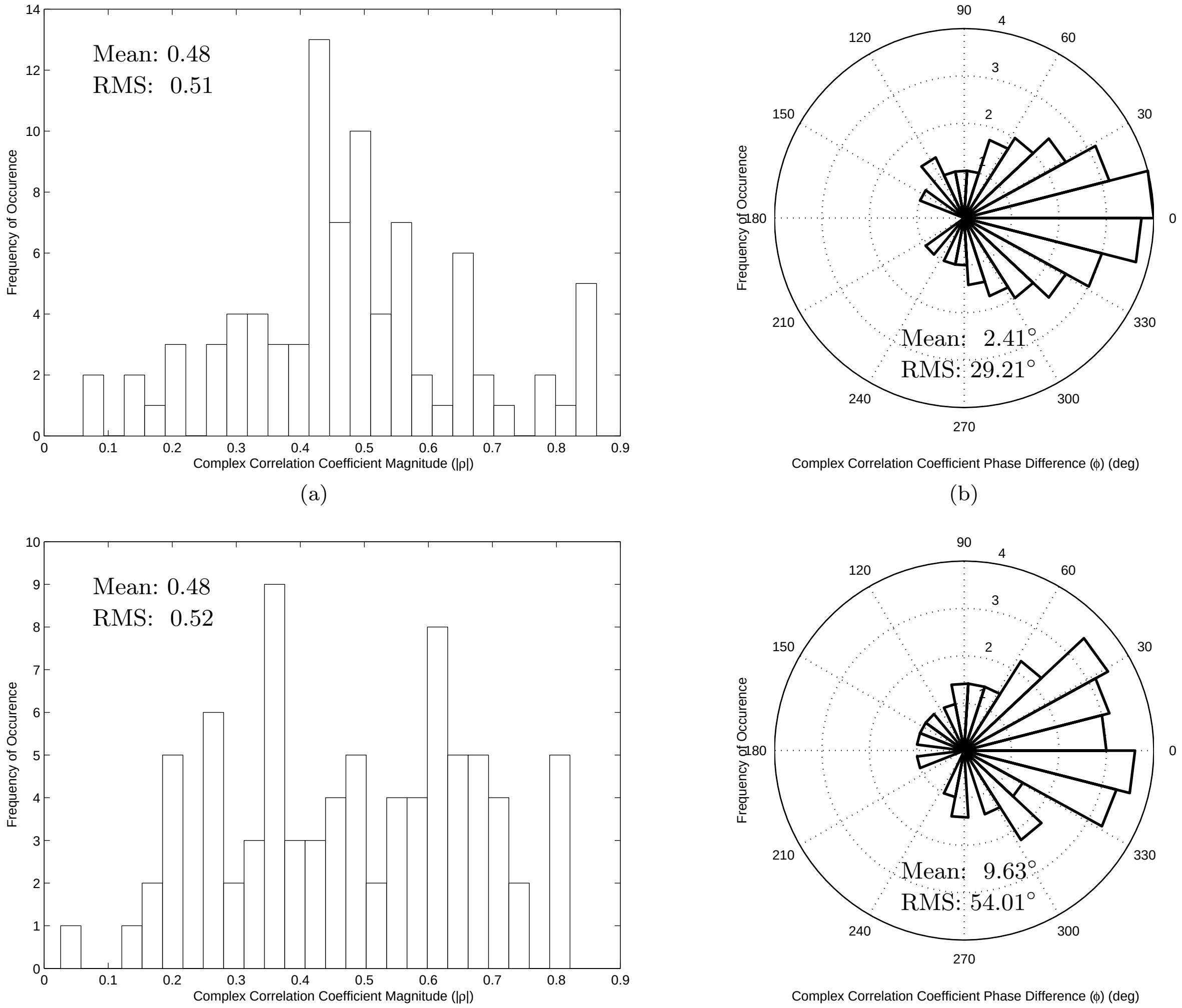

(a) (b) (c) (d)

Figure 3.18: Histograms of complex correlation magnitude and phase difference between re-gridded SAR MCC and HF radar currents. The top row is for the 2 km resolution HF radar currents, while the bottom row is for 6 km resolution HF radar currents. (a) and (c) are histograms for complex correlation magnitude, (b) and (d) are histograms for complex correlation phase difference (anti-clockwise from East). The mean and RMS values for each case are indicated in the plots.

Although mean values of $|\rho|$ are not ideal, still some insight can be gathered from the ϕ values. The positive mean values of ϕ for both 2 km and 6 km cases indicate that the MCC SAR vectors are oriented anti-clockwise relative to HF radar vectors. Although mean values of $|\rho|$ are not ideal, still some insight can be gathered from the ϕ values. The positive mean values of ϕ for both 2 km and 6 km cases indicate that the MCC SAR vectors are oriented anti-clockwise relative to HF radar vectors. The RMS values for ϕ are a measure of whether or not the vectors are oscillating together in direction; the RMS value for the 2 km dataset (29.21°) appears reasonable, while for the 6 km dataset, the RMS values seems unreasonably high (54.01°).

Overall, the complex correlation of 2 km datasets gives better results than the 6 km datasets. This is expected, because at the native measurements resolution of 6 km, HF radar datasets are fundamentally measuring current features of different scales, while the higher resolution features captured in MCC SAR currents may not translate into larger scale features just by down-sampling and re-gridding to 6 km resolution.

3.5.3 Analysis of Residuals

For further quantitative comparison of the two datasets, their residuals were calculated and analyzed. Fig. 3.19 shows the histograms of residuals for magnitude and direction (anti-clockwise from East) for 2 km HF radar currents subtracted from re-gridded 2 km MCC SAR currents (Fig. 3.19a, 3.19b) and for 6 km HF radar currents subtracted from re-gridded 6 km MCC SAR currents (Fig. 3.19c, 3.19d). Mean and standard deviation values for each set of residuals are also noted. The magnitude residuals for both 2 km and 6 km resolutions are quite symmetric about the mean, are unimodal, and show some agreement to the estimated normal histograms. However, the magnitude residuals do have a significant non-zero mean, ≈11 cm/s, for both 2 and 6 km resolutions. The direction residuals have a wide bias but the +ve mean values (5.45° for the 2 km datasets, 11.47° for the 6 km datasets) indicate a general anti-clockwise rotation of MCC SAR vectors relative to HF radar vectors, in agreement with the general observation from complex correlation analysis. The MCC SAR currents agree somewhat with the HF radar currents in identifying current vector direction, and have higher magnitudes than HF radar currents; possible reasons for this magnitude difference are discussed in Chap. 5.

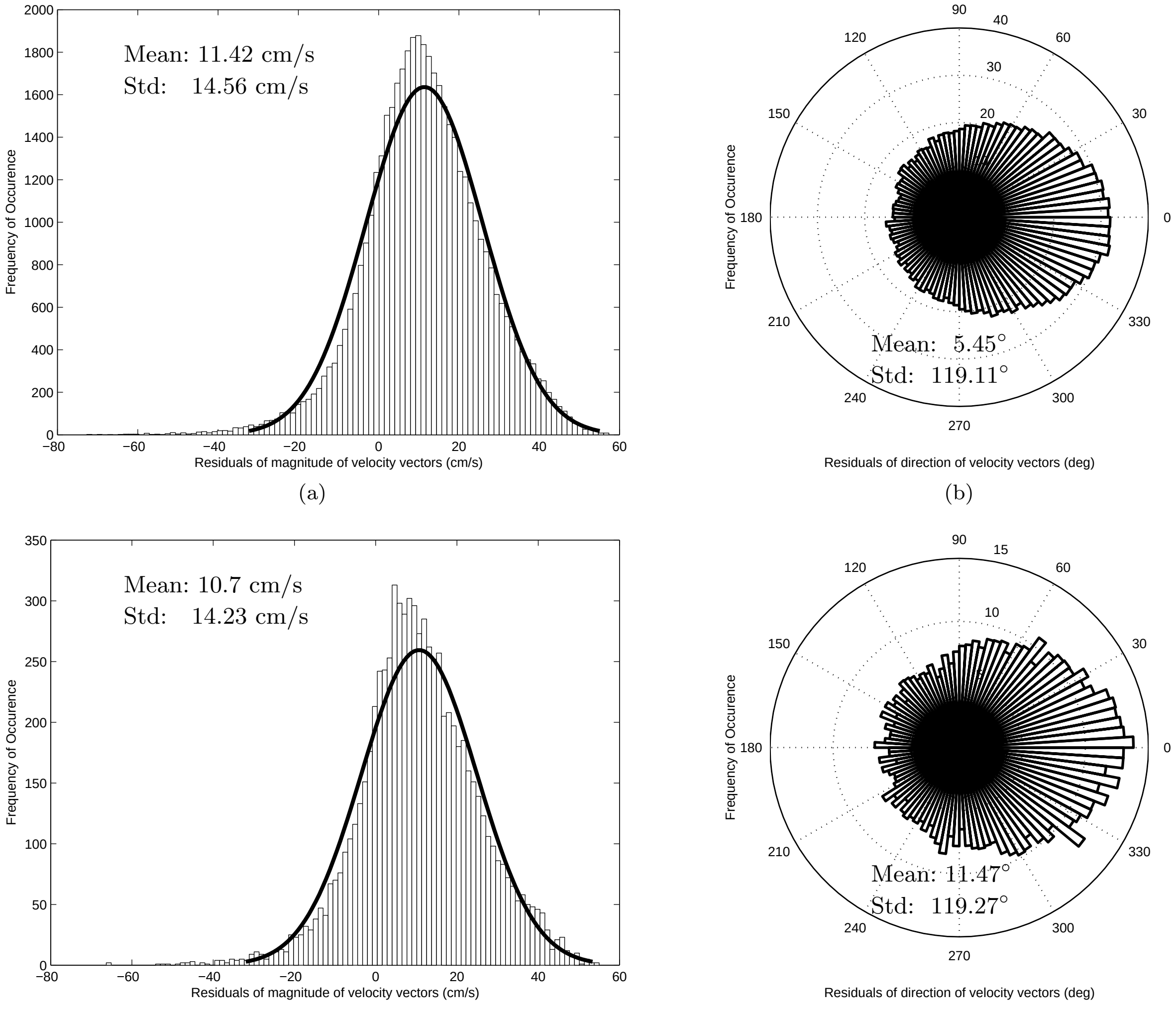

(a) (b)

(c) (d)

Figure 3.19: Histograms of residuals for magnitude and direction of re-gridded MCC SAR and HF radar currents. The top row is for the 2 km resolution HF radar currents, while the bottom row is for 6 km resolution HF radar currents. (a) and (c) are residual histograms for magnitude, (b) and (d) are residual histograms for direction (anti-clockwise from East). The thick black lines in (a) and (c) are the normal histograms estimated from the mean and variance in the respective residuals. The mean and standard deviation for each case is indicated in the plots.

Fig. 3.20 shows the histograms of residuals for u-component (zonal component) and v-component (meridional component) for 2 km (Fig. 3.20a, 3.20b) and 6 km resolutions (Fig. 3.20c, 3.20d) as in Fig. 3.19. The thick black lines are the normal histograms estimated from the mean and variance in the respective residuals. Mean and standard deviation values for each set of residuals are also noted. The residuals for both 2 km and 6 km resolutions are quite symmetric about the mean, are unimodal, and show some agreement to the estimated normal histograms. The means for the u- and v-component residuals are non-zero, positive, and have approximately the same values. For both 2 km and 6 km resolutions, this can be interpreted as showing that the increased magnitude in MCC SAR currents is distributed somewhat evenly in both the u- and v-components.

Since the area of study is in the near-shore region, it would be interesting to examine the along- and cross-shore components of the current fields. The along- and cross-shore rotation is performed by an anti-clockwise coordinate system rotation of 45°. The histograms of the residuals for the along- and cross-shore components of the MCC SAR and HF radar vector fields are presented in Fig. 3.21, calculated in the same way as Fig. 3.20. Fig. 3.21a and 3.21b show the residuals for the 2 km resolution while Fig. 3.21c and 3.21d show the residuals for the 6 km resolution. The histograms are again unimodal and symmetrical about the mean, and show some agreement to the estimated normal histograms. However, for both the 2 km and 6 km resolutions, a marked difference can be observed between the means: the means for the cross-shore components are close to 0 while the means for the along-shore components have a significant positive value (≈6-7 cm/s). It seems that the cross-shore component has very good agreement while the along-shore component has higher magnitudes for MCC SAR. It should be noted here that the actual velocity measurements of HF radar stations are only cross-shore radial velocities, and radial velocities from two or more HF radar stations are used to acquire a full 2-D vector solution, where each radial measurement is considered to be a linear combination of the full 2-D vector current components [72]. This process of conversion of multiple measured radials to a 2-D vector imparts higher errors to the interpolated along-shore component as compared to the directly observed cross-shore component. It seems that MCC SAR currents have good agreement with the higher accuracy cross-shore HF radar components, while the MCC SAR along-shore components have higher magnitudes than the lower accuracy along-shore HF radar components.

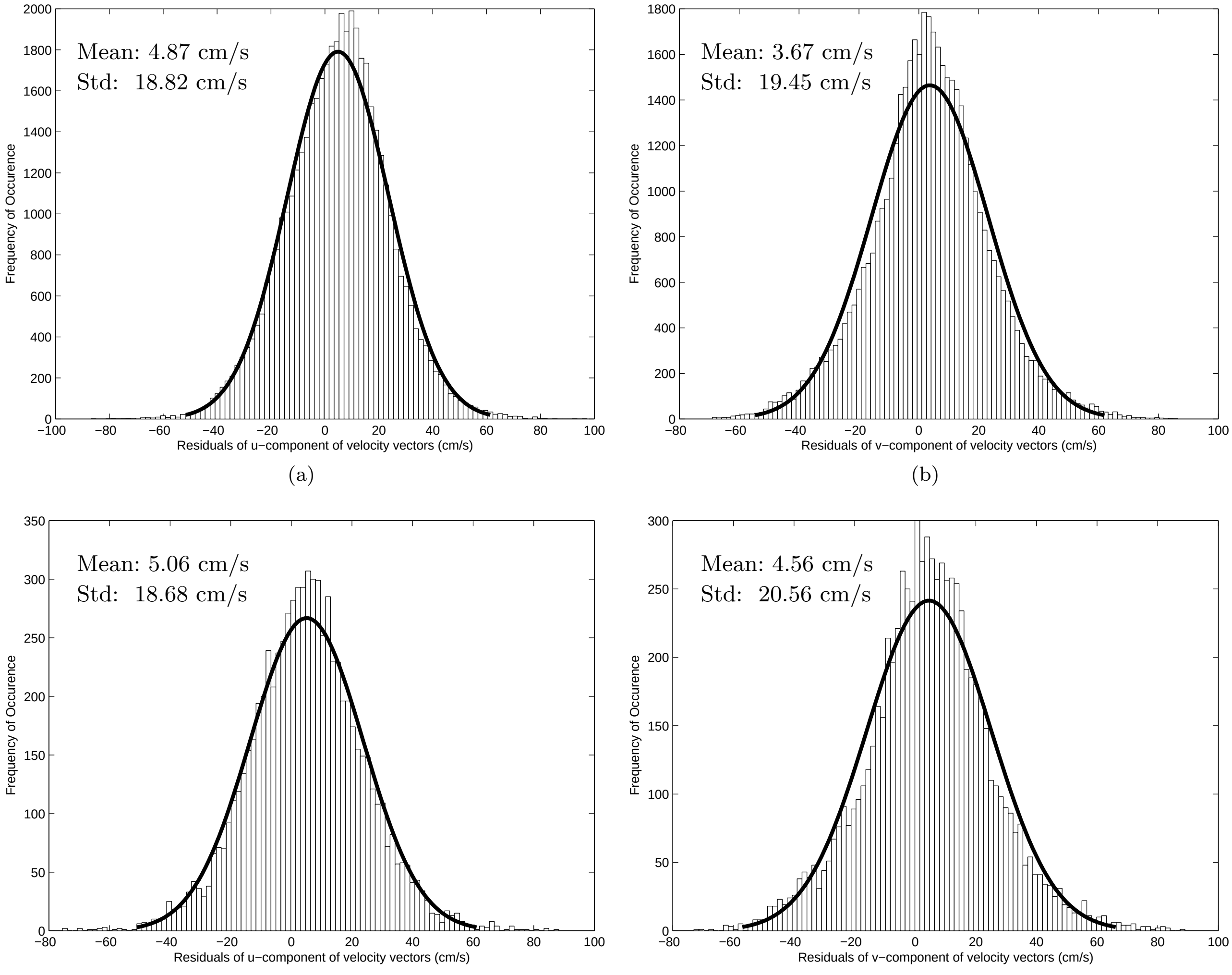

(a) (b)

(c) (d)

Figure 3.20: Histograms of residuals for vector components of re-gridded MCC SAR and HF radar currents. The top row is for the 2 km resolution HF radar currents, while the bottom row is for 6 km resolution HF radar currents. (a) and (c) are residual histograms for the u-component, (b) and (d) are residual histograms for the v-component. The thick black lines in are the normal histograms estimated from the mean and variance in the respective residuals. The mean and standard deviation for each case is indicated in the plots.

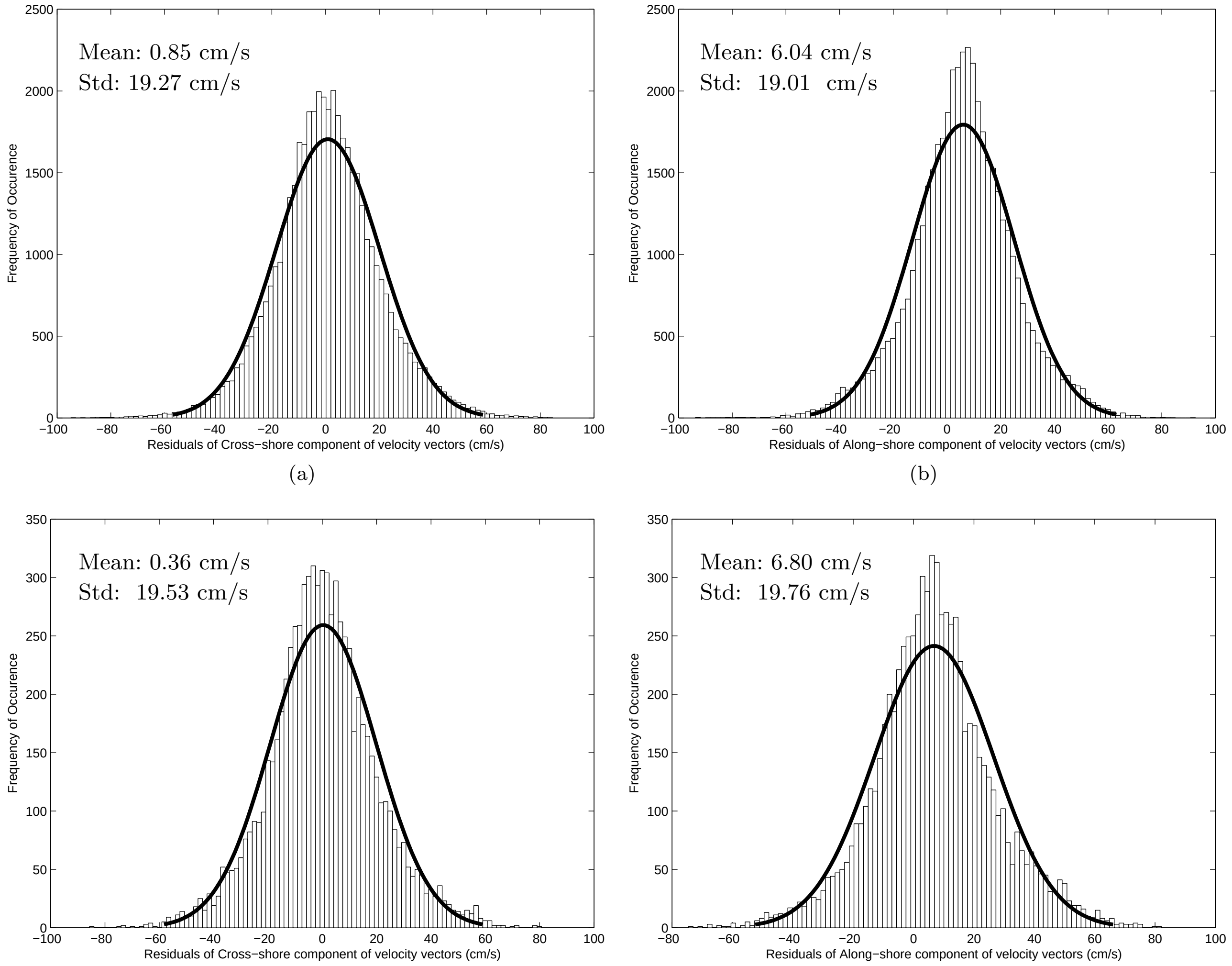

(a) (b)

(c) (d)

Figure 3.21: Histograms of residuals for cross-shore and along-shore components of re-gridded MCC SAR and HF radar currents. The top row is for the 2 km resolution HF radar currents, while the bottom row is for 6 km resolution HF radar currents. (a) and (c) are residual histograms for the cross-shore component, (b) and (d) are residual histograms for the along-shore component. The thick black lines in are the normal histograms estimated from the mean and variance in the respective residuals. The mean and standard deviation for each case is indicated in the plots.

3.6 Doppler Centroid and HF Radar Radial Currents Analysis

Doppler Centroid radial currents computed from Envisat Wide Swath Mode (WSM) images have previously been compared in the greater Agulhas Current system to geostrophic radial currents derived from CNES-CLS09 mean dynamic topography (MDT) and Sea Surface Height (SSH) anomalies, and surface drifter current measurements [113]. In the Norwegian Sea, Doppler Centroid radial currents were compared with geostrophic radial currents from many measurement sources [56].

A total of 49 Envisat WSM images from 2008-2009 were used to derive Doppler Centroid radial currents in the CCS. The processing details are described in [55, 56]. Out of these, 36 were over the California coastal region and the radial current fields derived from these were used to perform comparisons with 6 km resolution HF radar currents. Since HF radar measurements are available on an hourly-basis, so for each Doppler radial field, there was always an HF radar current field within one hour; this short time difference was ignored and the measurements were assumed to be coincident in time. The HF radar currents were filtered at a normalized uncertainty index threshold[b] of 0.8 for both u- and v-components and the Doppler radials were filtered at an Root Mean Square Error (RMSE) threshold of 0.75. The coordinate system of HF radar currents was rotated to align with the coordinate system of the Doppler radials, and one-dimensional HF radar radials extracted from this rotated dataset were used for comparison with Doppler radials.

Preliminary analysis of Doppler radials showed that they seem to have a much larger range of extreme (minimum and maximum) values than HF radar radials, so much so that they even appear unrealistic in some cases. An example of this is shown in Fig. 3.22. The primary feature of interest in the Doppler radial currents plot in Fig. 3.22a is the blue “tongue” having radial velocities in the range of ≈-100 cm/s to ≈-200 cm/s, which are quite unrealistic in this region. Even in the case of high-speed coastal jets, rarely do current magnitudes have such high values [23]. The RMSE for the Doppler currents in this region also varies over a wide range, from low to high values. HF radar radial currents in Fig. 3.22c show somewhat similar large-scale patterns, but with much lower magnitude fluctuations. Since wind models are used for removing the wind effect from the Doppler centroid measurements, it is useful to take a look at the wind

---

[b] See Sec. 1.6.2.1 for description

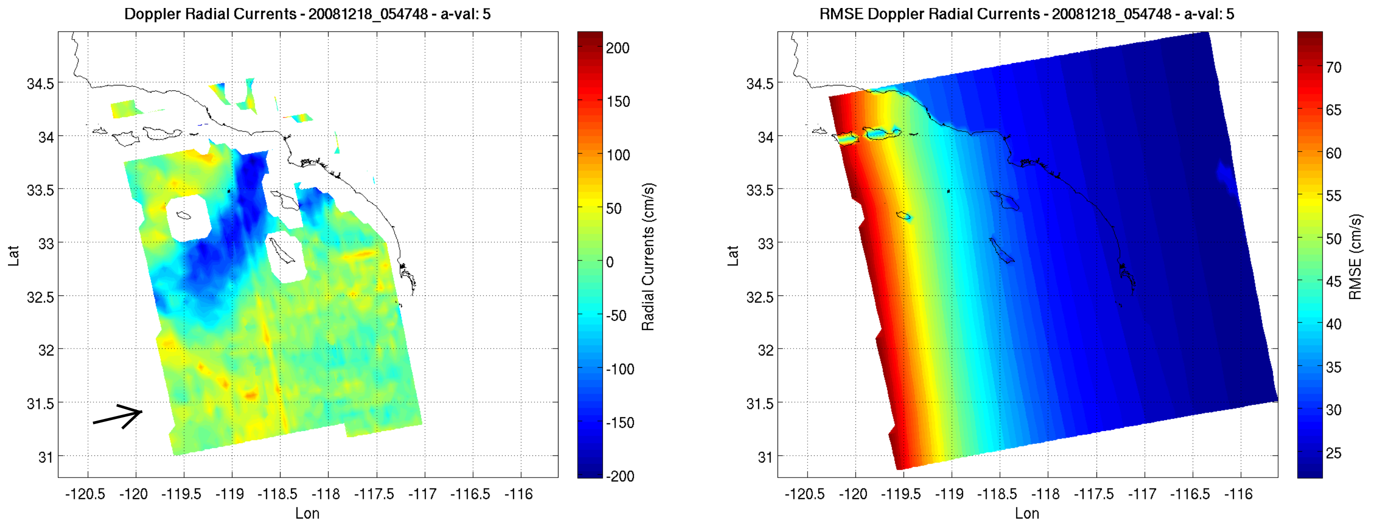

(a) Doppler radials

(b) RMSE for Doppler radial estimation

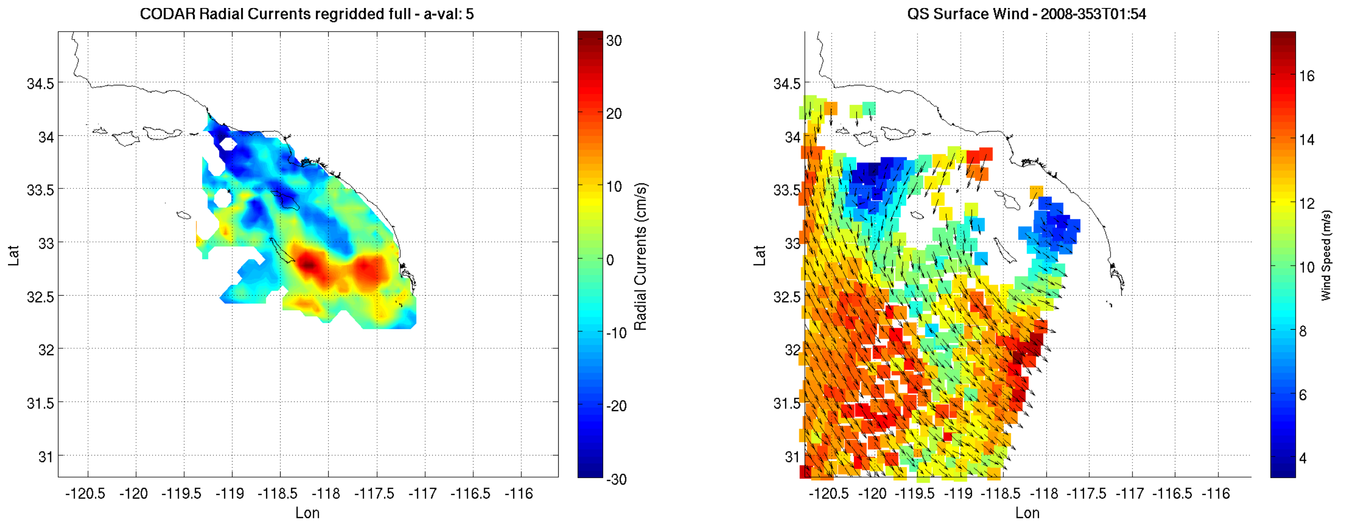

(c) High frequency (HF) radar radials

(d) QuikSCAT wind

Figure 3.22: Example of larger extreme (minimum-maximum) values of Doppler radials as compared to HF radar radials. QuikSCAT ocean surface wind measurements within ≈4 hour time difference are also shown. The black arrow in Fig. 3.22a indicates the positive radial direction of Doppler radials. See text for discussion.

field observations near the same time of the Doppler radials. QuikSCAT wind observations at 10 m height above the ocean surface are shown in Fig. 3.22d, at an observation time ≈4 hours before the Doppler and HF radar measurements (this time difference is ignored in this analysis). In the region with large negative Doppler radial velocities, the wind vectors show components in the negative radial direction, especially on the Eastern and Northern sides. In [113], it is noted that the Doppler Centroid current estimation method is quite sensitive to wind direction estimation errors, i.e. small errors in wind direction can significantly reduce the accuracy of the Doppler current radials. National Center for Environmental Prediction (NCEP) model winds, at a low grid resolution of 0.5°, were used for Doppler wind correction in processing of these Doppler datasets, which have a low spatial resolution. Furthermore, these wind corrections deal with mean fields and while they can be expected to be correct on average, they may not necessarily be correct on small scales, especially in the case of Doppler radials derived from a single Envisat WSM scene (personal communication with Morten Hansen). It is thus a strong possibility that, in the specific case shown in Fig. 3.22, the strong influence of wind has not been fully removed during the Doppler wind correction process, and this residual wind effect is a strong contributor to the very high -ve radial Doppler current velocities.

For quantitative comparisons with HF radar radials, Doppler radials were re-gridded to a constant 6 km resolution grid. After re-gridding, any grid points which were at a distance of >8 km from the original grid points were omitted from further analysis. Also, any interpolated grid points which did not have both Doppler and HF radar radials, and cases which had less than 3 coincident re-gridded vectors were omitted from further analysis. Some sample cases of re-gridded coincident Doppler and HF radar radial currents are shown in Fig. 3.23. Some large-scale features can be seen in both Doppler and HF radar radial fields, however smaller-scale features are not in great agreement. These sample plots also indicate that Doppler radials have larger extreme values (minima and maximuma) as compared to HF radar radials. This can be further seen in the histograms of re-gridded coincident Doppler and HF radar radials, in Fig. 3.24a and Fig. 3.24b, respectively; the histograms show that Doppler radials have larger extreme values, especially on the -ve side as compared to the HF radar radials.

In [56], comparison of Doppler radials with different geostrophic radials shows that Doppler radials follow similar patterns to other geostrophic currents yet have higher extreme values (minima and maxima)

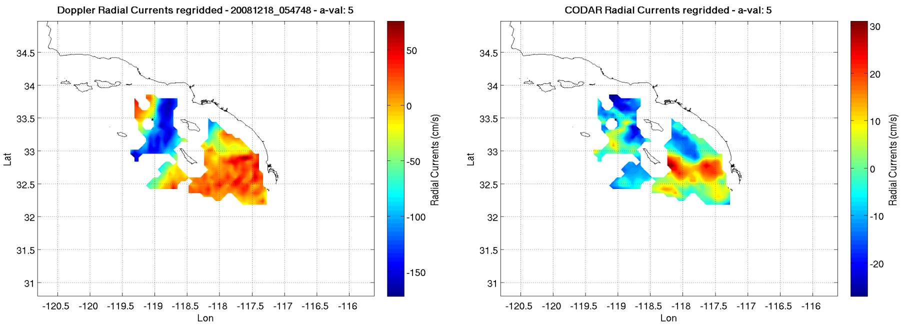

Doppler radials HF radar radials

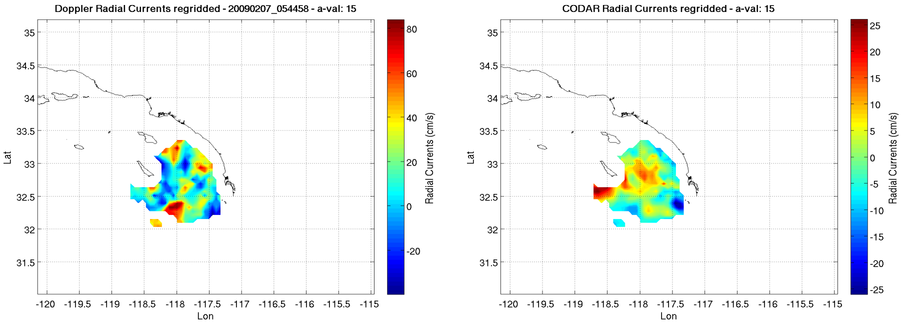

Doppler radials HF radar radials

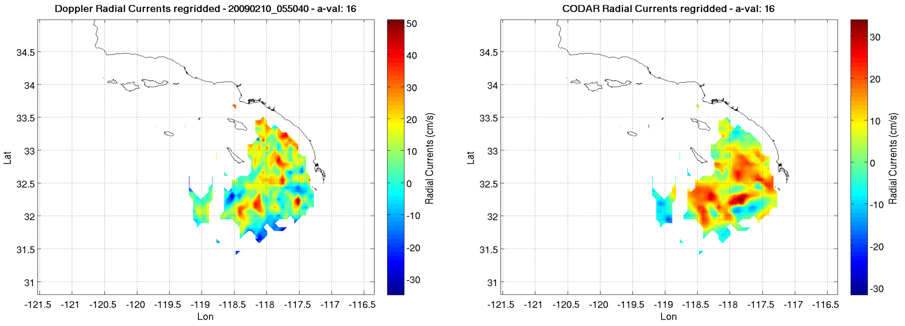

Doppler radials HF radar radials

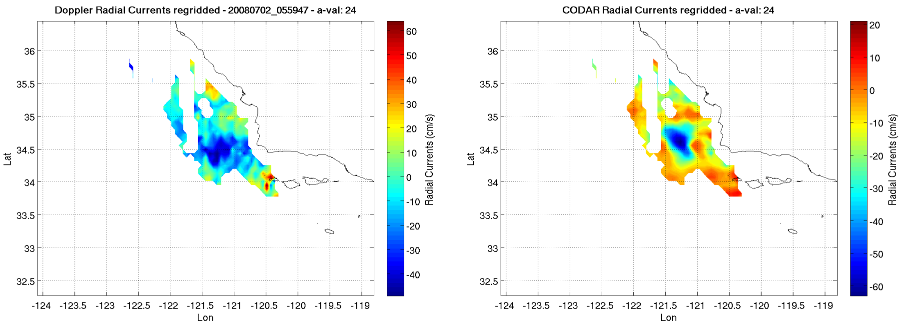

Doppler radials HF radar radials

Figure 3.23: Some sample cases of re-gridded coincident Doppler and HF radar radial currents; the plots on the left are Doppler radials while the plots on the right are HFs radar radials.

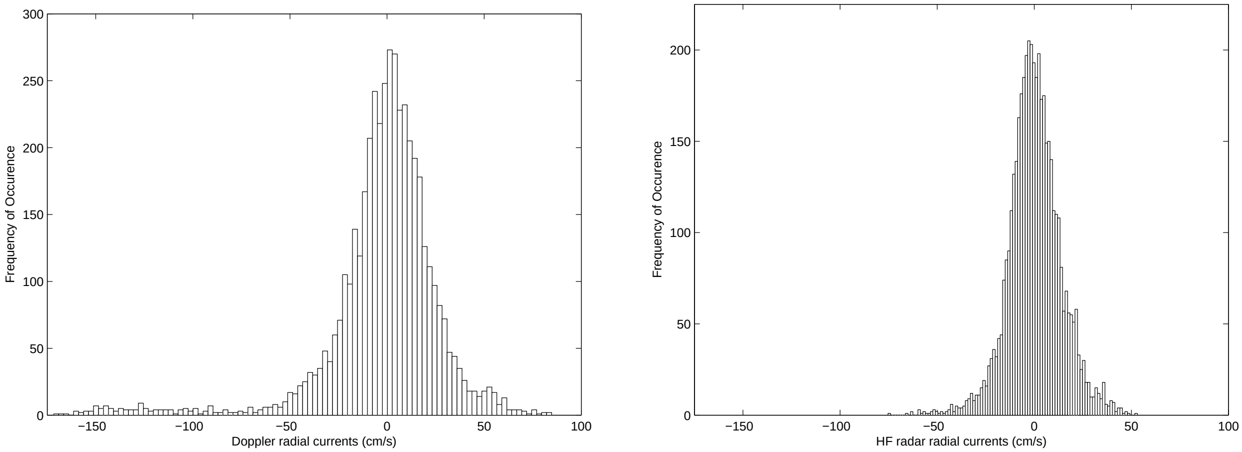

(a) Histogram of Doppler radials

(b) Histogram of HF radar radials

Figure 3.24: Histograms of re-gridded coincident Doppler and HF radar radials. Doppler radials in (a) have larger extreme values, especially on the -ve side as compared to the HF radar radials in (b).

as compared to geostrophic measurements (see Fig. 7 in [56]). In that study, the higher extreme values in Doppler radials are attributed to the contribution of ageostrophic components. In a more recent study [57], the weaker geostrophic velocities in the CNES-CLS09 data, as compared to Doppler centroid velocities, are attributed to the limited coverage of in-situ datasets and the low resolution of satellite datasets used to form CNES-CLS09 geostrophic currents. Surface drifters are known to advect out of strong current cores, thus achieving the maximum velocity only for a short while, effectively reducing the mean measured current. Geostrophic current fields derived from satellite gravity field measurements and satellite altimetry also start to get unreliable as they get closer to the coast.

High frequency radar measured currents are total surface currents measured in the coastal zone, averaged over the top 1 meter of the ocean, and contain both geostrophic and ageostrophic currents. It is therefore difficult to explain why Doppler radials have larger extreme values as compared to HF radar, yet show the same general large-scale features.From the comparison with surface wind, it seems that in certain cases, the wind fields are not completely removed during Doppler centroid correction and these wind fields contribute to the higher minimum-maximum values in Doppler radials.

3.6.1 Analysis of Residuals

Before further quantitative comparisons, Doppler radial current values >100 cm/s and <-100 cm/s were discarded (extreme value filtering). Following from the preceding discussion, the underlying assumption here is that radial current values $> |100|$ cm/s are unrealistic in this ocean region. Radial current residuals were calculated by subtracting HF radar radials from Doppler radials. The histogram of these residuals, shown in Fig. 3.25, is unimodal and symmetric about the near-zero mean. It also shows some agreement with the estimated normal histogram. The non-zero mean bias is small enough to be perhaps insignificant, however it should still be noted that MCC SAR comparisons with HF radar currents also showed a +ve mean bias for MCC SAR currents (Sec. 3.5.3).

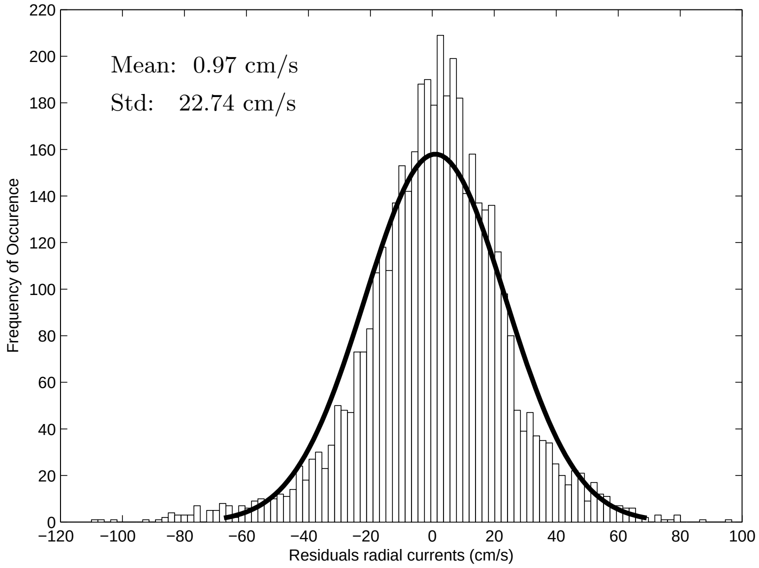

Figure 3.25: Histogram of residuals for Doppler and HF radar radial currents. The thick black line is the normal histograms estimated from the mean and variance in the residuals. The mean and standard deviation are indicated in the plot.

The accuracy of Doppler current estimation from Envisat WSM scenes increases with an increase in incidence angle [55]. Each WSM scene is composed of 5 subswaths, going from near-range to far-range, which implies that the RMSE for Doppler radial estimates decreases in general from near- to far-range. It should therefore be instructive to see the behavior of the residuals in each sub-swath. Fig. 3.26 shows the residual histograms, plotted in the same way as Fig. 3.25, but for each sub-swath, where sub-swath 1 is in near-range and sub-swath 5 is in far-range. The general trend that can be noted is that as we go from near-range to far-range, the standard deviation of the residuals decreases, and the histograms also start to approach normality (becoming more uni-modal and symmetric about the mean). The behavior of residuals for sub-swath 5 does not conform with this assumption. This is probably due to the fact that of all the WSM scenes used for derivation of Doppler radials, all except 1 were ascending orbits, and for the US West Coast, this means that the far-range will always be nearer to land. Land-contamination effects, such as azimuth ambiguities, which are known to be present in Envisat WSM scenes therefore probably play a big role in showing greater standard deviation of the residuals for sub-swath 5 than expected.

As just noted above, the RMSE for the estimation of Doppler radials is greater in the near-range and decreases towards the far-range. Ideally, the Root Mean Square Deviation (RMSD) between Doppler and HF radar radials should also follow this pattern, which would imply that both of these measurements are showing something similar. The mean Doppler radial estimation RMSE and RMS of the radial residuals are shown in Fig. 3.27, for each sub-swath. The RMSE values used are from the sub-swaths in the original Doppler radials dataset, and are filtered at a threshold of 0.75. As expected, both Doppler estimation RMSE (Fig. 3.27a) and RMSD between Doppler and HF radar radials (Fig. 3.27b) show the same general pattern, decreasing from near-range to far-range. This clearly shows that the differences between Doppler and HF radar radials have a direct relationship with the Doppler radial estimation RMSE, which again hints at the fact that both current measurement methods are sampling the same geophysical fields.

3.7 MCC SAR and Doppler Centroid Radials Analysis

Direct time-coincident comparison between Doppler radials from Envisat WSM scenes and MCC SAR currents is not possible because Envisat can not collect data in both the stripmap image mode and the WSM mode at the same time. However, it is possible to find occasions when Envisat & ERS2 SAR 30-min lag pairs were available for generation of MCC SAR currents and Envisat WSM scenes were collected in the immediately preceding or following orbit in the same location. For such specific cases, comparison can be performed between MCC SAR currents and Doppler radials separated by ≈12 hours in time. Although this is a relatively large time difference, it does eliminate the two major tidal variations, which have time

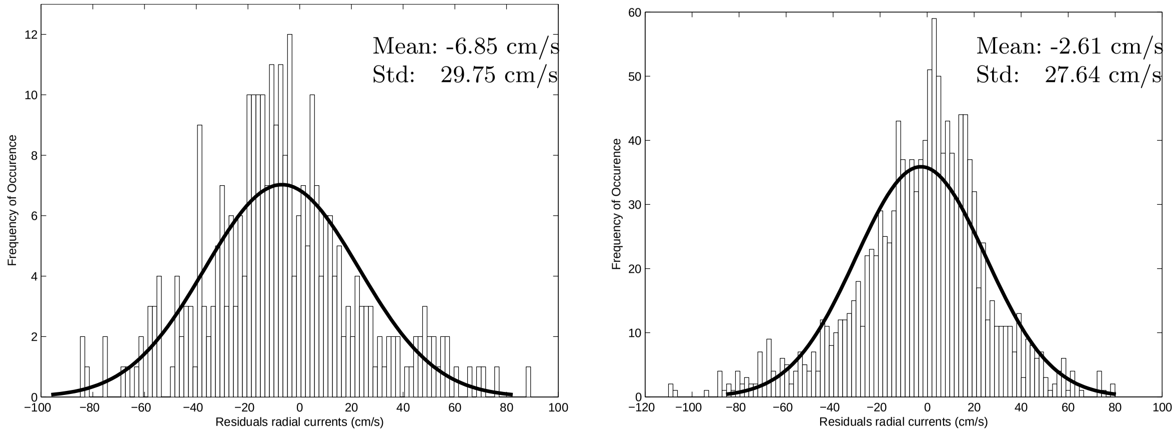

(a) Sub-swath 1 (b) Sub-swath 2

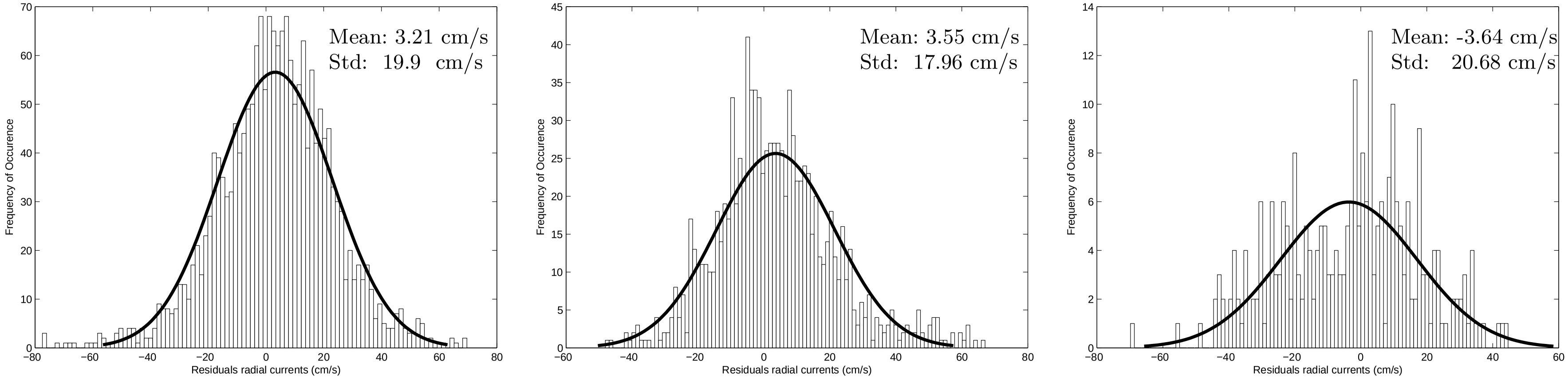

(c) Sub-swath 3 (d) Sub-swath 4 (e) Sub-swath 5

Figure 3.26: Histogram of residuals for Doppler and HF radar radial currents, calculated for sub-swaths in the Envisat WSM images. Sub-swath 1 is in the near-range while sub-swatch 5 is in the far-range. The thick black lines are the normal histograms estimated from the mean and variance in the respective residuals. The mean and standard deviation values are also indicated in the plots.

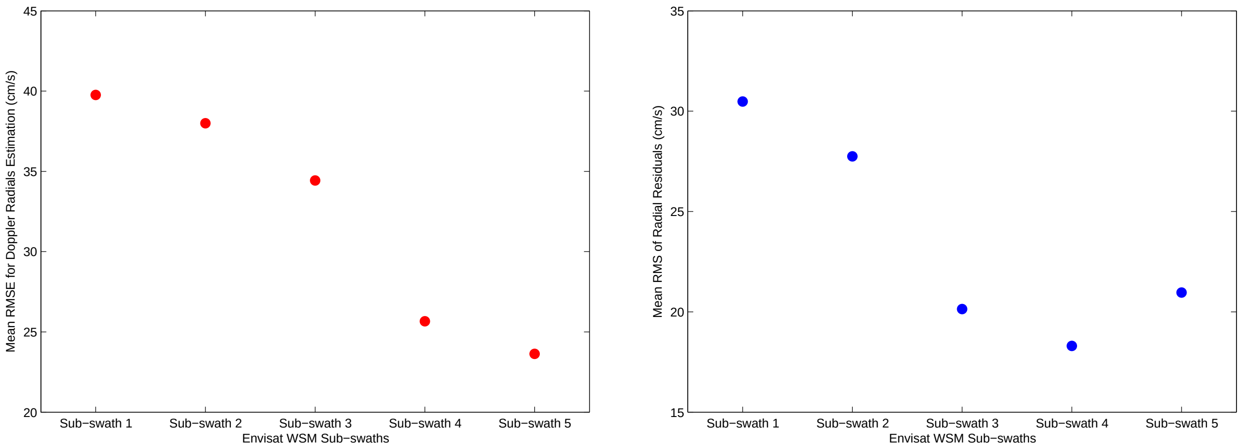

(a) Mean RMSE for Doppler radial estimates for each sub-swath

(b) Mean RMSD between Doppler and HF radar radials for each sub-swath

Figure 3.27: Doppler radial estimation RMSE (in (a)) and RMSD between Doppler and HF radar radials (in (b)) for each sub-swath in Envisat WSM scenes.

periods of 6 and 12 hours. The mesoscale features in the CCS generally have time scales larger than a day, however submesoscale features might have shorter time scales. Major reasons for short time scale variations in mesoscale current features could be eddy propagation or even eddy advection in the vicinity of an area; in general, however, these can be ignored in the CCS. A total of 5 cases were found having this ≈12 hour time difference over the CCS; they are plotted in Fig. 3.28. The Doppler radials were filtered at an RMSE threshold of 0.75. The coordinate system of MCC SAR vectors was rotated to align with the coordinate system of the Doppler radials, and one-dimensional MCC SAR radials extracted from this rotated dataset were used for the plots in Fig. 3.28. The map extent was chosen to give a good view of both Doppler and MCC SAR radials; the extent of the Doppler radial field in each case is generally larger than that shown. The plots show that the MCC SAR radials are concentrated close to the coast, while the Doppler radials are generally present farther from the coast. This can be easily explained by the fact that the MCC SAR relies on biogenic surface slicks which generally exist closer to the coast, while the Envisat WSM Doppler centroid grid suffers from land contamination near the coast due to the large Doppler centroid footprint (a few km) and also suffers from azimuth ambiguities over the coastal ocean from the brighter land targets. As a result of these issues, out of the 5 cases, only 2 (bottom 2 panels) show Doppler and MCC SAR coverage with some spatially coincident grid points. Further analysis will thus be restricted to only these 2 cases.

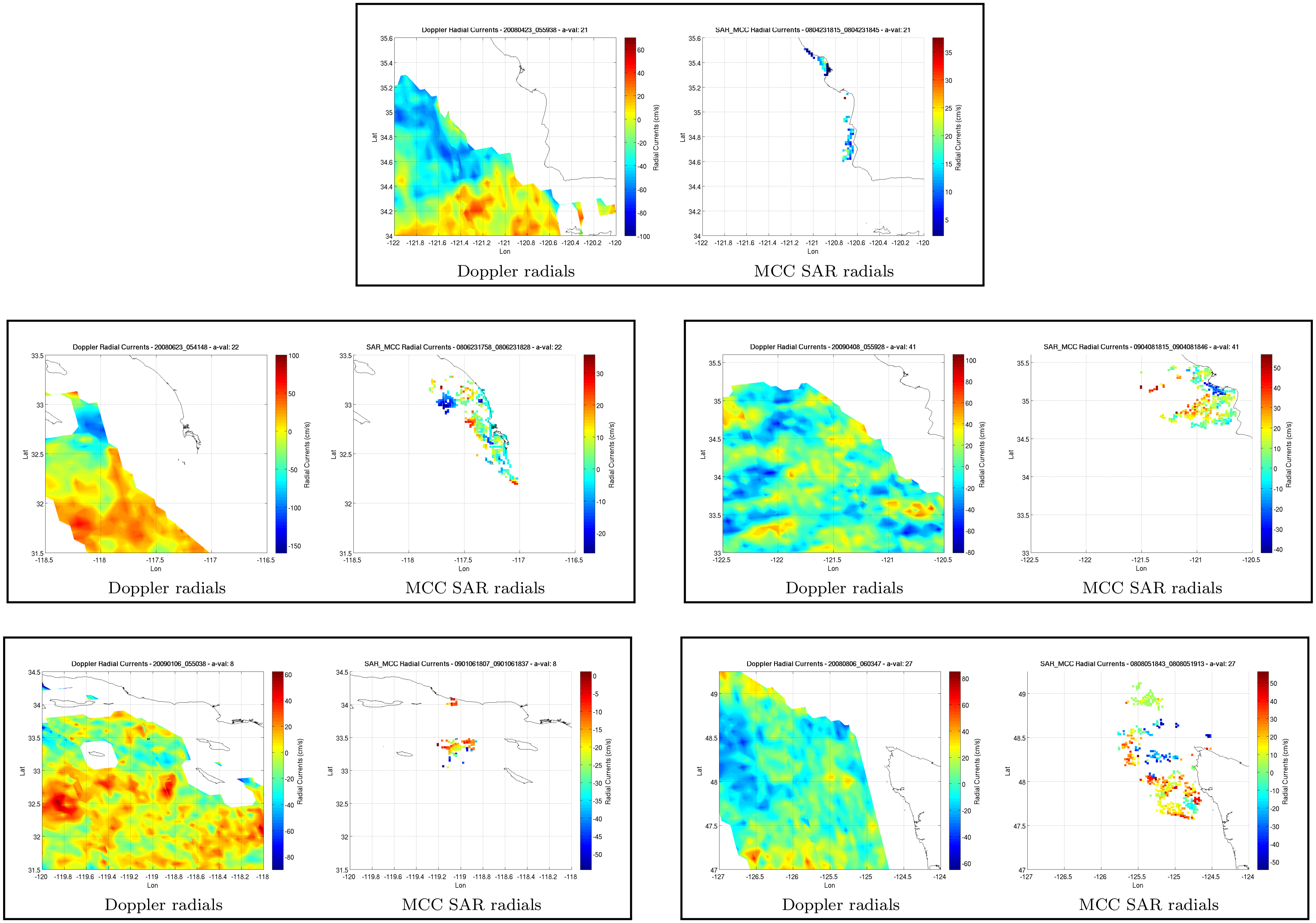

Figure 3.28: Plots of ≈12 hour time difference Doppler radials and MCC SAR radial currents. In each panel, Doppler radials are plotted on the left while MCC SAR radials are plotted on the right. Only the bottom two panels have space coincidence between the two datasets.

For a quantitative comparison, both Doppler and MCC SAR radials for the cases in the bottom 2 panels of Fig. 3.28 were re-gridded to a constant 8 km resolution grid. After re-gridding, any grid points which were at a distance of >10 km from the original grid points were omitted from further analysis. Any interpolated grid points, which did not have both Doppler and MCC SAR radar radials were also discarded. The re-gridded coincident Doppler and MCC SAR radial currents are shown in Fig. 3.29. Note that extreme value filtering has not been applied to Doppler radial fields here, as was done for comparison with HF radar radials (Sec. 3.6); this is because for the 2 re-gridded coincident cases, the radial magnitudes of Doppler radials are within |100| cm/s. In the top panel, the coincident region does not have enough areal coverage to discern any spatial patterns, and there doesn't seem to be good agreement between the Doppler and MCC SAR radials. In the bottom panel, which has better coincident areal coverage, similar spatial patterns on the large-scale can be seen. It is interesting to note that even without extreme value filtering, the minimum-maximum values of Doppler and MCC SAR radials are very similar; this was not the case when Doppler radials were compared with HF radar radials (Sec. 3.6). Although it's hard to make a definite assessment on the basis of just one good comparison of Doppler and MCC SAR radials, separated by ≈12 hours, in the bottom panel of Fig. 3.29, it seems that the extreme value magnitudes are similar for both these radial measurements because the basic measurement mechanism is same, i.e. remote sensing using C-band SAR.

3.7.1 Analysis of Residuals

Radial current residuals were calculated by subtracting MCC SAR radials from Doppler radials, for the 2 cases shown in Fig. 3.29. The histogram of these residuals is plotted in Fig. 3.30. Because of the small number of coincident points where the residuals were calculated (106 points), it would not be prudent to treat this histogram as definitive; however, the number of points analyzed is greater than 30, which lends some statistical credibility to the histogram. The mean is near-zero, the histogram has high peaks in the middle, and tapers off towards the tails. A valid assumption can be made that the histogram will tend to become more Gaussian as the number of analyzed points increases; this points towards the differences between the two datasets being dominated by random errors.

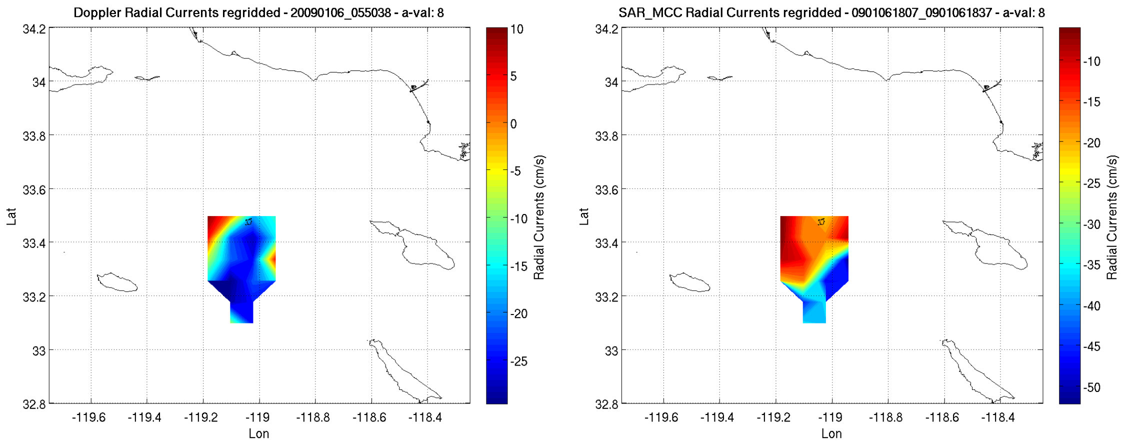

Doppler radials MCC SAR radials

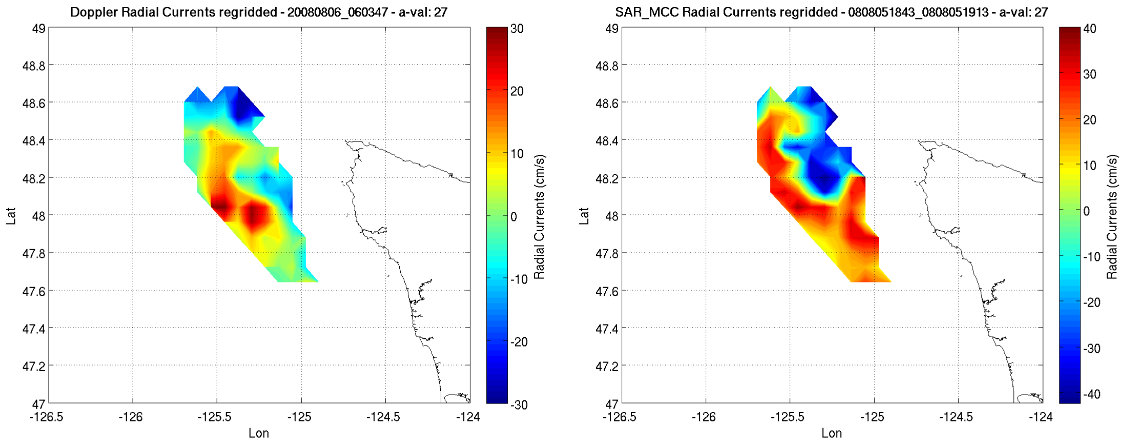

Doppler radials MCC SAR radials

Figure 3.29: Plots of re-gridded coincident Doppler and MCC SAR radials, along with their residuals, for the cases in the bottom 2 panels from Fig. 3.28. In each panel, Doppler radials are plotted on the left while MCC SAR radials are plotted on the right.

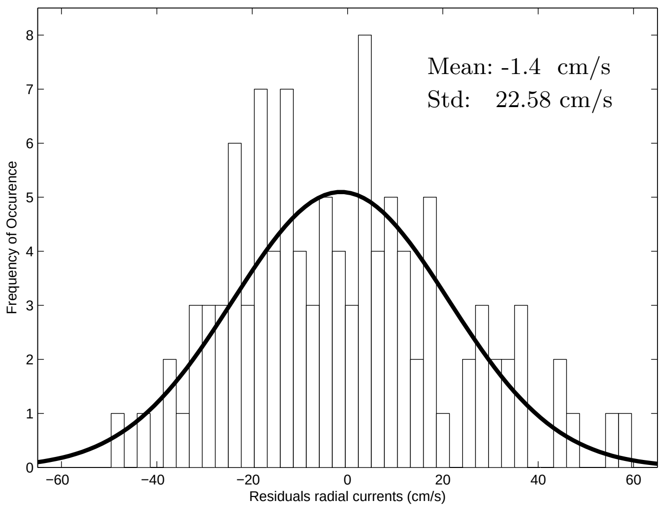

Figure 3.30: Histogram of residuals for Doppler and MCC SAR radial currents. The thick black line is the normal histograms estimated from the mean and variance in the residuals. The mean and standard deviation are indicated in the plot.

Chapter 4

Experiments with ATI for Ocean Surface Currents

4.1 Introduction

Along-Track Interferometry (ATI) is used to measure moving target velocity in the range (Cross-Track (XT)) radial direction. This chapter describes the experiments conducted for absolute phase calibration of TerraSAR-X (TSX) Dual Receive Aperture (DRA) mode ATI data. Sec. 4.2 shows why phase unwrapping is not a problem for ocean current measurement from these data acquisitions. Sec. 4.3 describes in detail the data, processing steps, and analysis of the experiments.

4.2 Phase Unwrapping Requirements for TerraSAR-X DRA Mode ATI

For TSX, the velocity at which the ATI phase wraps over 360° (v_{pw}) is a function of the DRA time lag τ_{DRA} and incidence angle θ_{inc} [112]:

$$v_{pw} = \frac{\lambda}{2\tau_{DRA} \sin\theta_{inc}} \tag{4.1}$$

where λ is the TSX radar wavelength.

The TSX phased array antenna has a length of 4.8 m, which would give a nominal DRA time lag of:

$$\tau_{DRA} = \frac{4.8}{4v_s} \tag{4.2}$$

where v_s is the TSX velocity in its orbit.

Over the range of nominal incidence angles for TSX (15° - 50°), the values of v_{pw} are plotted in Fig. 4.1. With ocean currents rarely exceeding velocities of 150 cm/s, Fig. 4.1 clearly shows that phase unwrapping is not required for ocean current measurement from TSX DRA mode ATI data.

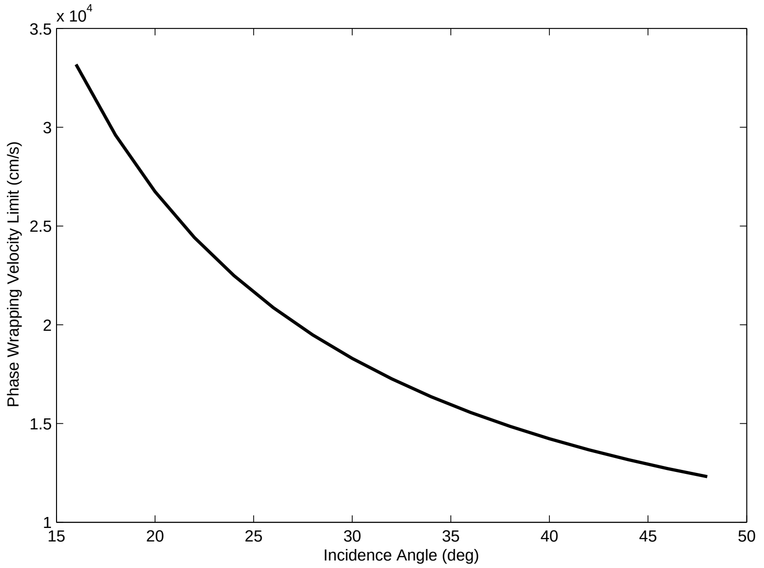

Figure 4.1: TSX DRA mode ATI phase wrapping velocity limit as a function of incidence angle, which shows that the problem of phase unwrapping can be ignored for ocean current measurement from this dataset.

4.3 Absolute Calibration for TerraSAR-X DRA Mode ATI

Absolute phase calibration is one of the primary problems for ocean surface current generation from spaceborne ATI. Although ATI through TSX on-board phased array antenna offers the advantage of a single platform with no direct XT interferometric phase contributions, the onboard receiver configurations for ATI mode operation introduce phase drift at the time of data acquisition. For the Aperture Synthesis (AS) mode ATI, channel balancing causes phase drifts between fore and aft antenna returns, which needs to be corrected. For the DRA mode, the primary reason for phase drift is inadequate antenna pattern sidelobe suppression at the time of reception when the single phased array is logically split into two antennas length-wise. One method commonly used for absolute phase calibration is to use phase measurements over land and determine a corrective phase trend such that the phase over stationary land should be zero. This method for absolute phase calibration was used for TSX AS mode ATI data in [111] and [124]. Other experimental methods for phase calibration use azimuth displacement of range-moving targets, e.g. in [2], a ship was used, whose velocity was determined by the well-known wake-displacement method [96].

The phase trends in TSX AS mode ATI data can be eliminated by eliminating the channel balancing step during Synthetic Aperture Radar (SAR) processing [123]. For DRA mode data, however, the phase trend in Along-Track (AT) phase is not clearly known. This restricts the use of TSX DRA mode ATI to only scenes where land is available, which can be used to model and remove phase trends.

Some TerraSAR-X DRA datasets were processed for absolute phase calibration experiments. The DRA mode datasets are delivered as complex returns from both fore and aft virtual antennas, and also the full antenna return, in slant-range and azimuth coordinates. Eight images were chosen, with adequate number of land and ocean pixels in each scene. The full-antenna return intensity images are shown in Fig. 4.2, along with their geographical location. Due to their huge file sizes, the complex images were down-sampled by a factor of 2 for easier data handling in subsequent processing. The interferogram was generated by complex product of the fore- and aft- antenna returns, and interferometric phase over land and ocean regions was extracted. Due to high phase noise, the interferogram was resampled to slant range and azimuth grid cells of 100 m x 100 m resolution. It has been shown previously [124] that the phase trend in TSX ATI images can be modeled over land by a 2nd degree polynomial fit. This is explored in further detail below.

For the extracted interferometric phases over land, a 2nd degree polynomial fit was calculated for each line of constant range. The complex images are processed at full bandwidth and are not subjected to any spectral weighting during SAR image formation; this causes some SAR imaging artifacts like ghosting (azimuth ambiguities) of bright land targets over the low-backscatter ocean. To eliminate such artifacts and other spurious values in each range line, any phase values that were statistical outliers (outside the 1.5 standard deviation range of each range line phase) were discarded. Range lines with less than 2% land pixels in them were also discarded. A 2nd degree polynomial fit was calculated over each range line, and these were averaged to generate one mean fit. The mean fit over land for each ATI interferogram is shown in Fig. 4.3 along with the mean filtered phase values. In most cases, a 2nd degree polynomial seems adequate to define the overall phase trend.

Over the ocean, the non-zero phase trend over land becomes a component of the total ocean interferometric phase in each range line. It is not known whether or not this phase trend can be extracted from only ocean interferometric phase. To analyze this, the processing done for land interferometric phase above was repeated for each ocean range line. For each of the 8 chosen ATI datasets, the phase trends extracted by polynomial fitting over land and ocean are plotted together in Fig. 4.4. Overall, the phase trend over ocean

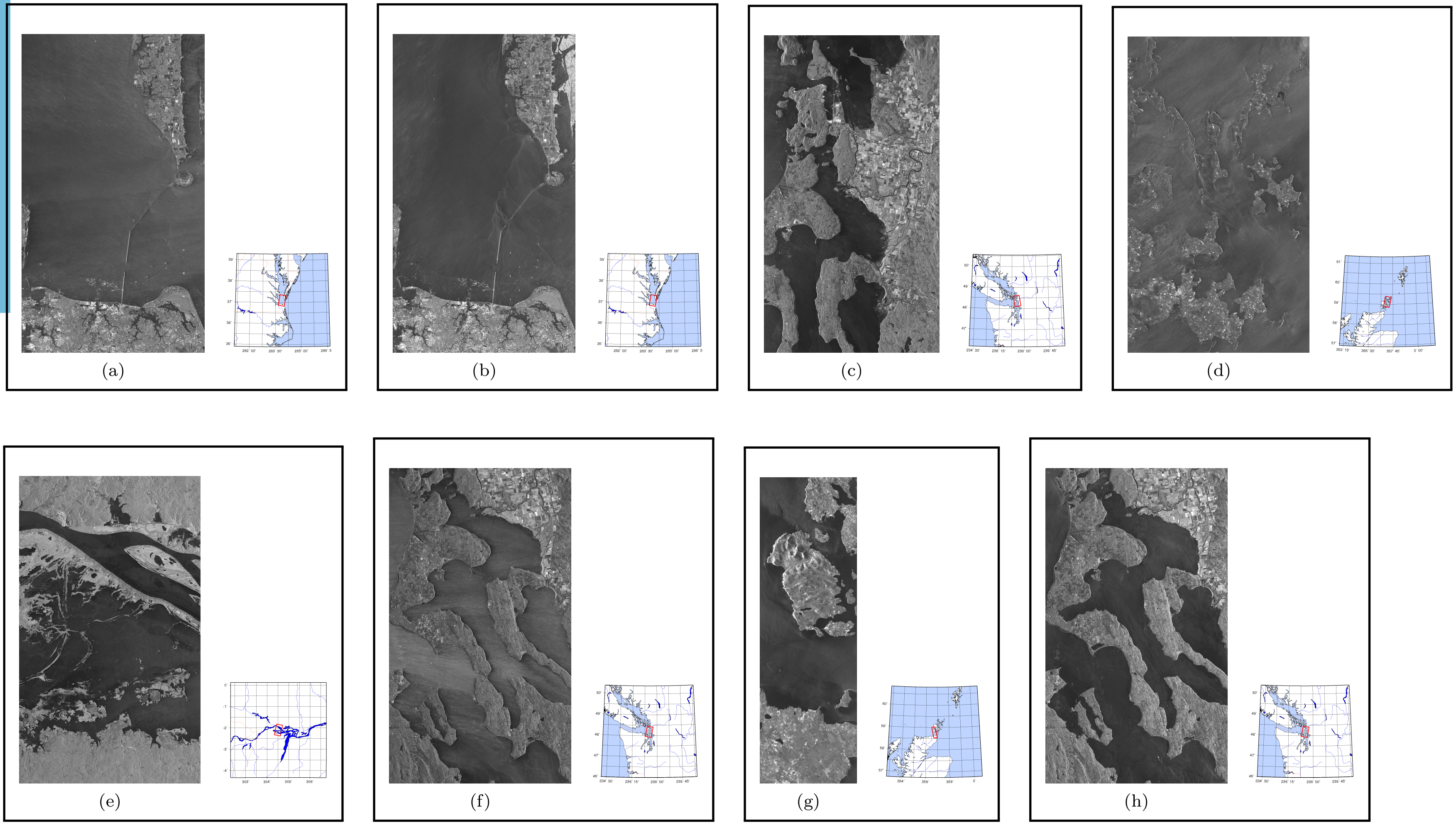
(a) (b) (c) (d) (e) (f) (g) (h)

Figure 4.2: TerraSAR-X DRA mode ATI datasets chosen for absolute calibration experiments. The images shown are preview (heavily down-sampled) versions of the full antenna return intensity images. The geographical location of each image is shown in the accompanying inset map. Data courtesy DLR.

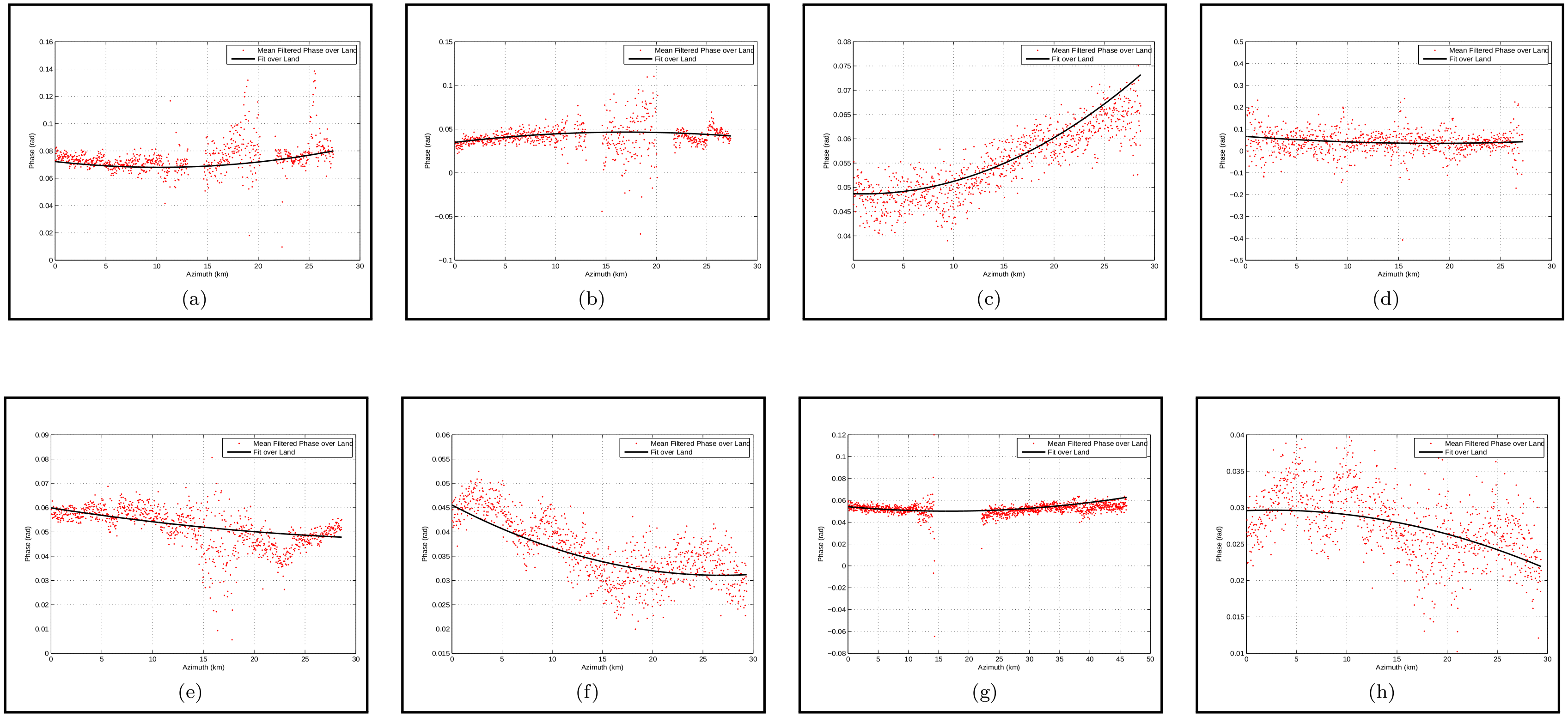

(a) (b) (c) (d)

(e) (f) (g) (h)

Figure 4.3: TerraSAR-X DRA mode ATI mean filtered phase values (red dots) along with the 2nd degree polynomial fit that defines the phase trend (black lines).

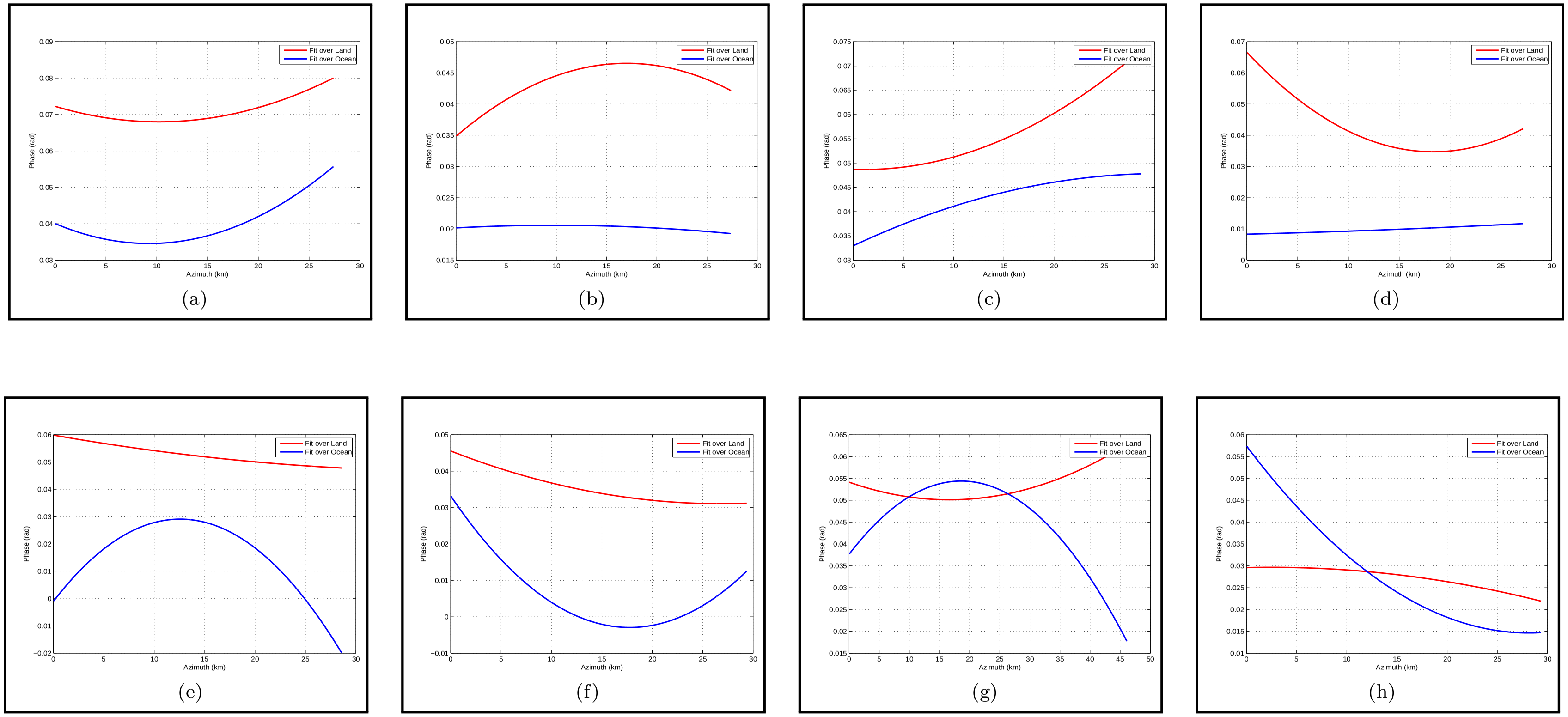

(a) (b) (c) (d)

(e) (f) (g) (h)

Figure 4.4: TerraSAR-X DRA mode ATI 2nd degree polynomial fits for phase trends, over land (red lines) and over ocean (blue lines).

has smaller values than the trend over land. In some cases (Fig. 4.4a, 4.4b, 4.4c, 4.4f) the ocean phase trend shows reasonable agreement in terms of the trend shape, which may hint towards an empirical additive or multiplicative constant factor that defines the relationship between the land and ocean phase trends. At the same time, there are cases which show no agreement at all (Fig. 4.4d, 4.4e, 4.4g, 4.4h). No definite judgment can be made from the plots in Fig. 4.4.

Another way to analyze the phase trends is to consider the frequency components present in each range line, i.e. the wavenumber power spectra of the range lines. Shown in Fig. 4.5 are the mean power spectra for each ATI phase, over land and ocean (solid red and blue lines, respectively); these spectra are the mean of individual spectra determined over each range line. For stationary land, the primary phase values are due to the low-wavenumber phase trend, which is why the mean spectra for ocean and land are nearly the same at low wavenumbers, in all ATI datasets. At higher wavenumbers, the spectra show markedly decreased values for phase over land, which shows that phase over land does not contain much high wavenumber components. Fig. 4.5 also contains plots of the power spectra of the 2nd degree polynomial fits calculated over land and ocean (dashed red and blue lines, respectively). Since the fits are just a 2nd-degree polynomial function, with no added noise or other frequency components, the spectra present the standard view of a long-period function. The fits over land contain more power in general, which should be expected from what was observed in Fig. 4.4. Also note that for the cases in Fig. 4.4 where the trend shapes are not in good agreement, the spectra in Fig. 4.5 are also not the same shape in the lower wavenumbers. Overall, the plots for all cases in Fig. 4.4 and 4.5 show that, in limited cases, the phase trend can be estimated from ocean phase, with the trend magnitude scaled relative to the phase trend over land by an unknown factor.

Absolute phase calibration is generally performed by removing the 2nd degree polynomial fit phase trend over land from the ocean interferometric phase. Here, absolute calibration is performed alternately by removing both the fit over land and the fit over ocean; the mean power spectra for ocean phase (solid blue lines), ocean phase calibrated by fit over land (dashed red lines), and ocean phase calibrated by fit over ocean (dashed blue lines), are all shown together in Fig. 4.6. For absolute calibration using either trend estimated over land or ocean, the resultant spectra are only affected in the lower wavenumbers. The spectral power distribution, however, is different for absolute calibration using land and ocean. This is not unexpected,

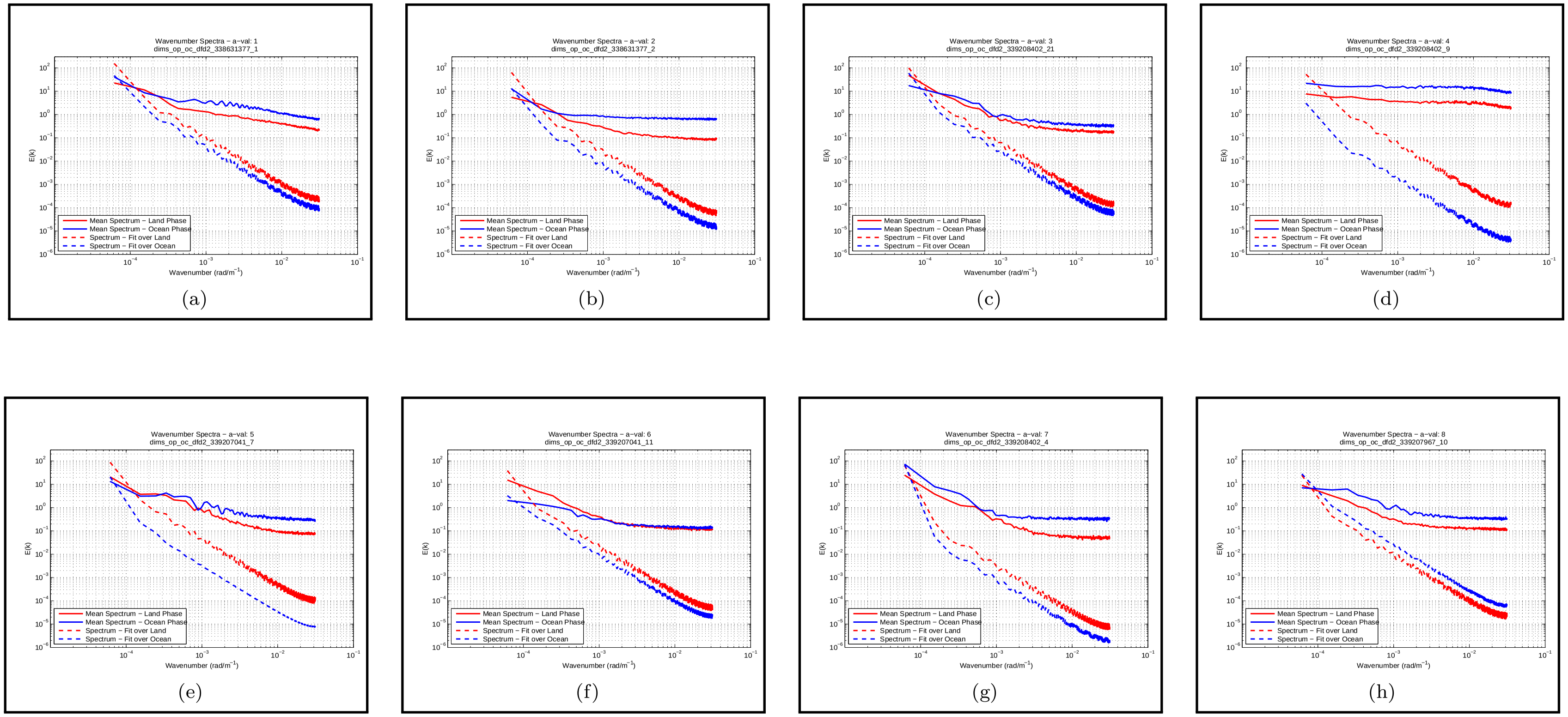

Figure 4.5: Mean power spectra for ATI phases over land and ocean (solid red and solid blue lines, respectively), and power spectra for 2nd-degree polynomial fits over land and ocean (dashed red and dashed blue lines, respectively).

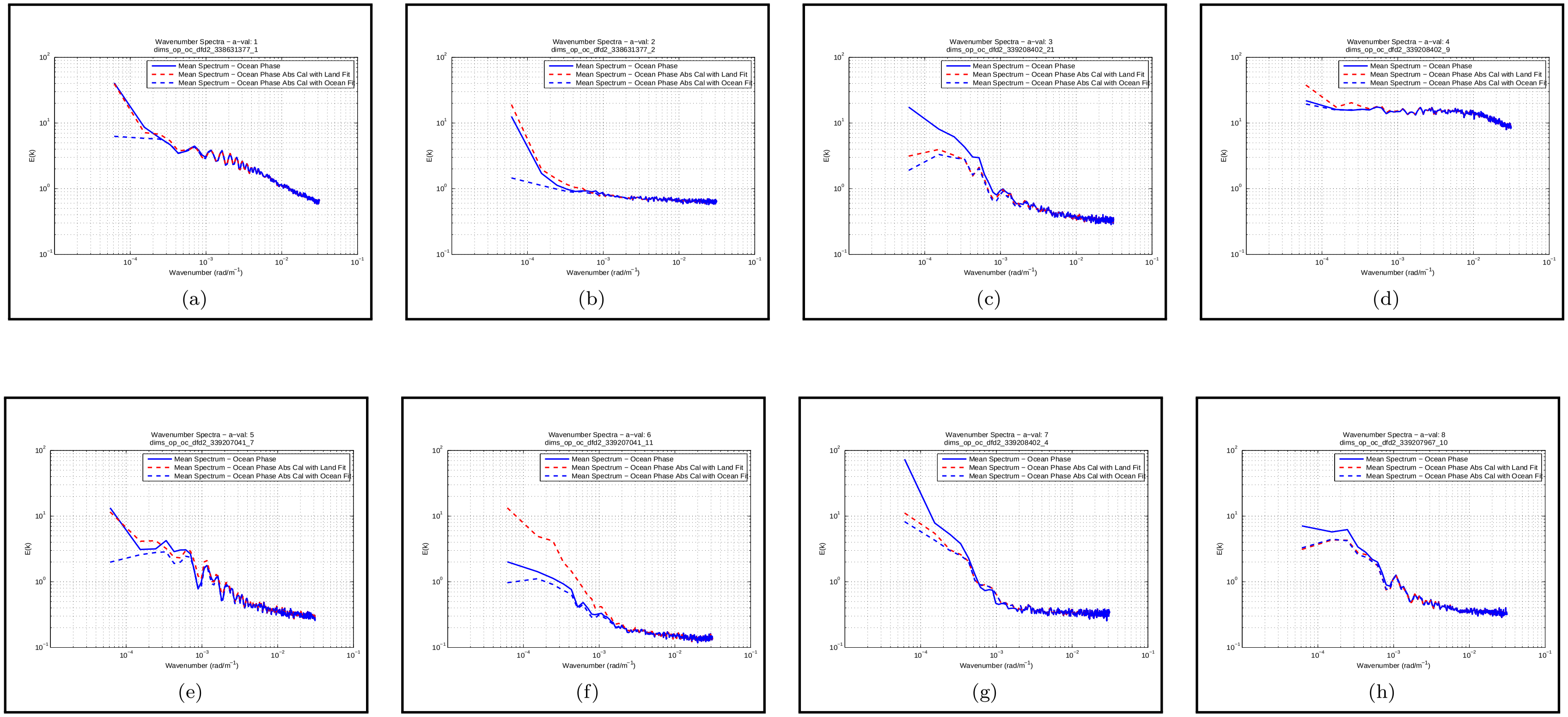

(a) (b) (c) (d)

(e) (f) (g) (h)

Figure 4.6: Mean power spectra for ATI phases over ocean (solid blues lines), and mean power spectra for absolute calibrated ocean phases, using trends estimated over land (dashed red lines) and trends estimated over ocean (dashed blue lines).

as the phase trends estimated over ocean would definitely include some actual longer period components in the ocean phases as phase trend, while the phase trend estimated over land should ideally show only the actual phase trend. In all cases, absolute calibration using trend estimated over ocean suppresses the lower wavenumbers by a much higher factor relative to the phase trend over land. Of even more interest is the fact that in 2 cases (Fig. 4.6c and 4.6h), the absolute calibrated spectra are nearly the same. This encouraging result points towards a probable solution for absolute calibration using phase trends estimated over only ocean, in limited cases.

In light of the above observations, a more direct view of absolute calibration using estimated phase trends is shown in Fig. 4.7, which contains plots for case (c) from the figures above (e.g. Fig. 4.2). The left panel shows the uncalibrated interferometric phase, the middle panel shows the interferometric phase calibrated using phase trend estimated over land, and the right panel shows the interferometric phase calibrated using phase trend estimated over ocean. All phase plots are smoothed by a 5x5 low-pass mean filter, used thrice in succession. The white box in all images indicates a strong azimuth ambiguity (confirmed through manual inspection of the interferogram) and land) and has been eliminated empirically. All phase plots are overlaid on the full-antenna return intensity image to show land and ocean areas. Both calibrated plots have the same general spatial distribution of phase, however what is more significant is that their color scales are very similar to each other, as compared to the color scale for the uncalibrated phase.

To summarize the whole discussion above, the usage of only ocean to estimate the phase trend for absolute calibration of TSX DRA mode ATI datasets looks quite promising and deserves further detailed study.

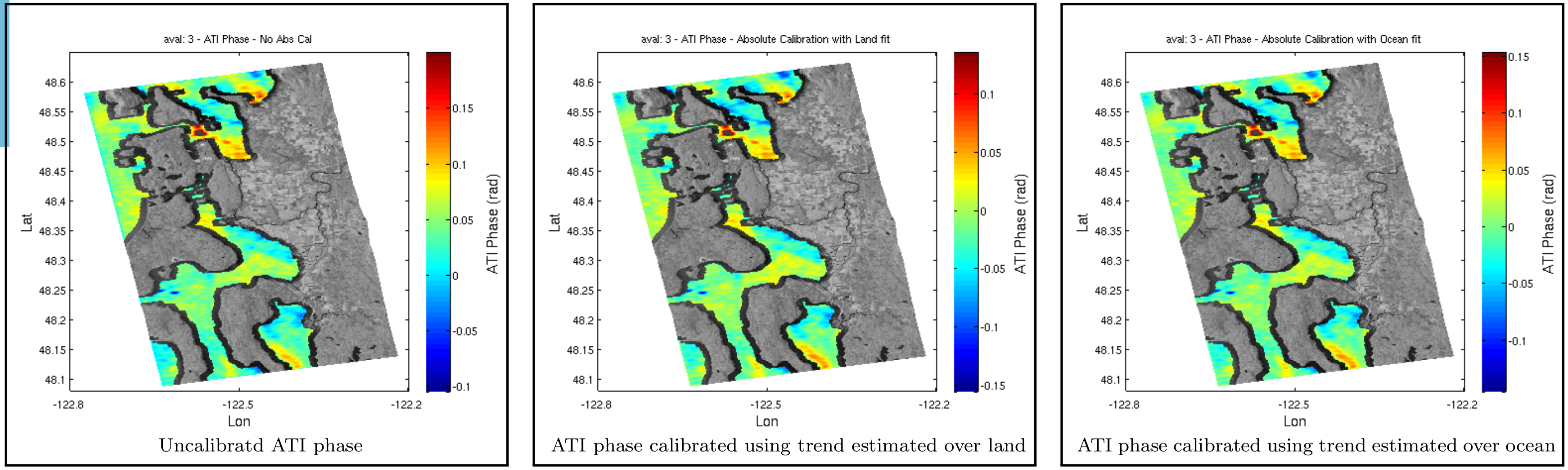

Uncalibratd ATI phase

ATI phase calibrated using trend estimated over land

ATI phase calibrated using trend estimated over ocean

Figure 4.7: Absolute ATI phase calibration from land and ocean trends for case (c) in Fig. 4.2. The left panel shows the uncalibrated phase, the middle panel shows the phase calibrated using phase trend estimated over land, and the right panel shows the phase calibrated using phase trend estimated over ocean. All phase plots have been smoothed using a 5x5 mean filter three times successively. The plots are overlaid on the full-antenna return intensity image (in gray-scale).

Chapter 5

Discussion

5.1 Low Backscatter Features in SAR

As discussed in Sec. 2.4.2.3, besides biogenic slicks, low-backscatter signatures in Synthetic Aperture Radar (SAR) intensity images over the ocean may also occur due to low winds, rain, wave-current interactions, conditions in the marine atmospheric boundary layer, and oil slicks. These sources of low-backscatter are generally ignored in the processing of sequential SAR imagery of 30-min lag by virtue of the defined Maximum Cross-Correlation (MCC) processing parameters (pattern subwindow and search window sizes), which focus on estimating surface slick advection. For example, one such feature was present in the MCC SAR data processing example shown in Fig. 3.9, and the accompanying discussion in Sec. 3.3.5 explained how the MCC SAR processing ignores low-backscatter features which are not surface slicks. However, the MCC SAR processing does not explicitly employ any other mechanism to distinguish between low-backscatter features from different phenomena. An implementation of such a mechanism in the data processing chain could be a future improvement in the method to make it more robust in terms of making sure that the low-backscatter features being detected and tracked are surface slicks.

5.2 MCC SAR and HF Radar Analysis

While High frequency radar currents serve as a good reference dataset for MCC SAR currents due to their coincident coverage at comparable resolution, the direct comparisons done in Sec. 3.5 should be accompanied by a note of caution. While C-band SAR penetrates, at most, only a few cm into the ocean surface, the High frequency (HF) radar currents being used are measured and averaged over the top 1 m of the ocean surface [72]. In fact, this could be the reason why MCC SAR currents show greater magnitudes than HF radar currents in general. Under ideal steady-state wind near the ocean surface, the Ekman spiral is set up in the first few meters depth in the ocean: the current vectors change direction and experience a reduction in magnitude with depth.This would imply that the magnitude of the 1 m averaged HF radar average currents will be less than MCC SAR currents measured at the surface. Gade et al. [47] reported the same higher magnitude in currents derived from SAR feature tracking when they compared their derived currents with model currents averaged over the top 4 m of the ocean, and they too attributed it to the effect of surface wind. While this is only a hypothesis and a probable explanation for the higher magnitude of currents in MCC SAR, this needs to be explored further by analyzing surface wind fields along with the SAR images. The hypothesis is that higher velocity winds would set up a stronger vertical shear in the Ekman layer and should show more deviations between MCC SAR and HF radar current measurements. A correlation between wind speed and disagreement between the two current fields would be one affirmation of this hypothesis.

In Sec. 3.5.3, the near-zero bias for the cross-shore component and a significant mean bias for the along-shore component in the residuals between MCC SAR and HF radar currents was attributed to the HF radar measurement mechanism. However, another additional aspect to this consideration is that the mean California Current System (CCS) current is primarily along-shore and there is a mean flow contribution to these currents which may be better captured in one medium rather than another.

5.3 Impact of Stokes Drift

The orbital motion executed by a parcel of water due to a passing wave is not a closed orbital path; for a short (deep-water) wave, this orbit is circular, while for a long (shallow-water) wave, the orbit is elliptical [101]. The water parcel has a slightly larger velocity at the top of its orbit as compared to the backward velocity at the bottom of its orbital motion. This effectively generates a current that modifies the phase speed of the wave relative to a stationary observer and results in a net forward motion in the direction of surface wave propagation; this net transport is called "Stokes drift" and it occurs for both short and long waves. Stokes drift is important at the surface and decays rapidly with depth [8]. It can be also interpreted as the difference between Lagrangian and Eulerian velocities in the presence of surface gravity waves [51, 118]. Stokes drift may also result due to swell (surface gravity waves not generated by the local wind). Recent theory suggests that, in the open ocean, the surface Stokes drift typically is 2/3 of the total surface wind-induced drift [8], and for fully developed seas with no fetch, the surface Stokes drift has a magnitude that is $\approx$1.62% of the wind speed at 10 m above the sea surface [135].

5.3.1 Stokes Drift in HF Radar and MCC SAR Current Measurements

The hourly-averaged surface current measurements by HF radar should also contain the effect of Stokes drift, but the measured impact of this drift would depend on the waves resonant to the radar frequency [7,38]. In fact, HF radar currents contain a nonlinear wave correction that is essentially a filtered surface Stokes drift, which is a function of the radar frequency [8]. High frequency radar frequency also determines the depth over which these measurements are averaged (higher frequency would generally measure over a shallower surface layer). Calculating the exact Stokes drift component in HF radar current measurements is not a trivial task; see [8] for an example of Stokes drift estimation using a numerical wave model.

The contribution of Stokes drift is present in surface slick advection tracked in 30-min separation SAR image pairs, which is essentially a Lagrangian measurement. Furthermore, slick formation dampens the wind-driven surface capillary waves, and therefore the wind-induced current over a slick-covered ocean surface is smaller than that over a slick-free surface [139]. The contribution of Stokes drift to total surfactant transport is not well-known and is a topic of present research (e.g. [8], McWilliams, J. C. and Fox-Kemper, B., Oceanic wave-balanced surface fronts and filaments, submitted to J. Fluid Mech., 2012).

The MCC SAR currents and HF radar currents thus definitely contain different Stokes drift contributions in their total measured currents, due to difference in their measurement methods. Determining and analyzing these Stokes drift contributions for the two methods may be a topic for further research. However, a rough calculation of the general Stokes drift magnitudes will be useful towards finding physical explanations for the differences between MCC SAR and HF radar measurements.

Under the simplifying assumptions of uni-directional waves and the wave spectrum being separable into direction and frequency components, Webb & Fox-Kemper [135] propose a relatively simple method to calculate the surface Stokes drift magnitude:

$$U^s = \frac{16\pi^3}{g}\int_0^\infty f_w^3 \; S\left(f_w\right) \; df_w = \frac{16\pi^3 m_3}{g} \tag{5.1}$$

$$m_3 = \int_0^\infty f_w^3 \; S\left(f_w\right) \; df_w \tag{5.2}$$

where U^s is the surface Stokes drift magnitude, g is the acceleration due to gravity, f_w is the wave frequency, $S\left(f_w\right)$ is the wave spectrum, and m_3 is the third wave spectral moment.

The wave spectrum $S\left(f_w\right)$ can either be generated from models or estimated through empirical forms. Here, the well-known Pierson & Moskowitz (PM) wave spectrum for fully developed seas [98] is used, given in its empirical form by:

$$S\left(f_w\right) = S\left(f_w, PM\right) = \frac{g^2\alpha_{PM}}{(2\pi)^4 f_w^5}\exp\left[-\frac{5}{4}\left(\frac{f_{wp}}{f_w}\right)^4\right] \tag{5.3}$$

where α_{PM} is an empirical factor, and f_{wp} is the peak wave frequency for the spectrum.

For fully-developed waves, a typical value for α_{PM} is:

$$\alpha_{PM} = 8.1 \times 10^{-3} \tag{5.4}$$

and the peak frequency f_{wp} can be expressed in an empirical form as a function of wind speed at 19.5 m above the ocean surface ($W_{19.5}$) [135]:

$$f_{wp} = \frac{1.14g}{2\pi W_{19.5}} \tag{5.5}$$

Generally, wind observations over the sea surface are available at a height of 10 m. Under the assumption of a neutrally stable atmospheric boundary layer and a drag coefficient of 1.3×10^{-3}, the relationship between wind speed at 10 m above the ocean surface (W_{10}) and wind speed at 19.5 m above the ocean surface ($W_{19.5}$) can be approximated as [120]:

$$W_{19.5} \approx 1.026 W_{10} \tag{5.6}$$

Using Eqns. 5.3 - 5.6, Eqn. 5.1 becomes:

$$U^s \approx \frac{g\alpha_{PM}}{\pi}\int_0^\infty \frac{1}{f_w^2}\exp\left[-1.8976\left(\frac{g}{2\pi f_w W_{10}}\right)^4\right] \; df_w \tag{5.7}$$

QuikSCAT wind observations at 10 m height above the ocean surface are available in the near-shore regions at a resolution of 12.5 km during most of the time period over which MCC SAR currents are generated (2008-2009). These wind velocity magnitudes were used to derive the approximate surface Stokes drift magnitude from Eqn. 5.7; only wind observations within ±6 hours of the MCC SAR current fields were used, under the assumption that no significant changes in the wind field will occur within a time-frame of 6 hours. These wind fields were re-gridded to 6 km resolution for consistency with the 6 km HF radar currents dataset. The histogram of these re-gridded coincident W_{10} magnitudes over all processed MCC SAR datasets is shown in Fig. 5.1a, while the histogram of the derived Stokes drift magnitudes is shown in Fig. 5.1b. The histograms are the same in shape because the surface Stokes drift and W_{10} magnitudes have a nearly linear relationship with each other [135]; both histograms are shown here to illustrate the U^s and W_{10} magnitudes. The surface Stokes drift magnitudes are mostly in the range of 4-5 cm/s, which is ≈0.4 of the magnitude bias between MCC SAR and HF radar currents (≈11 cm/s). However, the numbers are in the comparable range, and it seems very likely that surface Stokes drift can explain some of the magnitude bias, while there may be other contributions to the magnitude bias. Furthermore, many simplifying assumptions have been made for the Stokes drift estimation here. The PM spectrum is for fully developed waves in the open ocean, while

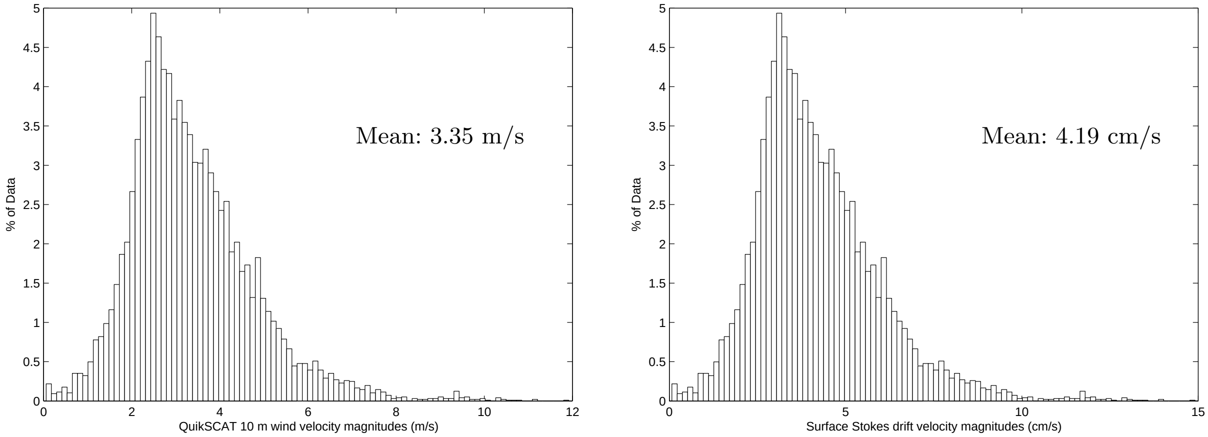

(a) Histogram of QuikSCAT re-gridded coincident 10 m surface wind magnitudes

(b) Histogram of estimated surface Stokes drift magnitudes

Figure 5.1: Histograms of QuikSCAT 10 m surface wind magnitudes (in (a)) and surface Stokes drift magnitudes estimated from the PM spectrum (in (b)). The histograms have the same form because the relationship between 10 m surface wind and surface Stokes drift magnitudes is nearly linear.

the area of interest for this research is the coastal ocean. Also, fetch (the distance over which the wind blows over the ocean with constant velocity) has not been considered; a finite fetch represents continuous wave development through non-linear, wave-wave interactions (even for very long times and distances), unlike the static “fully-developed” spectrum of Pierson & Moskowitz [120]. The JONSWAP (Joint North Sea Wave Observation Project) spectrum [58] is a modification to the PM spectrum and incorporates fetch. For the US West Coast, however, fetch is not a very important consideration and can be ignored, as surface winds here are generally aligned along-coast most of the time [23]. The directional spread loss for Stokes drift, which is the loss associated with wave energy in other directions than the uni-directional wave assumed here, has not been considered either [135]. Finally, to explicitly determine the impact of Stokes drift to the comparison of MCC SAR and HF radar currents, the depth profile of Stokes drift for HF radar measurements has to be determined. However, this initial estimation confirms that Stokes drift plays a significant role in such comparisons.

5.3.2 Stokes Drift in Doppler Centroid Current Measurements

The Stokes drift may also be important when comparisons between Doppler Centroid and HF radials are made, because of different resonant wavelengths for the HF radar and Envisat ASAR frequencies. But perhaps the Stokes drift contribution is not that important due to the comparison being made for the low spatial resolution grid of 8 km. In the processing for Doppler radials, the Stokes drift should effectively be removed with the wind removal, however the wind removal employs a model wind field as input to an empirical model, which could have its own errors. These wind fields are correct on average, but may not be correct for specific cases.

Chapter 6

Conclusions and Future Work

6.1 Conclusions

In this dissertation, Envisat Advanced SAR (ASAR) & ERS-2 Advanced Microwave Instrument (AMI) C-band SAR stripmap intensity images acquired with a time lag of 30 minutes are used to derive MCC SAR ocean surface currents at ≈1.9 km spatial resolution. Surface currents are measured by utilizing the backscatter damping by biogenic surface slicks, and the advection of these surface slicks is measured for determination of current fields. A semi-automated algorithm is developed for this purpose, using the Maximum Cross-Correlation (MCC) method, which has been previously used to track features in thermal infrared (TIR) and ocean color (OC) images. All the processing steps are described and explained in detail. The chosen primary geographical area of study is the coastal California Current System (CCS), where submesoscale and mesoscale current features' time and length scales allow for suitable measurement through a 30 minute time interval. The CCS is well-known for biogenic slicks, either through upwelling, or in convergence zones of submesoscale eddies with diameters <10 km. Nearly two years of data over 2008-2009 (a total of 124 image pairs) is processed. Some data is also processed over the US East Coast as an experiment to see if the MCC SAR method may generate currents in regions other than the CCS. However, detailed data analysis and validation is restricted to the MCC SAR currents generated in the CCS.

The wavenumber spectrum of ocean currents gives an insight into the Kinetic Energy (KE) distribution in the ocean over a range of spatial scales. Substantial velocity variance in the CCS is known to reside in the submesoscale range. In the submesoscale wavenumber regime, theory predicts a power-law decay behavior;

current traditional quasigeostrophic (QG) theory specifies a power-law slope of -3, surface quasigeostrophic theory (SQG) and 3D isotropic turbulence theory predicts a power-law slope of -5/3, and high-resolution simulations and frontogenesis theory predicts a slope of -2. The submesoscale wavenumber spectra derived over the CCS using a high-resolution model [19, 21] and High frequency (HF) radar currents [73] both show very good agreement with the k^{-2} power law. To date, many of the developments in submesoscale oceanography have been led by theory and modeling without observational validation; the spectra observed from HF radar surface current observations are very recent. The velocity wavenumber spectrum calculated from the derived MCC SAR currents follows the k^{-2} power law in the wavenumber range of 10^{-4} rad/m to 10^{-3} rad/m, in agreement with submesoscale resolution models and HF radar measurements. This also shows that MCC SAR currents can be used to directly measure the surface velocity of submesoscale processes. The development of surface variability in the CCS is known to be seasonal, with late summer containing more mesoscale features, due to upwelling and baroclinic instability, as compared to winter. The seasonal wavenumber spectra calculated along the California Coast clearly show these seasonal differences.

The derived MCC SAR currents are compared and validated against HF radar measured currents at 2 km and 6 km resolutions along the California Coast. Complex correlation and analysis of residuals shows that while the datasets show reasonable agreement in current vector direction, the MCC SAR currents are oriented counter-clockwise relative to HF radar currents; this mean counter-clockwise orientation has values of 5.5° and 11.5° for the 2 km and 6 km datasets, respectively. In magnitude, MCC SAR vectors show a higher magnitude bias of 11.7 cm/s and 10.6 cm/s for the 2 km and 6 km datasets, respectively. Along- and cross-shore rotation of the current vectors shows that this magnitude difference occurs primarily in the along-shore component (6 cm/s and 6.8 cm/s for the 2 km and 6 km datasets, respectively) and is negligible (<1 cm/s) in the cross-shore component. This bias concentration in the along-shore component can be attributed to the HF radar current measurement method, where direct velocity measurements are made in only cross-shore radial direction, and radial velocities from two or more HF radar stations are used to acquire a full 2-D vector solution. Besides the mean bias values indicated above, the histograms of all residuals are unimodal and mean-symmetric, indicating that the overall errors between he two datasets are random in nature. Better agreement of MCC SAR currents with 2 km HF radar datasets, instead of 6 km resolution datasets, shows that the MCC SAR method is fundamentally measuring high resolution current fields. Initial estimates of surface Stokes drift point towards the significant impact of Stokes drift in comparisons between MCC Synthetic Aperture Radar (SAR) and HF radar currents fields.

Doppler Centroid Cross-Track (XT) radial currents from Envisat Wide Swath Mode (WSM) scenes are compared with 6 km resolution HF radar radial currents, and are seen to have much larger extreme values, which is attributed to the Doppler wind correction process. Ignoring the extreme values, errors between the two datasets appear to be random, with a small mean positive bias of 1 cm/s in the Doppler radials. It is known that Doppler radial estimation Root Mean Square Error (RMSE) increases with incidence angle. Analysis of residuals, and inter-comparison between RMSE for Doppler radial current estimation & Root Mean Square Deviation (RMSD) between the two datasets is conducted for each sub-swath of the WSM scenes. Results from both analyses show that differences between Doppler and HF radar radials are not independent of incidence angle. Overall, both current measurement methods are deduced to be sampling the same geophysical fields. Comparison of Doppler radials with MCC SAR radials for two ≈12-hour lag cases also shows promising results, and similar spatial patterns can be seen in both datasets.

The use of TerraSAR-X Along-Track Interferometry (ATI) datasets acquired through the Dual Receive Aperture (DRA) mode is restricted because of lack of absolute phase calibration. Analysis of these datasets is restricted to scenes with adequate stationary land in them. Experiments conducted with a few DRA mode ATI datasets show that in certain cases, it may be possible to derive the phase trend for absolute calibration from the ocean phase itself. Trends estimated over land and ocean both show similar behavior in the larger wavenumbers, and in some cases, absolute calibration using both trends shows similar behavior in their wavenumber power distribution. In the one case shown, the phases seem to be in the same general range of values for calibration done by trends over land and ocean. Further refinement of this analysis may point towards more general methods for calibration without using land.

6.2 Future Work

Several suggestions and recommendations are now made for future work:

- **Processing the Envisat ERS-2 30-min lag images at their native 12.5 m.** For this research, the SAR images were down-sampled by a factor of 2 as an initial step before processing. This was mainly done to save on processing time and under the assumption that advection of surface slicks being measured would not show noticeable fluctuation at such a high resolution. However, processing of this data at the highest available resolution may give further insights in to the submeoscale processes and dynamics in the CCS.

- **Running MCC with SAR pairs of time lag greater than 30 minutes.** This research has demonstrated that 30-min lag between SAR images can be used in most conditions for determining surface current advection, and surface slick features do not decorrelate during this short time-lag. There has been some evidence that it might be possible to determine surface slick advection with slightly higher time-lag (see Table 1.2); the maximum time-lag ever utilized for SAR measurement of biogenic surface slick advection has been 100 minutes. At the same time, the discussion in Sec. 3.2.1 shows the possibility of biogenic slicks being correlated for higher time intervals also. It would be interesting to explore SAR image pairs with higher time-lags for this purpose. One possibility is to use either Envisat ASAR or TerraSAR-X (TSX) ascending-descending orbit image pair, with a time lag of ≈12 hours. TerraSAR-X, however, operates in X-band, rather than C-band, and it would be interesting to see how well X-band frequency performs for biogenic slick delineation and tracking. Other possibilities are to use datasets from multiple SAR satellites operating at different frequencies, which may give overlapping datasets in the same day. While they may not be in the same orbit, reasonable accurate geolocation of acquired images makes multiple-satellite SAR images well-suited for biogenic slick tracking through the MCC method.

- **Running MCC utilizing the lower resolution Envisat WSM mode images.** Envisat ASAR operates in the WSM mode at 150 m nominal resolution and 400 km swath width. Often, ASAR images are captured in the WSM mode instead of the high resolution stripmap mode (which was used for MCC SAR currents generation in this research), and even though a corresponding ERS-2 stripmap image with 30-min lag was available, such pairs were not taken into consideration because of lower WSM mode resolution. It would be interesting to explore what 30-min lag image pairs at an effective resolution of 150 m could show us in terms of biogenic slick advection. It would also be useful to experiment with WSM image pairs captured in the ≈12 hour lag Envisat ascending-descending orbits.

- **Changing size of pattern subwindow in MCC SAR processing.** The size of the template subwindow used for MCC processing in this research was chosen to be 1.1 km x 1.1 km (44 x 44 pixels), adequate enough to track biogenic slick features in the range of tens of meters up to 2-3 km, yet small enough to not smooth out the fine-resolution during correlation feature matching. Yet, this size was chosen empirically for development and successful demonstration of the method; it should be useful in the future to test the algorithm performance with different sizes for the pattern subwindow. Some flow features, e.g. eddy flow, may be better resolved with larger pattern subwindow sizes, as it would capture large-scale motions in a better manner. Furthermore, submesoscale models have shown [19–21] that the submesoscale energy increases with increasing model resolution, while the mesoscale range energy remains roughly constant with resolution. Processing MCC SAR currents with different pattern subwindow sizes will allow comparison with this spectral behavior from actual current observations.

Bibliography

[1] Mark R. Abbott and Ricardo M. Letelier. Decorrelation scales of chlorophyll as observed from bio-optical drifters in the California Current. Deep Sea Research Part II: Topical Studies in Oceanography, 45(8-9):1639–1667, August 1998.

[2] T. L. Ainsworth, Scott R. Chubb, R. A. Fusina, R. M. Goldstein, R. W. Jansen, and G. R. Valenzuela. INSAR imagery of surface currents, wave fields, and fronts. IEEE Transactions on Geoscience and Remote Sensing, 33(5):1117–1123, 1995.

[3] Werner Alpers and Heidi A. Espedal. Oils and surfactants. In Christopher R. Jackson and John R. Apel, editors, Synthetic Aperture Radar Marine User's Manual, chapter 11, pages 263–275. National Oceanic and Atmospheric Administration, Washington, D. C., 2004.

[4] Werner Alpers and Heinrich Hühnerfuss. The Damping of Ocean Waves by Surface Films: A New Look at an Old Problem. Journal of Geophysical Research, 94(C5):6251–6265, 1989.

[5] Werner Alpers, Duncan B. Ross, and C. L. Rufenach. On the Detectability of Ocean Surface Waves by Real and Synthetic Aperture Radar. Journal of Geophysical Research, 86(C7):6481–6498, 1981.

[6] Werner Alpers, Volkmar Wismann, Reinhard Theis, Heinrich Hühnerfuss, Norbert Bartsch, Joao Moreira, and J. D. Lyden. The damping of ocean surface waves by monomolecular sea slicks measured by airborne multi-frequency radars during the SAXON-FPN experiment. In [Proceedings] IGARSS'91 Remote Sensing: Global Monitoring for Earth Management, volume 4, pages 1987–1990. IEEE, 1991.

[7] Fabrice Ardhuin, Alastair D. Jenkins, Daniéle Hauser, Ad Reniers, and Bertrand Chapron. Waves and operational oceanography: Toward a coherent description of the upper ocean. Eos, Transactions American Geophysical Union, 86(4):37, 2005.

[8] Fabrice Ardhuin, Louis Marié, Nicolas Rascle, Philippe Forget, and Aron Roland. Observation and Estimation of Lagrangian, Stokes, and Eulerian Currents Induced by Wind and Waves at the Sea Surface. Journal of Physical Oceanography, 39(11):2820–2838, November 2009.

[9] Richard Bamler and Philipp Hartl. Synthetic aperture radar interferometry. Inverse Problems, 14(4):R1–R54, August 1998.

[10] Corinne J. Bassin, Libe Washburn, Mark A. Brzezinski, and Erika McPhee-Shaw. Sub-mesoscale coastal eddies observed by high frequency radar: A new mechanism for delivering nutrients to kelp forests in the Southern California Bight. Geophysical Research Letters, 32(12):L12604, 2005.

[11] Andrew F. Bennett and Kenneth L. Denman. Phytoplankton patchiness: inferences from particle statistics. Journal of Marine Research, 43(2):307–335, May 1985.

[12] William C. Boicourt, William J. Wiseman, Jr., Arnoldo Valle-Levinson, and Larry P. Atkinson. Continental shelf of the Southeastern United States and Gulf of Mexico: In the shadow of the Western Boundary Current. In Allan R. Robinson and K. H. Brink, editors, The Sea, Vol. 11, chapter 6, pages 135–182. John Wiley & Sons, Inc., Hoboken, NJ, 1998.

[13] Vincenzo Botte and Daniela Mansutti. Numerical modelling of the Marangoni effects induced by plankton-generated surfactants. Journal of Marine Systems, 57(1-2):55–69, August 2005.

[14] Melissa M. Bowen, W. J. Emery, John L. Wilkin, Paul C. Tildesley, Ian J. Barton, and Rebecca Knewtson. Extracting multiyear surface currents from sequential thermal imagery using the maximum cross-correlation technique. Journal of Atmospheric and Oceanic Technology, 19(10):1665–1676, 2002.

[15] Gary S. Brown. Backscattering from a Gaussian-distributed perfectly conducting rough surface. IEEE Transactions on Antennas and Propagation, 26(3):472–482, May 1978.

[16] Gary S. Brown. A comparison of approximate theories for scattering from rough surfaces. Wave Motion, 7(2):195–205, March 1985.

[17] O B Brown, R. H. Evans, J. W. Brown, H. R. Gordon, R. C. Smith, and K. S. Baker. Phytoplankton blooming off the u.s. East coast: a satellite description. Science (New York, N.Y.), 229(4709):163–7, July 1985.

[18] Xavier Capet, Patrice Klein, Bach Lien Hua, Guillaume Lapeyre, and James C. Mcwilliams. Surface kinetic energy transfer in surface quasi-geostrophic flows. Journal of Fluid Mechanics, 604:165–174, May 2008.

[19] Xavier Capet, J. C. McWilliams, M. J. Molemaker, and A. F. Shchepetkin. Mesoscale to Submesoscale Transition in the California Current System. Part I: Flow Structure, Eddy Flux, and Observational Tests. Journal of Physical Oceanography, 38(1):29–43, January 2008.

[20] Xavier Capet, J. C. McWilliams, M. J. Molemaker, and A. F. Shchepetkin. Mesoscale to Submesoscale Transition in the California Current System. Part II: Frontal Processes. Journal of Physical Oceanography, 38(1):44–64, January 2008.

[21] Xavier Capet, J. C. McWilliams, M. J. Molemaker, and A. F. Shchepetkin. Mesoscale to Submesoscale Transition in the California Current System. Part III: Energy Balance and Flux. Journal of Physical Oceanography, 38(10):2256–2269, October 2008.

[22] Bertrand Chapron, Fabrice Collard, and Fabrice Ardhuin. Direct measurements of ocean surface velocity from space: Interpretation and validation. Journal of Geophysical Research, 110(C7):1–17, 2005.

[23] David M. Checkley and John A. Barth. Patterns and processes in the California Current System. Progress In Oceanography, 83(1-4):49–64, December 2009.

[24] Scott R. Chubb, Richard P. Mied, Colin Y. Shen, Wei Chen, Thomas E. Evans, and Josh Kohut. Ocean Surface Currents From AVHRR Imagery: Comparison With Land-Based HF Radar Measurements. IEEE Transactions on Geoscience and Remote Sensing, 46(11):3647–3660, November 2008.

[25] A. Ciappa, L. Pietranera, A. Coletta, and Xingwei Jiang. Surface transport detected by pairs of COSMO-SkyMed ScanSAR images in the Qingdao region (Yellow Sea) during a macro-algal bloom in July 2008. Journal of Marine Systems, 80(1-2):135–142, February 2010.

[26] Pablo Clemente-Colón. Evolution of upwelling-associated biological features in the Middle Atlantic Bight as captured by SAR, SST, and ocean color sensors. In IGARSS 2001. Scanning the Present and Resolving the Future. Proceedings. IEEE 2001 International Geoscience and Remote Sensing Symposium (Cat. No.01CH37217), volume 6, pages 2616–2618. IEEE, 2001.

[27] Pablo Clemente-Colón and Xiao-Hai Yan. Observations of East Coast upwelling conditions in synthetic aperture radar imagery. IEEE Transactions on Geoscience and Remote Sensing, 37(5):2239–2248, 1999.

[28] R. Ian Crocker, D. K. Matthews, W. J. Emery, and Daniel G. Baldwin. Computing Coastal Ocean Surface Currents From Infrared and Ocean Color Satellite Imagery. IEEE Transactions on Geoscience and Remote Sensing, 45(2):435–447, February 2007.

[29] John C. Curlander and Robert N. McDonough. Synthetic Aperture Radar: Systems and Signal Processing. Wiley-Interscience, 1991.

[30] Kenneth L. Denman and Mark R. Abbott. Time scales of pattern evolution from cross-spectrum analysis of advanced very high resolution radiometer and coastal zone color scanner imagery. Journal of Geophysical Research, 99(C4):7433, 1994.

[31] Paul M. DiGiacomo and Benjamin Holt. Satellite observations of small coastal ocean eddies in the Southern California Bight. Journal of Geophysical Research, 106(C10):22521–22543, 2001.

[32] Henk A. Dijkstra. Dynamical Oceanography. Springer, 2008.

[33] Charles Elachi and Jakob J. van Zyl. Introduction to the Physics and Techniques of Remote Sensing. Wiley-Interscience, 2 edition, 2006.

[34] Tanos M. Elfouhaily and Charles-Antoine Guérin. A critical survey of approximate scattering wave theories from random rough surfaces. Waves in Random and Complex Media, 14(4):R1–R40, October 2004.

[35] W. J. Emery, Daniel G. Baldwin, and D. K. Matthews. Sampling the mesoscale ocean surface currents with various satellite altimeter configurations. IEEE Transactions on Geoscience and Remote Sensing, 42(4):795–803, April 2004.

[36] W. J. Emery, A. C. Thomas, M. J. Collins, W. R. Crawford, and D. L. Mackas. An objective method for computing advective surface velocities from sequential infrared satellite images. Journal of Geophysical Research, 91(C11):12865–12878, 1986.

[37] William J. Emery and Richard E. Thompson. Data Analysis Methods in Physical Oceanography. Elsevier Science, 2nd edition, 2001.

[38] H.-H. Essen, Klaus-Werner Gurgel, and T. Schlick. On the accuracy of current measurements by means of HF radar. IEEE Journal of Oceanic Engineering, 25(4):472–480, 2000.

[39] G. Ferrier, J. T. Macklin, S. P. Neill, A. M. Folkard, G. Copeland, and J. M. Anderson. Observing estuarine currents and fronts in the Tay Estuary, Scotland, using an airborne SAR with along-track interferometry (ATI). International Journal of Remote Sensing, 26(20):4399–4404, October 2005.

[40] Giorgio Franceschetti and Riccardo Lanari. Synthetic Aperture Radar Processing. CRC Press, 1999.

[41] Stephen J. Frasier and Adriano J. Camps. Dual-beam interferometry for ocean surface current vector mapping. IEEE Transactions on Geoscience and Remote Sensing, 39(2):401–414, 2001.

[42] Paula S. Fratantoni and Robert S. Pickart. The Western North Atlantic Shelfbreak Current System in Summer. Journal of Physical Oceanography, 37(10):2509–2533, October 2007.

[43] A. K. Fung and K. S. Chen. Dependence of the surface backscattering coefficients on roughness, frequency and polarization states. International Journal of Remote Sensing, 13(9):1663–1680, June 1992.

[44] A. K. Fung, Zongqian Li, and K. S. Chen. Backscattering from a randomly rough dielectric surface. IEEE Transactions on Geoscience and Remote Sensing, 30(2):356–369, March 1992.

[45] Martin Gade, Werner Alpers, Heinrich Hühnerfuss, Volkmar R. Wismann, and Philipp A. Lange. On the Reduction of the Radar Backscatter by Oceanic Surface Films: Scatterometer Measurements and Their Theoretical Interpretation. Remote Sensing of Environment, 66(1):52–70, October 1998.

[46] Martin Gade, Ove Rud, and M. Ishii. Monitoring algae blooms in the Baltic Sea by using spaceborne optical and microwave sensors. In IGARSS '98. Sensing and Managing the Environment. 1998 IEEE International Geoscience and Remote Sensing. Symposium Proceedings. (Cat. No.98CH36174), volume 2, pages 754–756. IEEE, 1998.

[47] Martin Gade, Benjamin Seppke, and Leonie Dreschler-Fischer. Mesoscale surface current fields in the Baltic Sea derived from multi-sensor satellite data. International Journal of Remote Sensing, 33(10):3122–3146, May 2012.

[48] R. M. Goldstein and H. A. Zebker. Interferometric radar measurement of ocean surface currents. Nature, 328(20):707–709, 1987.

[49] R. M. Goldstein, H. A. Zebker, and T. P. Barnett. Remote sensing of ocean currents. Science (New York, N.Y.), 246(4935):1282–5, December 1989.

[50] Rafael C. Gonzalez and Richard E. Woods. Digital Image Processing. Pearson Education, 2nd edition, 2002.

[51] Hans C. Graber, Brian K. Haus, Rickey D. Chapman, and Lynn K. Shay. HF radar comparisons with moored estimates of current speed and direction: Expected differences and implications. Journal of Geophysical Research, 102(C8):18749–18766, 1997.

[52] Hans C. Graber, Donald R. Thompson, and Richard E. Carande. Ocean surface features and currents measured with synthetic aperture radar interferometry and HF radar. Journal of Geophysical Research, 101(C11):25813–25832, 1996.

[53] C. Guillou, W. Ellison, L. Eymard, K. Lamkaouchi, C. Prigent, G. Delbos, G. Balana, and S. A. Boukabara. Impact of new permittivity measurements on sea surface emissivity modeling in microwaves. Radio Science, 33(3):649–667, May 1998.

[54] T. Hamre and Heidi A. Espedal. Operational use of wind data for slick detection. In 3rd ERS Symp. on Space at the Service of our Environment, pages 1417–1421, Florence, 1997.

[55] Morten W. Hansen, Fabrice Collard, Knut-Frode Dagestad, Johnny Johannessen, Pierre Fabry, and Bertrand Chapron. Retrieval of Sea Surface Range Velocities From Envisat ASAR Doppler Centroid Measurements. IEEE Transactions on Geoscience and Remote Sensing, 49(10):3582–3592, 2011.

[56] Morten W. Hansen, Johnny Johannessen, Knut-Frode Dagestad, Fabrice Collard, and Bertrand Chapron. Monitoring the surface inflow of Atlantic Water to the Norwegian Sea using Envisat ASAR. Journal of Geophysical Research, 116(C12008):1–13, 2011.

[57] Morten W. Hansen, Johnny A. Johannessen, and Roshin Raj. Mapping the Nordic Seas surface velocity using Envisat ASAR. In Pan Ocean Remote Sensing Conference (PORSEC) 2012, Kochi, Kerala, November 2012. Indian National Centre for Ocean Information Services (INCOIS).

[58] K. Hasselmann, T. P. Barnett, E. Bouws, H. Carlson, D. E. Cartwright, K. Enke, J. A. Ewing, H. Gienapp, D. E. Hasselmann, P. Kruseman, A. Meerburg, P. Mller, D. J. Olbers, K. Richter, W. Sell, and H. Walden. Measurements of wind-wave growth and swell decay during the Joint North Sea Wave Project (JONSWAP). Ergänzungsheft zur Deutschen Hydrographischen Zeitschrift Reihe, 8(12):1–95, 1973.

[59] K. Hasselmann and S. Hasselmann. On the Nonlinear Mapping of an Ocean Wave Spectrum Into a Synthetic Aperture Radar Image Spectrum and Its Inversion. Journal of Geophysical Research, 96(C6):10713–10729, 1991.

[60] K. Hasselmann, R. K. Raney, W. J. Plant, Werner Alpers, R. A. Shuchman, David R. Lyzenga, C. L. Rufenach, and M. J. Tucker. Theory of Synthetic Aperture Radar Ocean Imaging: A MARSEN View. Journal of Geophysical Research, 90(C3):4659–4686, 1985.

[61] Stephanie A. Henson and Andrew C. Thomas. Phytoplankton scales of variability in the California Current System: 2. Latitudinal variability. Journal of Geophysical Research, 112(C7):C07018, July 2007.

[62] Barbara M. Hickey. Coastal oceanography of Western North America from the tip of Baja California to Vancouver Island. In Allan R. Robinson and Kenneth H. Brink, editors, The Sea, Vol. 11, chapter 12. John Wiley & Sons, Inc., Hoboken, NJ, 1998.

[63] Benjamin Holt. SAR Imaging of the Ocean Surface. In Christopher R. Jackson and John R. Apel, editors, Synthetic Aperture Radar Marine User's Manual, chapter 2, pages 25–79. National Oceanic and Atmospheric Administration, Washington, D. C., 2004.

[64] H. A. Hovland, Johnny Johannessen, and G. Digranes. Slick detection in SAR images. In Proceedings of IGARSS '94 - 1994 IEEE International Geoscience and Remote Sensing Symposium, volume 4, pages 2038–2040. IEEE, 1994.

[65] Christopher R. Jackson and John R. Apel, editors. Synthetic Aperture Radar Marine User's Manual. National Oceanic and Atmospheric Administration, Washington, D. C., 2004.

[66] Johnny Johannessen, Bertrand Chapron, Fabrice Collard, V. Kudryavtsev, Alexis Mouche, D. Akimov, and Knut-Frode Dagestad. Direct ocean surface velocity measurements from space: Improved quantitative interpretation of Envisat ASAR observations. Geophysical Research Letters, 35(L22608), 2008.

[67] M. Kahru, J.-M. Leppanen, and Ove Rud. Cyanobacterial blooms cause heating of the sea surface. Marine Ecology Progress Series, 101:1–7, 1993.

[68] Dayalan P. Kasilingam and Omar H. Shemdin. Models for Synthetic Aperture Radar Imaging of the Ocean: A Comparison. Journal of Geophysical Research, 95(C9):16263–16276, 1990.

[69] Duk-jin Kim, W. M. Moon, and Yoon-Soo Kim. Application of TerraSAR-X Data for Emergent Oil-Spill Monitoring. IEEE Transactions on Geoscience and Remote Sensing, 48(2):852–863, February 2010.

[70] Sung Yong Kim. Observations of submesoscale eddies using high-frequency radar-derived kinematic and dynamic quantities. Continental Shelf Research, 30(15):1639–1655, September 2010.

[71] Sung Yong Kim, Eric J. Terrill, and Bruce D. Cornuelle. Objectively mapping HF radar-derived surface current data using measured and idealized data covariance matrices. Journal of Geophysical Research, 112(C6):1–16, June 2007.

[72] Sung Yong Kim, Eric J. Terrill, and Bruce D. Cornuelle. Mapping surface currents from HF radar radial velocity measurements using optimal interpolation. Journal of Geophysical Research, 113(C10):1–16, October 2008.

[73] Sung Yong Kim, Eric J. Terrill, Bruce D. Cornuelle, Burt Jones, Libe Washburn, Mark A. Moline, Jeffrey D. Paduan, Newell Garfield, John L. Largier, Greg Crawford, and P. Michael Kosro. Mapping the U.S. West Coast surface circulation: A multiyear analysis of high-frequency radar observations. Journal of Geophysical Research, 116(C3):1–15, March 2011.

[74] Lawrence A. Klein and Calvin T. Swift. An improved model for the dielectric constant of sea water at microwave frequencies. IEEE Journal of Oceanic Engineering, 2(1):104–111, January 1977.

[75] Patrice Klein, Bach Lien Hua, Guillaume Lapeyre, Xavier Capet, Sylvie Le Gentil, and Hideharu Sasaki. Upper Ocean Turbulence from High-Resolution 3D Simulations. Journal of Physical Oceanography, 38(8):1748–1763, August 2008.

[76] Pijush K. Kundu. Ekman Veering Observed near the Ocean Bottom. Journal of Physical Oceanography, 6(2):238–242, March 1976.

[77] Philipp Lange and Heinrich Hühnerfuss. Drift Response of Monomolecular Slicks to Wave and Wind Action. Journal of Physical Oceanography, 8(1):142–150, January 1978.

[78] P. Y. Le Traon, Patrice Klein, Bach Lien Hua, and G. Dibarboure. Do altimeter wavenumber spectra agree with the Interior or Surface Quasigeostrophic theory? Journal of Physical Oceanography, 38(5):1137–1142, May 2008.

[79] J. Carl Leader. Incoherent backscatter from rough surfaces: The two-scale model reexamined. Radio Science, 13(3):441–457, May 1978.

[80] A. K. Liu and Ming-Kuang Hsu. Deriving Ocean Surface Drift Using Multiple SAR Sensors. Remote Sensing, 1(3):266–277, July 2009.

[81] John W. Loder, B. Petrie, and G. Gawarkiewicz. The coastal ocean off Northeastern North America: A large-scale view. In Allan R. Robinson and K. H. Brink, editors, The Sea, Vol. 11, chapter 5, pages 105–133. John Wiley & Sons, Inc., Hoboken, NJ, 1998.

[82] David R. Lyzenga and George O. Marmorino. Measurement of surface currents using sequential synthetic aperture radar images of slick patterns near the edge of the Gulf Stream. Journal of Geophysical Research, 103(C9):18769–18777, 1998.

[83] Amala Mahadevan and Janet W. Campbell. Biogeochemical variability at the sea surface: how it is linked to process response times. In L. Seuront and B. P. G. Strutton, editors, Handbook of Scaling Methods in Aquatic Ecology: Measurement, Analysis, Simulation, chapter 14, pages 215–227. CRC Press, 2003.

[84] H. Maitre, editor. Processing of Synthetic Aperture Radar Images. Wiley-ISTE, 2008.

[85] George O. Marmorino, Benjamin Holt, M. Jeroen Molemaker, Paul M. DiGiacomo, and Mark A. Sletten. Airborne synthetic aperture radar observations of spiral eddy slick patterns in the Southern California Bight. Journal of Geophysical Research, 115(C5):1–14, May 2010.

[86] George O. Marmorino, David R. Lyzenga, and J. A. C. Kaiser. Comparison of airborne synthetic aperture radar imagery with in situ surface-slope measurements across Gulf Stream slicks and a convergent front. Journal of Geophysical Research, 104(C1):1405–1422, 1999.

[87] George O. Marmorino, Geoffrey B. Smith, Jakov V. Toporkov, Mark A. Sletten, Dragana Perkovic, and Stephen J. Frasier. Evolution of ocean slicks under a rising wind. Journal of Geophysical Research, 113(C4):C04030, April 2008.

[88] Thomas Meissner and Frank J. Wentz. The complex dielectric constant of pure and sea water from microwave satellite observations. IEEE Transactions on Geoscience and Remote Sensing, 42(9):1836–1849, September 2004.

[89] Antonio Moccia and Giancarlo Rufino. Spaceborne along-track SAR interferometry: performance analysis and mission scenarios. IEEE Transactions on Aerospace and Electronic Systems, 37(1):199–213, 2001.

[90] D. Moller, Stephen J. Frasier, David L. Porter, and Robert E. McIntosh. Radar-derived interferometric surface currents and their relationship to subsurface current structure. Journal of Geophysical Research, 103(C6):12839–12852, 1998.

[91] W.M. Moon, D. Moller, and D.A. Imel. Measurements of ocean surface waves and currents using L- and C-band along-track interferometric SAR. IEEE Transactions on Geoscience and Remote Sensing, 41(12):2821–2832, December 2003.

[92] G. Nico, G. Palubinskas, and M. Datcu. Bayesian approaches to phase unwrapping: theoretical study. IEEE Transactions on Signal Processing, 48(9):2545–2556, 2000.

[93] Ferdinando Nunziata, Piotr Sobieski, and Maurizio Migliaccio. The Two-Scale BPM Scattering Model for Sea Biogenic Slicks Contrast. IEEE Transactions on Geoscience and Remote Sensing, 47(7):1949–1956, July 2009.

[94] P. Pavlakis, D. Tarchi, and A. J. Sieber. On the monitoring of illicit vessel discharges using spaceborne SAR remote sensing - a reconnaissance study in the Mediterranean sea. Annals OF Telecommunications, 56(11-12):700–718, 2001.

[95] Dragana Perkovic, J.V. Toporkov, M.A. Sletten, Gordon Farquharson, S.J. Frasier, G.O. Marmorino, and K.P. Judd. Gulf Stream observations obtained with the UMass dual beam interferometer and an infrared camera. In IEEE International IEEE International IEEE International Geoscience and Remote Sensing Symposium, 2004. IGARSS '04. Proceedings. 2004, volume 5, pages 3325–3328. IEEE, 2004.

[96] William G. Pichel, Pablo Clemente-Colón, Christopher R. Wackerman, and Karen S. Friedman. Ship and Wake Detection. In Christopher R. Jackson and John R. Apel, editors, Synthetic Aperture Radar Marine User's Manual, chapter 12, pages 277–303. National Oceanic and Atmospheric Administration, Washington, D. C., 2004.

[97] Mark H. Pickett and Jeffrey D. Paduan. Ekman transport and pumping in the California Current based on the U.S. Navy's high-resolution atmospheric model (COAMPS). Journal of Geophysical Research, 108(C10):1–10, 2003.

[98] Willard J. Pierson and Lionel Moskowitz. A proposed spectral form for fully developed wind seas based on the similarity theory of S. A. Kitaigorodskii. Journal of Geophysical Research, 69(24):5181–5190, December 1964.

[99] William J. Plant. A stochastic, multiscale model of microwave backscatter from the ocean. Journal of Geophysical Research, 107(C9):1–21, 2002.

[100] William J. Plant and William C. Keller. Evidence of Bragg scattering in microwave Doppler spectra of sea return. Journal of Geophysical Research, 95(C9):16299, 1990.

[101] S. Pond and George L. Pickard. Introductory Dynamical Oceanography. Pergamon Press, 2nd edition, 1983.

[102] Thomas M. Powell, Craig V. W. Lewis, Enrique N. Curchitser, Dale B. Haidvogel, Albert J. Hermann, and Elizabeth L. Dobbins. Results from a three-dimensional, nested biological-physical model of the California Current System and comparisons with statistics from satellite imagery. Journal of Geophysical Research, 111(C7):C07018, 2006.

[103] John A. Richards. Remote Sensing with Imaging Radar. Signals and Communication Technology. Springer Berlin Heidelberg, Berlin, Heidelberg, 2009.

[104] Carolyn Roesler, William J. Emery, and Waqas A. Qazi. Using HF radar coastal currents to correct satellite altimetry. In Proc. 4th Coastal Altimetry Workshop, Porto, Portugal, October 2010.

[105] Roland Romeiser, Werner Alpers, and Volkmar Wismann. An improved composite surface model for the radar backscattering cross section of the ocean surface 1. Theory of the model and optimization/validation by scatterometer data. Journal of Geophysical Research, 102(C11):25237–25250, 1997.

[106] Roland Romeiser, Helko Breit, Michael Eineder, Hartmut Runge, Pierre Flament, and J. Vogelzang. Current measurements by SAR along-track interferometry from a Space Shuttle. IEEE Transactions on Geoscience and Remote Sensing, 43(10):2315–2324, October 2005.

[107] Roland Romeiser and Hartmut Runge. Theoretical evaluation of several possible Along-Track InSAR modes of TerraSAR-X for ocean current measurements. IEEE Transactions on Geoscience and Remote Sensing, 45(1):21–35, January 2007.

[108] Roland Romeiser, Hartmut Runge, Steffen Suchandt, Judith Sprenger, Holger Weilbeer, Ariane Sohrmann, and Detlef Stammer. Current measurements in rivers by spaceborne Along-Track InSAR. IEEE Transactions on Geoscience and Remote Sensing, 45(12):4019–4031, December 2007.

[109] Roland Romeiser, Anke Schmidt, and Werner Alpers. A three-scale composite surface model for the ocean waveradar modulation transfer function. Journal of Geophysical Research, 99(C5):9785–9801, 1994.

[110] Roland Romeiser, Steffen Suchandt, Hartmut Runge, and Hans Graber. Currents in rivers, coastal areas, and the open ocean from TerraSAR-X along-track InSAR. In 2010 IEEE International Geoscience and Remote Sensing Symposium, pages 3059–3062. IEEE, July 2010.

[111] Roland Romeiser, Steffen Suchandt, Hartmut Runge, Ulrich Steinbrecher, and S. Grunler. First analysis of TerraSAR-X Along-Track InSAR-derived current fields. IEEE Transactions on Geoscience and Remote Sensing, 48(2):820–829, February 2010.

[112] Roland Romeiser and Donald R. Thompson. Numerical study on the along-track interferometric radar imaging mechanism of oceanic surface currents. IEEE Transactions on Geoscience and Remote Sensing, 38(1):446–458, 2000.

[113] M. J. Rouault, A. Mouche, Fabrice Collard, Johnny Johannessen, and Bertrand Chapron. Mapping the Agulhas Current from space: An assessment of ASAR surface current velocities. Journal of Geophysical Research, 115(C10):1–14, October 2010.

[114] J. H. Ryther. Photosynthesis and Fish Production in the Sea. Science, 166(3901):72–76, October 1969.

[115] Johannes Schulz-Stellenfleth, Irena Hajnsek, and Susanne Lehner. Use of Tandem-X in a Squinted Split Antenna Mode Configuration to Retrieve 2-D Current and Ocean Wave Information. In 2006 IEEE International Symposium on Geoscience and Remote Sensing, pages 2408–2411. IEEE, July 2006.

[116] L. Shemer, M. Marom, and D. Markman. Estimates of currents in the nearshore ocean region using interferometric Synthetic Aperture Radar. Journal of Geophysical Research, 98(C4):7001–7010, 1993.

[117] M. D. Simon and A. K. Geim. Diamagnetic levitation: Flying frogs and floating magnets (invited). Journal of Applied Physics, 87(9):6200, 2000.

[118] Jerome A. Smith. Observed variability of ocean wave stokes drift, and the Eulerian response to passing groups. Journal of Physical Oceanography, 36(7):1381–1402, July 2006.

[119] Detlef Stammer. Global characteristics of ocean variability estimated from regional TOPEX/POSEIDON altimeter Measurements. Journal of Physical Oceanography, 27(8):1743–1769, August 1997.

[120] Robert H. Stewart. Introduction to Physical Oceanography. Orange Grove Texts Plus, 2009.

[121] A. Stogryn. Equations for calculating the dielectric constant of saline water (Correspondence). IEEE Transactions on Microwave Theory and Techniques, 19(8):733–736, August 1971.

[122] P. Ted Strub and Corinne James. Altimeter-derived variability of surface velocities in the California Current System: 2. Seasonal circulation and eddy statistics. Deep Sea Research Part II: Topical Studies in Oceanography, 47(5-6):831–870, May 2000.

[123] Steffen Suchandt, Hartmut Runge, Helko Breit, Ulrich Steinbrecher, Alexander Kotenkov, and Ulrich Balss. Automatic extraction of traffic flows using TerraSAR-X Along-Track Interferometry. IEEE Transactions on Geoscience and Remote Sensing, 48(2):807–819, February 2010.

[124] Steffen Suchandt, Hartmut Runge, Roland Romeiser, Nuria Tous-Ramon, and Ulrich Steinbrecher. Tidal current measurement with TerraSAR-X Along-Track Interferometry. In 2010 IEEE International Geoscience and Remote Sensing Symposium, pages 2432–2435. IEEE, July 2010.

[125] J. Svejkovsky and J. Shandley. Detection of offshore plankton blooms with AVHRR and SAR imagery. International Journal of Remote Sensing, 22(2-3):471–485, January 2001.

[126] Donald R. Thompson. Microwave scattering from the sea. In Christopher R. Jackson and John R. Apel, editors, Synthetic Aperture Radar Marine User's Manual, chapter 4, pages 117–138. National Oceanic and Atmospheric Administration, Washington, D. C., 2004.

[127] K. R. Thompson, D. E. Kelley, D. Sturley, B. Topliss, and R. Leal. Nearshore circulation and synthetic aperture radar: An exploratory study. International Journal of Remote Sensing, 19(6):1161–1178, January 1998.

[128] Fawwaz T. Ulaby, Richard K. Moore, and A. K. Fung. Microwave remote sensing: active and passive. Addison-Wesley, 1986.

[129] Gaspar R. Valenzuela. Theories for the interaction of electromagnetic and oceanic waves - A review. Boundary-Layer Meteorology, 13(1-4):61–85, January 1978.

[130] A. G. Voronovich. Small-slope approximation for electromagnetic wave scattering at a rough interface of two dielectric half-spaces. Waves in Random and Complex Media, 4(3):337–367, July 1994.

[131] A. G. Voronovich. A two-scale model from the point of view of the small-slope approximation. Waves in Random and Complex Media, 6(1):73–83, January 1996.

[132] Vera Žutić, Božena Ćosović, Elena Marčenko, Nevenka Bihari, and Frano Kršinić. Surfactant production by marine phytoplankton. Marine Chemistry, 10(6):505–520, December 1981.

[133] Ronald E. Walpole, Raymond H. Myers, Sharon L. Myers, and Keying Ye. Probability & Statistics for Engineers & Scientists. Pearson Education, 7 edition, 2002.

[134] James R. Wang. A comparison of the MIR-estimated and model-calculated fresh water surface emissivities at 89, 150, and 220 GHz. IEEE Transactions on Geoscience and Remote Sensing, 40(6):1356–1365, June 2002.

[135] A. Webb and Baylor Fox-Kemper. Wave spectral moments and Stokes drift estimation. Ocean Modelling, 40(3-4):273–288, January 2011.

[136] Frank J. Wentz and Thomas Meissner. Algorithm Theoretical Basis Document (ATBD) Ver. 2: AMSR Ocean Algorithm. Technical report, Remote Sensing Systems, Santa Rosa, CA, 2000.

[137] John W. Wright. Backscattering from capillary waves with application to sea clutter. IEEE Transactions on Antennas and Propagation, 14(6):749–754, November 1966.

[138] John W. Wright. A new model for sea clutter. IEEE Transactions on Antennas and Propagation, 16(2):217–223, March 1968.

[139] Jin Wu. Sea-Surface Drift Currents Induced by Wind and Waves. Journal of Physical Oceanography, 13(8):1441–1451, August 1983.

[140] Li Xinming, Li Shixin, and Wei Hao. Theoretical study on coastal upwelling induced by alongshore current. Chinese Journal of Oceanology and Limnology, 10(3):239–257, September 1992.

Appendix A

Acronyms

ADCPs	Acoustic Doppler Current Profilers
AMI	Advanced Microwave Instrument
AS	Aperture Synthesis
ASAR	Advanced SAR
AT	Along-Track
ATI	Along-Track Interferometry
AVHRR	Advanced Very High Resolution Radiometer
CCS	California Current System
Chl-a	Chlorophyll-a
CI	confidence interval
CLS	Collecte Localisation Satellites
CNES	Centre National d'Etudes Spatiales
DOF	degrees of freedom
DRA	Dual Receive Aperture

ESA	European Space Agency
GEC	Ellipsoid Geocoded
HF	High frequency
IR	infrared
KE	Kinetic Energy
MCC	Maximum Cross-Correlation
MDT	mean dynamic topography
MODIS	Moderate-Resolution Imaging Spectroradiometer
MTF	modulation transfer function
NCEP	National Center for Environmental Prediction
OC	ocean color
PM	Pierson & Moskowitz
PRF	pulse repetition frequency
RMS	Root Mean Square
RMSD	Root Mean Square Deviation
RMSE	Root Mean Square Error
SAR	Synthetic Aperture Radar
SCB	Southern California Bight
SPM	Small Perturbation Model
SRTM	Shuttle Radar Topographic Mission

SSH	Sea Surface Height
SST	Sea Surface Temperature
TIR	thermal infrared
TSX	TerraSAR-X
WSM	Wide Swath Mode
XT	Cross-Track

Appendix B

Relative Permittivity of Sea Water

For water, the "complex relative permittivity (ϵ_{cr})", given by $\epsilon_{cr} = \epsilon_r^{'} - j\epsilon_r^{''}$, is a function of frequency and two physical parameters: temperature and salinity (amount of salt content in water). The dependence of ϵ_{cr} on angular frequency ω, temperature T, and salinity S can be described by an equation of the Debye form with a single relaxation wavelength [74]:

$$\epsilon_{cr}(T,S,\omega) = \epsilon_\infty + \frac{\epsilon_S(T,S) - \epsilon_\infty}{1 + [j\omega\tau(T,S)]^{1-\eta}} - j\frac{\sigma(T,S)}{\omega\epsilon_o} \tag{B.1}$$

where ϵ_∞ is the relative permittivity at infinite frequency, $\epsilon_S(T,S)$ is the relative static (zero-frequency) permittivity, $\tau\,(T,S)$ is the Debye relaxation time, η is the Cole-Cole spread factor, $\sigma(T,S)$ is the conductivity of water, and ϵ_o is the permittivity for vacuum. The Debye equation with $\epsilon_\infty = 4.9$ and $\eta = 0$ is the "standard Debye equation."

Stogryn [121] was the first to derive a regression model fit to experimental observations of relative permittivity observations using regression, called the "Stogryn Model". Klein & Swift [74] noted that the Stogryn model was not accurate enough for the demands of precision microwave radiometry. They developed an improved Stogryn model by fitting over more measurements that had become available by then, producing the "Klein-Swift Model." Both the Stogryn and Klein-Swift models used the standard Debye equation. The Klein-Swift model is accurate at low frequencies, but gets increasingly inaccurate at higher frequencies; Guillou et al. [53] and Wang [134] note that the Klein-Swift model is not accurate at frequencies higher than 10 GHz. The "Wentz Model" [136] was very similar to the Klein-Swift Model, but was improved by neglecting some conflicting experimental measurements for the fit, and using the non-standard Debye equation with $\epsilon_\infty = 4.44$ and $\eta = 0.012$. The "Meissner-Wentz Model" [88] uses a second Debye relaxation frequency in the basic Debye equation to achieve a better fit at higher frequencies. Comparative analysis in [88] shows that in the 1-15 GHz frequency range, the deviation between the models discussed above is negligible.

Appendix C

SAR Squint Angle

Normally a space-borne SAR acquires image data with the radar beam pointing perpendicularly to the flight path (Fig. 2.8), i.e. the angle between the radar beam and the flight direction is 90°. The radar beam look angle (Fig. 2.1, Fig. 2.8) is determined by the phased array antenna in the case of TerraSAR-X and TanDEM-X satellites. Any offset of the radar beam pointing angle from this perpendicular, w.r.t. the flight path, is called "squint angle" and is often used in SAR imaging for specific operations, e.g. spotlight mode imaging which requires longer SAR dwell time on a ground resolution cell than the regular stripmap mode [103], and as suggested by [115] for 2-D Along-Track Interferometry (ATI) ocean current retrieval using the TanDEM-X SAR satellite pair. The squint angle is graphically explained in Fig. C.1 (from [40]). In Fig. C.1a, it is clear that the SAR beam is in the plane perpendicular to the flight path, while in Fig. C.1b the SAR beam is no longer perpendicular to the flight path due to change in orientation of the SAR platform.

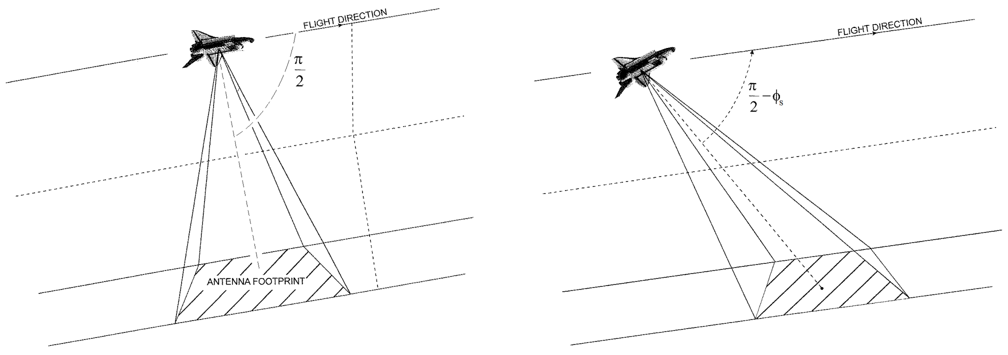

(a) SAR stripmap mode imaging geometry with no squint)

(b) SAR stripmap mode imaging geometry with squint angle ϕ_s)

Figure C.1: Illustration of SAR stripmap mode imaging with no squint (in (a)) and with squint angle ϕ_s relative to the center of the image (in (b)) (from [40]).

Appendix D

Wavenumber Spectra Calculation

The discussion and analysis of wavenumber spectra in Sec. 3.4 only briefly mentions how the spectra were specifically calculated. Detailed below are the steps for calculation of 1-D wavenumber spectra for each MCC SAR current fields. The spectra were calculated in MATLAB.

(1) Take row/column vector x from input current field, with constant spatial spacing $d = 1.9km$.

(2) Often the input vector is detrended and the mean is removed because it shows up as a low-wavenumber component in the spectrum. However, this depends upon the type of input data, and what is being looked for in the spectrum. In this case, the trend or mean are not removed because the power residing in lower wavenumbers is of interest.

(3) Replace missing values (NaN values) with zeros.

(4) Zero-pad both sides of vector x to bring it to a length N for Fourier transform, creating a new vector x_N. N is chosen to be 128 here; this is the nearest power of 2 to the maximum length of different x.

(5) Next, a Hann window H, of half-width M, is generated to condition the zero-padded vector x_N. The Hann window is also zero-padded on both sides to bring it to length N. M is chosen to be 45 here, for the following reasons:

    (a) It is required to have a reasonably wide mainlobe in wavenumber domain (smaller span in spatial domain) to make power spectrum amplitude measurements accurate as that is the primary interest here, instead of, for example, frequency peak delineation. At the same time, if M is too small (e.g. 10), the side-lobes are not suppressed enough.

(b) Choosing $M < \frac{N}{2}$ increases the effective degrees of freedom (DOF).

(c) Most input vectors x have to be zero-padded to get to a length $N = 128$, while the Hann window H needs to operate primarily on the actual values.

(6) Apply the Hann window to the input vector (in spatial domain):

$$y_N = x_N \times H_N$$

(7) Calculate the power spectrum through Fourier transform:

$$Y = |\mathcal{F}(y_N)|^2$$

(8) Extract one-sided power spectrum. This means scaling by 2, except for the first mean value in the spectrum:

$$Y = 2Y\,(1 : N/2 + 1)$$
$$Y(1) = \frac{Y(1)}{2}$$

Excluding the first mean value, the spectrum has a total length of $\frac{N}{2} = 64$ now.

(9) Determine the spectrum normalization factor b and perform spectrum normalization. For Hann window:

$$b = \frac{8}{3}\frac{d}{N} = 40.86$$
$$Y = b \times Y$$

(10) The above calculations are repeated for each row/column vector in the input current field, and a mean spectrum Y_{mean} is determined.

(11) For no windowing on the input vector x, the DOF value is simply $v = 2$. For Hann windowing, the DOF value is given by:

$$DOF = \frac{8}{3} \times \frac{N}{M} = 7.35$$

(12) For $DOF = 2$, the standard deviation of the spectrum estimate is equal to its mean, and the spectrum estimate is not very reliable. Using the Hann window increases DOF and shortens the confidence interval (CI) for the estimate. To further reduce the CI, band averaging in the wavenumber domain is employed. Band averaging is performed here over 3 wavenumber bands; for the one-sided spectrum, averaging over 3 bands gives a total number of bands $N_B = 21$. The DOF then increases to:

$$DOF = \frac{8}{3} \times \frac{N}{M} \times N_B = 154.35$$

(13) The confidence interval for the spectrum estimate is generally a function of the wavenumber values and DOF, and is thus variable over the whole spectrum. However, under the logarithmic transformation, the CI becomes independent of wavenumber and depends only on DOF [37]. That is why the 95% CI values indicated in the log-scale wavenumber spectrum plots are constant for the whole spectrum.

Appendix E

Additional Wavenumber Spectra for MCC SAR Currents

Wavenumber spectrum analysis for MCC SAR currents was performed in Sec. 3.4 using Kinetic Energy (KE) spectra calculated and averaged over both latitude and longitude. Here, more plots of wavenumber spectra are presented. For spectra calculation details, refer to Sec. 3.4.

It was earlier stated that the 1-D spectra calculated along latitude and longitude are very similar; this can be seen in Fig. E.1 which presents 1-D spectra calculated individually over latitude and longitude.

Spectra calculated over the u- and v-components of vector currents are presented in Fig. E.2.

The spectra presented in Sec. 3.4 are overall means, with no indication of individual spectral behavior of each current field. Fig E.3 shows the KE spectrum for each current field used for the spectrum calculation in Fig. 3.12 along with the mean value (which is the same as shown in Fig. 3.12).

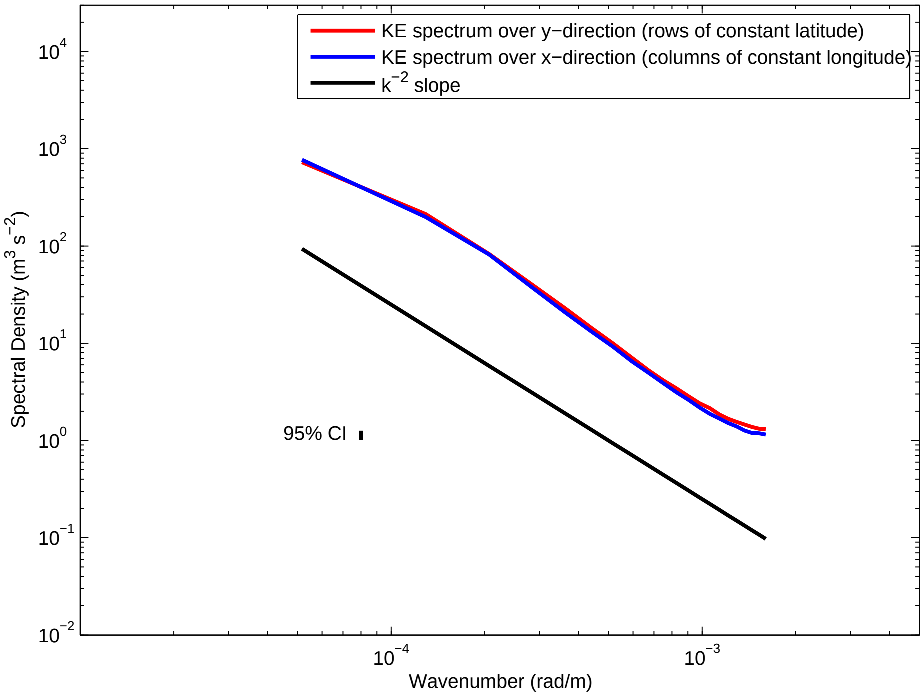

Figure E.1: Mean KE wavenumber spectra for MCC SAR currents calculated over each row of constant latitude and each column of constant longitude, averaged over a number of different times and scenes as described in the text.

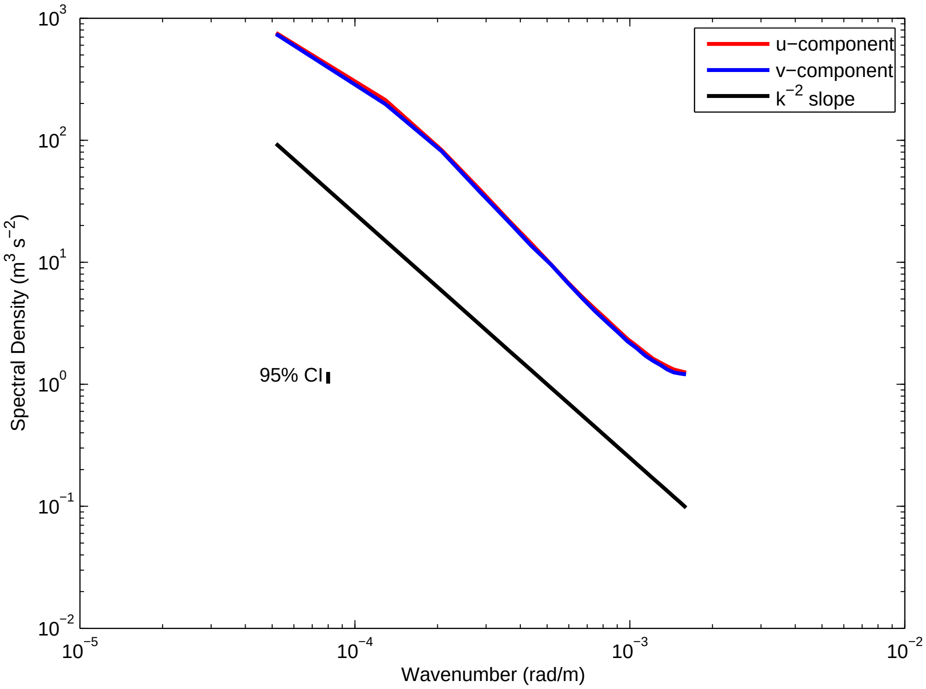

Figure E.2: Mean u- and v-component wavenumber spectra for MCC SAR currents, averaged over a number of different times and scenes as described in the text.

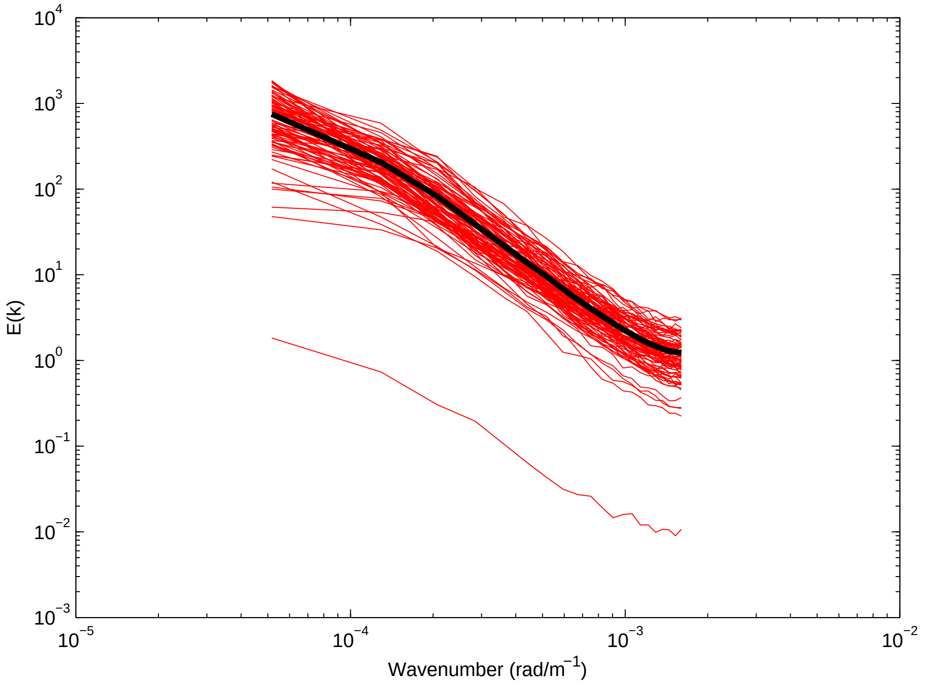

Figure E.3: KE wavenumber spectra from each MCC SAR current field (in red), and the overall mean (in thick black line). The mean spectrum is the same spectrum shown in Fig. 3.12.

Appendix F

Overall Distributions of 6 km Re-gridded Coincident MCC SAR and HF Radar Currents

The data distributions of MCC SAR and HF radar currents are compared in Sec. 3.5.1 for magnitude, direction, and vector components for 2 km re-gridded coincident datasets. The results from 6 km re-gridded coincident datasets are very similar, and plots for them are shown here. Fig. F.1 corresponds to Fig. 3.16, while Fig. F.2 corresponds to Fig. 3.17. The discussion in Sec. 3.5.1 applies for the plots here also.

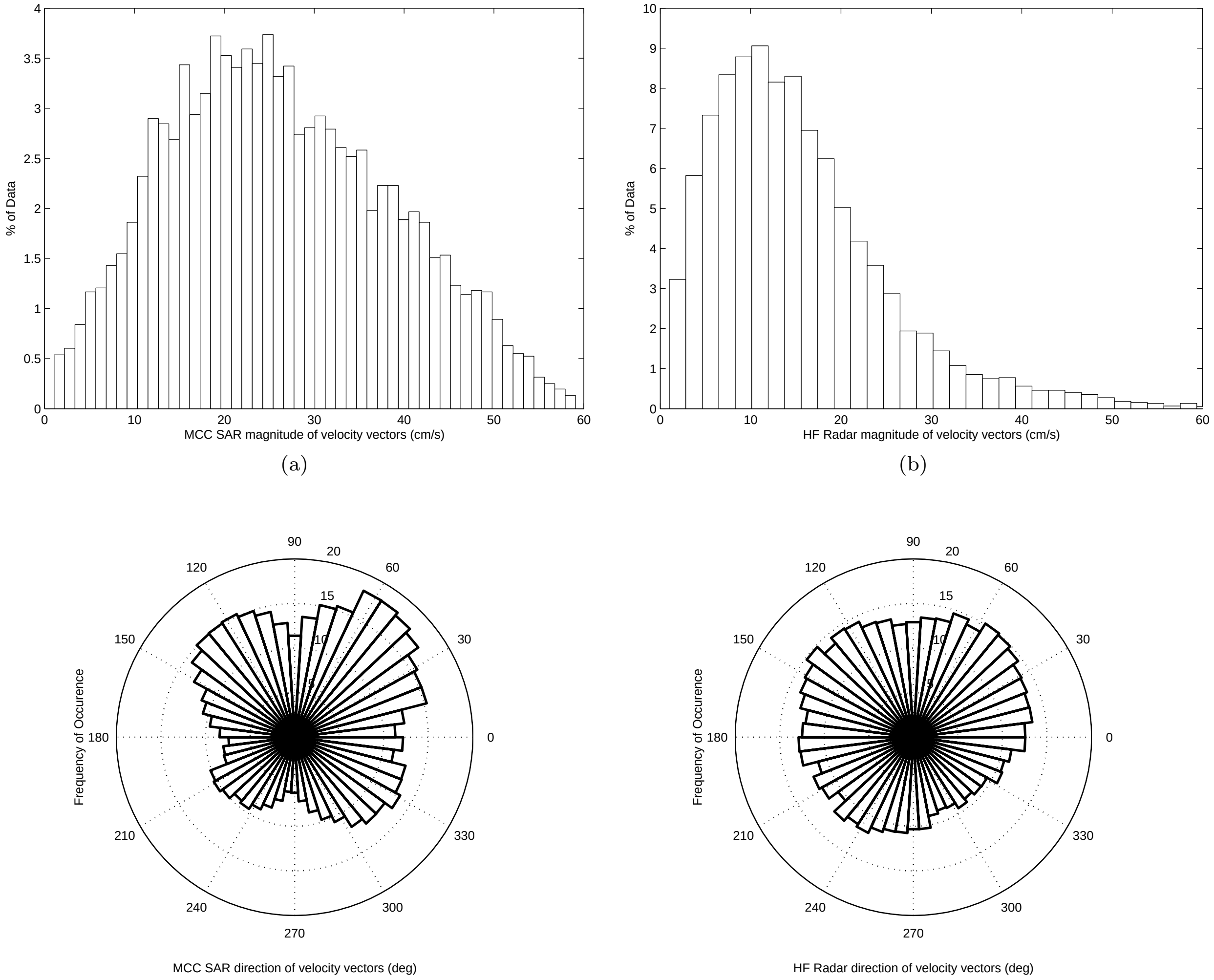

(a) (b)

(c) (d)

Figure F.1: Histograms of data distributions for magnitude and direction ((anti-clockwise from East) of re-gridded coincident MCC SAR and HF radar currents. (a) and (b) are histograms for velocity magnitudes of MCC SAR and HF radar currents, respectively. (c) and (d) are histograms for velocity directions of MCC SAR and HF radar currents, respectively.

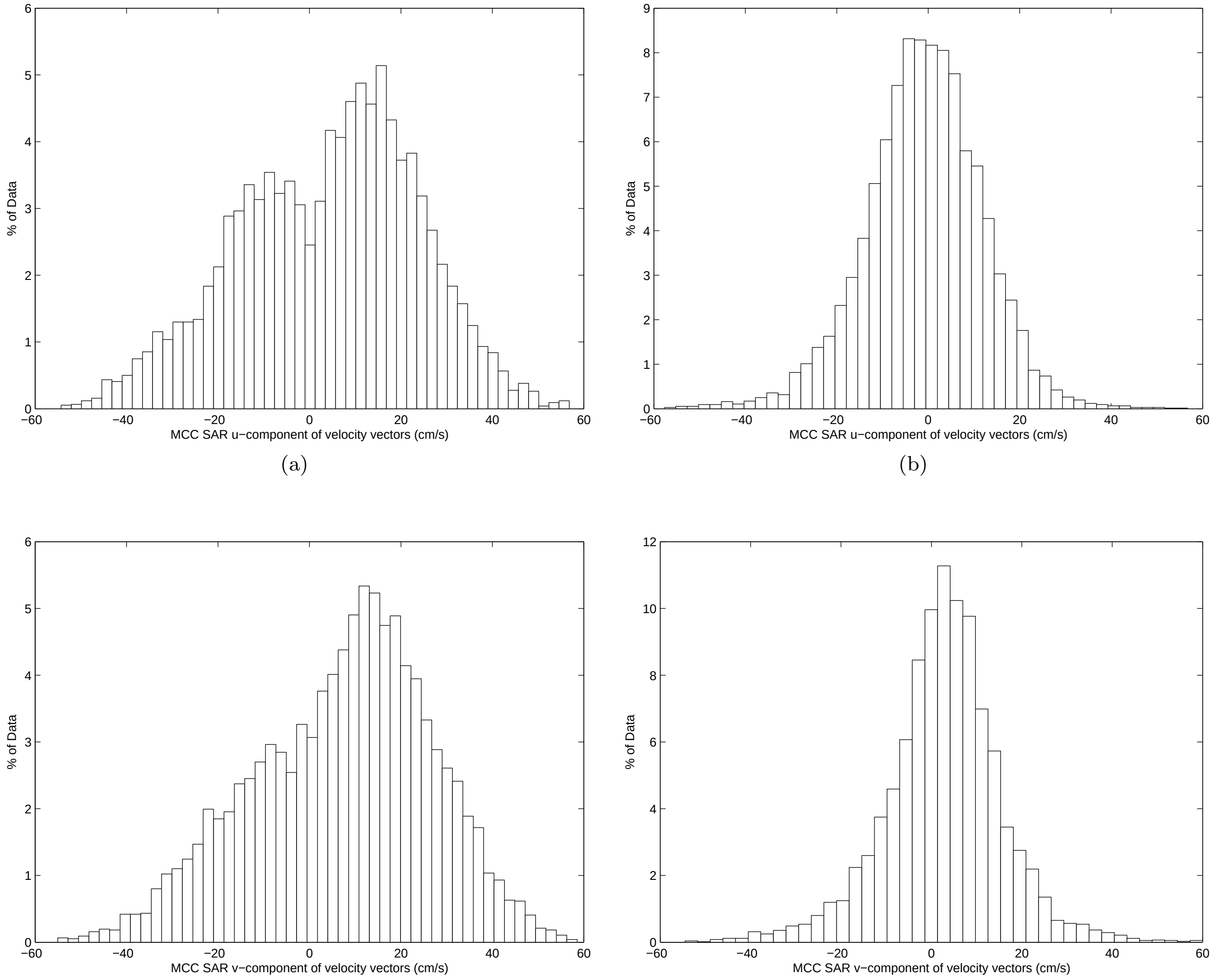

(a) (b) (c) (d)

Figure F.2: Histograms of data distributions for vector components of re-gridded coincident MCC SAR and HF radar currents. (a) and (b) are histograms for the u-component of MCC SAR and HF radar currents, respectively. (c) and (d) are histograms for the v-component of MCC SAR and HF radar currents, respectively.